Fracture mechanics in the semigrand canonical ensemble

by

Talal Mulla Mahmoud

S.B., Massachusetts Institute of Technology (2013)
S.M., Massachusetts Institute of Technology (2017)

Submitted to the Department of Civil and Environmental Engineering
in partial fulfillment of the requirements for the degree of

Doctor of Science in Civil Engineering

at the

MASSACHUSETTS INSTITUTE OF TECHNOLOGY

June 2021

Author . . . .
Department of Civil and Environmental Engineering
April 27, 2021

Certified by . . . .
Franz-Josef Ulm
Professor
Faculty Director, Concrete Sustainability Hub
Thesis Supervisor

Accepted by . . . .
Colette L. Heald
Professor of Civil and Environmental Engineering
Chair, Graduate Program Committee

Fracture mechanics in the semigrand canonical ensemble

by

Talal Mulla Mahmoud

Submitted to the Department of Civil and Environmental Engineering
on April 27, 2021, in partial fulfillment of the
requirements for the degree of
Doctor of Science in Civil Engineering

Abstract

We present a novel simulation method to assess the quasi-static fracture resistance of materials. Set within a semigrand canonical Monte Carlo (SGCMC) simulation environment, an auxiliary field –the bond rupture potential– is introduced to generate a sufficiently large number of possible microstates in the semigrand canonical ensemble, and associated energy and bond fluctuations. The SGCMC approach permits identifying the full phase diagram of brittle fracture for harmonic and non-harmonic bond potentials, analogous to the gas-liquid phase diagram, with the equivalent of a liquidus line ending in a critical point. The phase diagram delineates a solid phase, a fractured phase and a gas phase, and provides clear evidence of a first-order phase transition intrinsic to fracture. Moreover, energy and bond fluctuations generated with the SGCMC approach permit determination of the maximum energy dissipation associated with bond rupture, and hence of the fracture resistance of a widespread range of materials that can be described by bond potentials.

We further adapt the method to a hybrid analytical-simulation investigation of the fracture resistance of heterogeneous materials. We show that bond-energy fluctuations sampled by Monte Carlo simulations in the semigrand canonical ensemble provide a means to rationalize the complexity of heterogeneous fracture processes, encompassing probability and percolation theories of fracture within a unified framework of fluctuation-based fracture mechanics. For a number of random and textured model materials, we derive upper and lower bounds of fracture resistance, which are critical to identify toughening mechanisms. Specifically, elastic toughening mechanisms due to elastic energy mismatch are shown to result from both the activation of cooperative interactions in soft-tough bulk phases and interfaces, and the transition from critical to subcritical bond fracture percolation in textured materials. While counter-intuitive on first sight, this soft-tough paradigm can explain a number of experimental observations, including toughening of brittle solids by deformable polymers or organics, such as gas shale, nacre, stress-induced transformational toughening mechanisms in ceramics, and toughening of sparse elastic networks in hydrogels, to name a few.

Thesis Supervisor: Franz-Josef Ulm
Title: Professor
Faculty Director, Concrete Sustainability Hub

–G

Acknowledgments

Almost every portion of this thesis can be traced back to a specific person with whom I have had multiple conversations or some sort of exchange. My doctoral degree committee, very much like this thesis, is split in two, between physics and mechanics. Beginning with the thesis advisor, Prof. Franz-Josef Ulm, and the committee chair, Prof. Roland Pellenq, the committee is completed with Prof. David M. Parks, Prof. Mehran Kardar, and Prof. Colette Heald. This thesis aims to frame fracture mechanics within a statistical mechanics problem. Drawing on two seemingly disparate fields, the committee members during my doctoral degree pursuit became, as such, an invaluable wealth of understanding and perspective.

Help did not come exclusively from my committee, as I had the added great fortune of working closely with other professors and post-docs who are each, in their own rights, experts in their fields. At the top of this list are Katerina Ioannidou and Sina Moeini who helped completely reshape the middle of this thesis, so much so, the middle became the beginning and the original beginning became an appendix. I have to also thank Prof. Daniele Veneziano because I learned probability from him all those years ago; it stuck with me because, after all, everything (absolutely everything) is a probability until it is past. Whether or not I did probability justice in the pages to come is not for me to say, but statistical mechanics always felt, to me, like it would be better understood if it were called probabilistic mechanics, who knows which came first.

I am grateful to have a supporting family that I can rely on at every step of any journey. I close out the acknowledgements with a bang, thanking my mother and brother. I literally cannot do anything without my mother and brother; no amount of recognition or thanks can suffice in this regard.

Contents

List of Figures

List of Tables

Chapter 1

Introduction

Across history, the human species is defined by the materials they use or tool with their minds and hands at least from the stone age, bronze age, iron age, to the industrial age, machine age, and the present day defined contemporaneously as the atomic age, space age, and information, or more recently big data, age. With these developments in the tools and materials used, there is also a revolution through materials by design paradigm propelled by advances in computational power. Composites that overcome materials trade-offs vis-á-vis strength versus toughness, for example, bioinspired designs learning from nature's best, and additive manufacturing for rapid prototype fabrication create a deluge of new materials that are in contention with the idea of a homogenized continuum element, mandating reexamining many mechanics ideas, especially when it comes to the relatively nascent field of fracture mechanics. Materials no longer define the age in which we live in when we are defining new materials.

In this same spirit of reversal of circumstances, this thesis proposes flipping the discourse in fracture mechanics. Instead of thinking of the forward problem of a crack propagating due to energy balance between strain energy and fracture energy, consider the inverse problem where the total energy is defined and allowed to evolve as would stress and strain fields, for example, and whether or not a crack exists or propagates is not prescribed *a priori.* In essence, we remove the idea of a crack from fracture mechanics. While this may seem counter intuitive, it does invite the question what will the replace the crack in this inverse problem. Ultimately, at failure a crack must be included. From the outset these are contradictory statements. First, fracture analysis is done without a crack. Then, at fracture there is a crack. In fact, this is an apt macroscopic analogy for all the simulations in this thesis as will be described in full detail in Ch. 2. For now, we will go through a quick review of fracture mechanics over the past century.

1.1 Highlights from a hundred years of fracture mechanics

Fracture mechanics, in the modern formalism, was born in 1921, predating this thesis by a century, out of Griffith's work on molten glass as the prototypical material ideal for his theory of "rupture and flow in solids" [1]. It was not until World War II that interest in fracture mechanics piqued to avoid such losses as the now infamous Liberty ships [2]. This becomes a common motivation for all fracture mechanics research, either to avoid failure through fracture, or tailor the fracture as desired (think opening a soda can). Griffith's mental movie of fracture was composed of a sequence of frames, each at thermodynamic equilibrium, constantly negotiating the energy balance necessitated by fracture surface creation. Griffith's idea of competing energies, between the energy stored in a glass under loading and the energy released during fracture surface creation, required quantifying the surface energy of the glass. The energy stored in the glass is readily available from elasticity solutions so there was no obstacle there. This is where the molten glass comes into play. Through raised temperature creep tests on the glass, elementary force balance, and some trigonometry, Griffith is able to obtain the required measurement of the surface energy of the glass used in his experiments.

Since then, fracture mechanics has been expanded upon by numerous researchers and scientists, to now include measurable quantities dedicated to fracture, such as the energy release rate, stress intensity factor, J-integral, crack-tip opening displacement, and others [3]. All these ideas share the same origin from either conservation of energy or equilibrium of stresses because whenever fracture occurs there is a disturbance in both of these quantities, so they aptly serve as proxies to study and measure fracture. In listing all these quantities and their relation to fracture mechanics, a common theme arises, and that is the presence of a crack in the material of interest. Here, a distinction arises between crack initiation and crack propagation. Another theme, especially in the early developments of all these methods, is the limited applicability to homogeneous materials.

Griffith's work laid the foundation for the continuum approach to fracture mechanics expanded by Irwin [4, 5] and Orowan [6] based on an energy release rate. Stress intensity factors were included in the discourse on fracture by examining the stress fields around the crack tip. So far, these considerations rely on solutions that include a mathematically sharp crack [7, 8]. Cherepanov and Rice independently developed a path-independent integral now known as the J-integral [9, 10] expressing the energy balance between applied load and stored strain energy. This path integral is zero when enclosing a domain with no discontinuities, such as cracks (or if both ends of the crack are contained in the path integral); when only one end of the crack is enclosed in the domain of the path integral the value is a measure of fracture toughness (and clearly the problem becomes more complicated when considering more cracks).

Such are the early development of continuum fracture mechanics, which when observing small scale yielding avoids contrasts with the atomic discreteness of all materials. This naturally leads to a limitation and a size effect stipulation on the efficacy of continuum fracture fracture mechanics especially towards smaller length scales [11]. Discrete fracture mechanics, explicitly takes into account these limitations. Owing to this fact much research has been dedicated to probing discrete fracture mechanics especially with computational tools through finite element analysis [12–15], molecular dynamics [16, 17], and lattice based methods [18–20]. Understanding the discreteness of fracture better defines the aptness of continuum theories and further pushes beyond the attached limitations.

Discreteness implicitly encodes failure, or fracture, probabilities for area (2D) or volume (3D) elements. Especially for crack propagation, fracture can be viewed as a rare phenomenon in a material in terms of damage, stress, or strain localization [21–23]. Statistical models of fracture have been developed following rigorous formulation of extreme value theory [24–26], discounting effects of embedded stochasticity on the path for a deterministic model. This engenders a statistical mechanics view of fracture, viewing each discrete point or element as a collection of random variables that on the outset may or not be independent.

Statistical mechanical models of fracture also take a discrete view of fracture, in addition to employing the extensive framework of statistical mechanics to garner new insights into material failure [27]. Modeling of phase transitions and convergent behavior is usually undertaken in statistical physics and has also been applied to fracture [28, 29]. From the statistical mechanics points of view, fracture presents a number of interesting features including universality and scale-invariance of the crack morphology or roughness [30–34], power-law percolation behavior due to disorder in heterogeneous materials [35–38], and dynamical order parameters associated with crack front propagation [39–42].

Among the earliest models of heterogeneous fracture is the fiber-bundle model, which has been extended and adapted into many iterations far beyond its initial purpose of describing the strength of cotton yarns [43–45]. Extensions of the fiber bundle model aim to describe damage behavior of materials between the extreme cases of load sharing in the model, namely global load sharing and local load sharing. Moving from textiles to electricity, the random fuse model was expressly developed to study fracture of disordered material relying on the similarities between a strained mechanical sample and an electrical network of fuses with a voltage difference applied across it. Random fuse network models construct analogies with electrical circuits and dielectric breakdown to examine mechanical fracture where percolation occurs with respect to conductivity of the network, and a shift of the percolation threshold is observed when disorder is introduced by prescribing random fields [25, 27, 46]. In both cases of the fiber bundle and random fuse models, intrinsic to the model is a prescribed probabilistic description of failure thresholds in the fibers and fuses, respectively.

The challenge of effective fracture properties of heterogeneous materials is (at least) two-fold. While fracture properties of each constituent of a heterogeneous material can be known, the effect of the interaction through texture effects, micro-cracking [47], crack shielding [48], different phases and interfaces [49–53], and other fracture toughening (or worsening) mechanisms [54–57] is not always known, making it difficult to determine the appropriate averaging scheme. This is particularly problematic in terms of discrete fracture mechanics, which by definition considers each element individually, and approaches the solution through a bottom-up approach. Modelling heterogeneous materials for use in the discrete approach is challenging in itself, and different assumptions can lead to varying results [58–60].

Just as Griffith employed a specialized experimental setup to obtain the surface energy of a glass, we too shall employ an appropriate simulation setup within a statistical mechanics framework to obtain relevant quantities of interest useful in the study of fracture mechanics. The next chapter goes into full detail regarding the statistical mechanics basis of this thesis and its application fracture mechanics through simulation.

1.2 Research objectives

The overarching aim of this thesis is to resolve the absence of a general framework for assessing fracture of heterogeneous materials. Throughout this introduction we have alluded to how and what will be done to address this open-ended problem of fracture of heterogeneous materials. In this section, we will make the points clear, and in the next section we will outline the contents of the forthcoming chapters.

The first and most immediate objective is to devise a simulation approach that can do fracture mechanics without a crack. This is done by revisiting the apparent contradiction stated in the beginning of this chapter where the system starts with no crack and then ends with a crack at failure. This in fact, is not a contradiction at all, but merely a logical timeline of fracture. The allusion, however, that is made is to Monte Carlo forward and reverse trial moves. Thus, the simulations that will be performed are Monte Carlo simulations. The trial moves that we seek are exactly the absence and presecence of a crack, but in a more discretized manner. The smallest portion of a crack, then, is a bond, and the Monte Carlo simulations will be taking out and putting back in bonds over the course of a simulation. This concludes our first objective: setting up Monte Carlo simulations that work on the bonds of a system.

With the fruits of the first objective, we need to apply our simulation protocol to both homogeneous and heterogeneous simulation material models. The homogeneous systems are necessary to act as baselines for the heterogeneous application of the newly created Monte Carlo simulation method.

Finally, the third and possibly most important objective is to answer the question: can a general framework for fracture of heterogeneous materials be created, and if not, why not, and what are the obstacles hitherto?

1.3 Thesis outline

Chpater 1, provides relevant background information to motivate the research objectives and outlines the rest of the thesis.

Starting with first research objective, Chapter 2 elucidates the mechanisms of a semigrand canonical Monte Carlo (SGCMC) simulation. To do this, some statistical mechanics background is presented, with an emphasis on the semigrand canonical ensemble. The chapter ends with simulations details including geometry, energy potential, and loading condition specifications for the simulations models.

Chapter 3 moves on to the first half of the second research objective, which is to perform a parametric study on homogeneous materials with SGCMC simulations. The outcome of this parametric study is a phase diagram of brittle fracture, defining deformed solid, fractured solid, and gas-like phases. Fracture is defined through a semigrand canonical formulation of the linear elastic fracture mechanics criterion, $G = G_c$, where the SGC criterion is expressed in terms of heats of bond rupture.

Fracture of heterogeneous materials is readily handled in Chapter 4, with direct extensions of the work of chapter 3, completing the second half of the second research objective. Two-phase composites in two dimensions are used as the model heterogeneous materials with different volume fractions and textures. Probability arguments are used to develop analytic upper and lower bounds on fracture resistance of heterogeneous materials. Simulations fill in the domain between these bounds, identifying percolation associated with fracture of heterogeneous materials.

Ch. 4 will deal primarily with two-phase, two-dimensional composites. Ch. 5 will extend the discussion to three dimensional, two-phase composites, and expand the analysis to include measurement of two-point correlation functions, to and tie this established measure with the work of this thesis.

Finally, Ch. 6 will return the discussion to two dimensions exploring the effect of loading orientation and interfaces on the fracture resistance of composite materials. The interface study, in particular, will demonstrate the extension of the method to n-phase composites by treating each additional interface as a separate phase.

With the work of Chapters 3-6, the final research objective can be addressed in the concluding Chapter 7. Results and key insights are summarized. After hundreds of thousands of SGCMC simulations, Chapter 7 presents a unique perspective across two and three dimensions regarding the extreme value statistics embedded in fracture of homogeneous and heterogeneous materials.

Chapter 2

Methods

Possibly the most apparent or prolific indicator of fracture in a material is a crack. In so much fracture mechanics theory this crack is mathematically idealized as an infinitely thin slit, or an infinite line in the half-plane. Placing a marker for the location of the crack, and the crack tip, is necessary to develop the functional forms of the fracture mechanics crack-tip stress and strain field solutions that exist in many handbooks [61]. This differentiates the study of the propagation of a pre-existing crack, as opposed to crack initiation. As such, many assumptions can become implicit in fracture mechanics. One such assumption, is that all materials are full of defects even before the onset of crack propagation, in the form of microcracks, for example. In this thesis, we propose to forego the crack completely and instead focus on the precursors of a crack, which include the precursors to the microcracks, as well, namely the bonds in a material.

Precursory to any defects is a pristine material without any cracks or microcracks. What is not absent in the picture, but often overlooked, are the bonds that hold the material together. If the bonds break, microcracks form, and if enough bonds break in the vicinity of the same plane (in three dimensional space, or line in two dimensions), a crack initiates and propagates, amidst a large number of randomly formed microcracks (or the many tiny defects that exist in the material before fracture). During this process of bond breaking the stress and strain fields, simultaneously evolve such that the bonds do ultimately break along a crack plane. Cracks, thus, become an end (or intermediate) point and not a starting point for fracture. While observing the bonds in the fracture process might be practically challenging, such observations are far more tractable in simulation.

This chapter lays the approach undertaken in this thesis to study fracture mechanics from the perspective of bonds. There is no *a priori* crack in the material, and the material must be described through bond-wise potentials, as opposed to pair-wise potentials, that are a function of the distance of specific pairs of mass points in the material. These pairs of mass points form the endpoints of every bond in the material and as such constitute a bond topology list, or bond list for short. Simulations to study fracture in this thesis, thus, make use of the Metropolis Monte Carlo algorithm set in a semigrand canonical ensemble. In the next sections, the semigrand canonical ensemble, Monte Carlo simulations, and the simulation details, for 2D and 3D geometries, that comprise the methodology of this thesis will be be discussed in further detail.

2.1 Statistical mechanics background

Fracture mechanics in the semigrand canonical ensemble enlists the impressive arsenal that is the framework of statistical mechanics. To understand how this is done, we will enter into a little primer on statistical mechanics, by no means aiming to be a comprehensive or exhaustive review of the topic. We only aim to set the reader up to understand what is to come in the rest of the thesis, and for more the reader is directed to see references [62–64] or any of a myriad of textbooks and online resources.

Let us start from the end and work backwards in our quick introduction to statistical mechanics. Without stating the aim of statistical mechanics or going too much into in-depth derivations, we will constrain ourselves to the aim of statistical mechanics as employed in this thesis to study fracture mechanics. More specifically, using the tools of statistical mechanics we will build a model of fracture for brittle materials that are sufficiently described as mass points connected by bonds. Our model will be able to quantitatively describe the fracture resistance of any such bonded material model, whether the material is homogeneous or heterogeneous, with a special interest in advancing fracture mechanics of heterogeneous materials. The first step is to set the statistical mechanics stage where we will study fracture mechanics.

Setting the stage in statistical mechanics means choosing the appropriate (thermodynamic) ensemble with which to develop the expressions necessary to construct the probabilities of microstates of a system. Immediately, the ensemble implies the existence of microstates, so named because they comprise the macrostate, or system being modeled. Also implied, is that each microstate is associated with a certain probability. Semantically, an ensemble is the label given to a group of items. In statistical mechanics, these items are defined as all possible microstates of a system, or macrostate. The reason the idea of an ensemble is so important in statistical mechanics lies in the fundamental premise that *a priori* the probability of (occurrence of) any given microstate of a system in the same ensemble is equal. Two points require special attention. First, the assumption of equal probability is made at the outset, given no information about the microstates or ensemble. Second, the equiprobability is predicated on the condition all the microstates belong to the same ensemble. Statistical mechanics works by modeling physical phenomena as a set of probabilities, or random variables. The goal, then, is to describe these probabilities, and the best way to do this is through the probability density function for continuum random variables, or probability mass function for discrete random variables.

We need to construct probabilities pertinent to this fracture of bonded materials using an appropriate statistical mechanics model. The probability we seek is the probability of a crack forming or a bonded material breaking. We have to start by choosing an ensemble to begin writing the unambiguous mathematical constructs to describe this probability. We will be using numerical solvers, so let us agree to use a discrete formulation. In choosing an ensemble, we have to look ahead as to what might be the random variable for which we seek a probability mass function. In fracture, and in the bond-view point we have taken, the number of bonds in our system is chosen as the random variable to model. That is, the choice of ensemble must permit an avenue to construct the probability of a given microstate of a system having a set number of bonds or more explictily stated in terms of a symbolic equation:

$$P[N = n] = \frac{\#\text{of microstates with } N = n}{\#\text{of all possible microstates in this ensemble}} \tag{2.1}$$

where N is the random variable for the number of bonds, and n is any nonnegative integer. Stating the probability in Eq. 2.1 serves as a reminder of what statistical mechanics does when it models different phenomena as probabilities. Once an ensemble is chosen, the numerator becomes standardized, but the denominator constitutes one of many hurdles in statistical mechanics. Counting all the possible microstates in an ensemble quickly becomes an intractable task, so much so, this denominator is given its own special name, and this number is upgraded to a function, known as the partition function. For any ensemble in any problem, there will always be a need to define the partition function, as it is a tenet of any probability being the probability mass of sample space; without it, no probability can be defined.

Not only does the ensemble set the stage and mechanics of the formulation of the problem, it also defines the important partition function. A list of ensembles and their meanings is given in Table 2.1. All the ensembles are given a shorthand three- or four-letter name, referring to the thermodynamic state variables that serve as landmarks for all the microstates that belong to it. Being landmarks of the ensemble, these state variables are held constant. For example, the canonical ensemble is termed the NVT ensemble, as N, particle number, V, system volume, and T, temperature are held constant, meaning these are set quantities that fluctuate very little or not at all around a prescribed value and are the same in all microstates of a system in the canonical ensemble. As such, the first thing the choice of ensemble does is to fix at least a triplet of extensive (size-dependent, as in volume, number of atoms or bonds, and energy) and intensive (size-independent, as in pressure, P, chemical potential, μ, and temperature) variables. There are further implications to setting a state variable constant, because all these intensive and extensive variables come in intensive-extensive work-conjugate pairs; meaning the product or the integration of one variable with respect to its work-conjugate results in a measure of energy

Table 2.1: List of some thermodynamic ensembles. The thermodynamic ensembles build on each other starting from the microcanonical ensemble, especially in terms of construction of the partition functions (think how the probability of the sum of dice changes based on the number of dice rolled). Addition of a thermostat yields the canonical ensemble. Further allowing particle insertion and removal expands the canonical ensemble into a grand canonical ensemble. Setting a finite particle reservoir in the grand canonical ensemble makes it a semi-grand canonical ensemble. These changes are highlighted in red in the table.

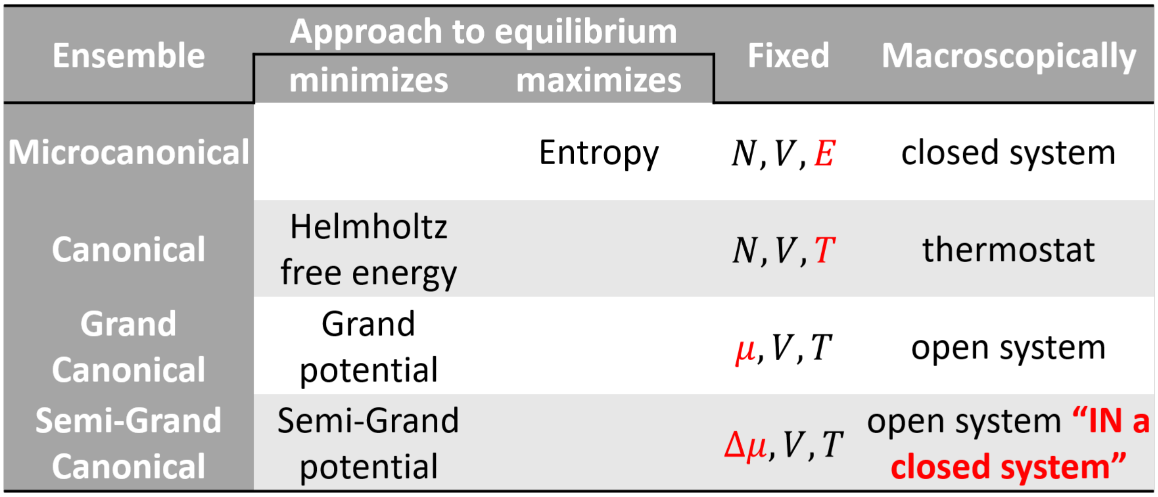

Ensemble	Approach to equilibrium		Fixed	Macroscopically
	minimizes	maximizes		
Microcanonical		Entropy	N, V, E	closed system
Canonical	Helmholtz free energy		N, V, T	thermostat
Grand Canonical	Grand potential		μ, V, T	open system
Semi-Grand Canonical	Semi-Grand potential		$\Delta\mu, V, T$	open system **“IN a closed system”**

(units of work). In other words, choosing an ensemble means setting certian variables constant while at the same time allowing their work-conjugates to fluctuate. These fluctuating quantities become the unknowns in the model and must be resolved either analytically, or more likely, through simulation.

With this understanding we are closer to choosing the best (or at least better) ensemble for our model of fracture, which requires an unknown random variable, the bond number. As the bond number is the unknown, or fluctuating quantity, we require an ensemble that sets the work conjugate of the bond number constant. We can view the bonds as particles, then, the fluctuating quantity is N, and its work conjugate is the chemical potential, μ. A point of notation arises here where we will label the chemical potential as a bond rupture potential for two reasons. First, fracture is viewed as bond rupture in order to create fracture surfaces and cracks. Second, bonds are not customarily taken as the particles in statistical mechanics literature or even in many simulation software packages, which more often take an atom- or mass point-centric view, and the change in notation reinforces these points. Out of all the ensembles in Table 2.1, the ensembles that will satisfy the requirements of our fracture model are the grand and semigrand canonical ensembles. While both these ensembles permit a changing number of bonds, only the semigrand canonical sets a fixed reserve of bonds. In the case of fracture of a brittle solid, we do not require an infinite reserve of bonds; the total number of bonds in the pristine material is a constant. As such, the semigrand canonical ensemble is more appropriate for the study of fracture. Choice of ensemble is a mathematical tool when considering the thermodynamic limit, and for a grand canonical formulation of fracture the reader is referred to Appendix C.

2.2 Semigrand canonical ensemble

With the choice of semigrand canonical ensemble made, the next step is to set the fixed reserve (number) of bonds to the total number of bonds possible in the system, N_0. Now when the bonds, N, break we can consider them as broken bonds, $N_b = M = N - N_0$, and it is clear that

$$N_0 = N + N_b \tag{2.2}$$

further justifying the choice of ensemble. More importantly, the choice of ensemble allows us to refine our microstate probability from Eq. (2.1) by providing a functional form for the semigrand canonical partition function at fixed volume and temperature [65–68]:

$$\Upsilon = \sum_{(1):i=1}^{c} \cdots \sum_{(\mathcal{N}):i=1}^{c} \frac{1}{\mathcal{N}!} \left[\prod_{j=1}^{c} q_j^{\mathcal{N}_j} e^{\beta \mathcal{N}_j (\mu_j - \mu_1)} \right] \int_{(1)} \cdots \int_{(\mathcal{N})} e^{-\beta U} d\mathbf{r}^{\mathcal{N}} \tag{2.3}$$

where $\mathcal{N}$ is the total number of particles (or bonds) considered of all species (e.g. broken, intact), $\beta = \frac{1}{k_B T}$, k_B is the Boltzmann constant, μ_1 is an arbitrarily set reference chemical potential, U is the potential energy, $\mathbf{r}$ is the coordinates vector of the bonds, and the coordinate of a bond is defined as the midpoint of its endpoints, and q is a variable containing kinetic terms from the integration over momenta. The $\mathcal{N}$ summations and integrals refer to the discreteness of the bonds and continuous applied strain, respectively. The summations, for each bond, sum over all the different identities a bond can have (2 in our case, either broken/OFF or intact/ON). In this way and as presented in [65] and [67], the partition function counts all possible arrangements of a total of N bonds where each bond can be either broken or intact. With tens of thousands of bonds and an infinite (or as close to infinite as digital precision allows) spectrum of strain, this partition function becomes unwieldy.

With an intractable probability distribution function owing to the partition function, the next best thing would be to sample from this unknown probability distribution. As this problem of a partition function is so ubiquitous, statistical physics offers several solutions with varying degrees of accuracy; there is always a trade-off or compromise in this sense. In our case we choose to go the molecular simulation route using Monte Carlo simulations.

2.3 Metropolis Monte Carlo method in the semi-grand canonical ensemble

Monte Carlo simulations performed in this thesis follow the Metroplos algorithm dating back to 1953 [68,69]. We have shown statistical mechanics enables us to construct microstate probabilities from Eq. (2.1), but we can not evaluate this probability because we do not know the value of the denominator, the partition function. We can overcome this inconvenience by noting that every probability of every microstate in any ensemble has the same denominator; sample space is the same for all microstates because they are in the same ensemble. Furthermore, we know that any number other than zero divided by itself is equal to 1. Metropolis' idea is to do just that, pick two microstates and assign a relative probability of moving from one to the other equal to the ratio of their respective probabilities. This ratio of probabilities no longer contains the partition function because it cancels out in the division.

Now we move from absolute probabilities to relative probabilities. To do so, we proceed by creating two microstates, 1 and 2, for which we will alter only one item, namely the random variable in question, the bond number, N. For example, bond x can be in the intact/ON state in microstate 1 and broken/OFF state in microstate 2, and all the other bond are identical in terms of whether they are ON or OFF. This, of course, has further ramifications for each microstate in terms of the system energy, stress and strain fields, but only through the effects of the change in bond number[1]. Next, since all we know is that these microstates belong to the same ensemble, to construct relative probabilities we require *a priori* that the conditional probabilities of moving from state 1 to state 2 and the reverse move, moving from state 2 to state 1, are equal. We impose this detailed balance condition in the construction of our relative probabilities in order to remove bias for any one microstate. When the probability of moving back and forth between two microstates is equal we are in equilibrium and that is the end goal of the simulation. Defining p_{12} as the probability of a move from microstate 1 to 2, and p_{21}, from 2 to 1, we can write out the condition for detailed balance as:

$$p_1 p_{12} = p_2 p_{21} \tag{2.4}$$

that is, the probability of going from state 1 to 2, p_{12}, conditioned on being in state 1, p_1, is equal to the probability of going from state 2 to state 1, p_{21}, conditioned on being in state 2, p_2. Rearranging Eq. (2.4) we arrive at the relative probabilities as [67, 68]:

$$\frac{p_{12}}{p_{21}} = \frac{p_2}{p_1} = \frac{\xi_2}{\xi_1} e^{-\beta(U_2 - U_1)} \tag{2.5}$$

where $\xi_i = e^{\beta\mu_i} / \sum_j e^{\beta\mu_j}$ are the fugacity fractions across all the species in the system (broken/OFF or intact/ON), where the fugacity absorbs all the terms carried over from the integration over momenta in the partition function [67], and the partition function cancels out in the division.

---

[1] These differences are more to do with the canonical moves, which are a different set of Monte Carlo trial moves that will be discussed later.

As these are relative probabilities, their utility is confined to the set of assumptions used in constructing them. Specifically, these relative probabilities can only indicate which of the two states 1 or 2 is more likely than the other. Moreover, there is no guarantee that these probabilities are less than or equal to 1 (no guarantee that these numbers are probabilities), because while they are ratios of conditional probabilities, they themselves are not conditional probabilities. This is where Monte Carlo trial moves are defined as well as their acceptance probabilities. Performing these moves constitutes running a Monte Carlo simulation[2].

At this point the Monte Carlo moves are straightforward, they are going from state 1 to state 2, and because of detailed balance, its reverse move, going from state 2 to state 1. The implementation of the Monte Carlo method in our case is through simulations where trial moves are attempted randomly based on the partition function used to develop the acceptance probabilities. These are trial moves because whether or not we will actually perform them depends on the acceptance probabilities. So far, we only have relative "probabilities" from Eq. (2.5), and we alluded to how these are just numbers that can (and do) become greater than 1.

Just as we moved from absolute probabilities to relative probabilities because of the unknown value of the partition function, we must make one more final move from these relative probabilities to acceptance probabilities. In this case, we know the numerical values of all the components of our relative probabilities through simulation, for example. However, these relative probabilites are not strictly speaking probabilities as they can be greater than 1. Let us consider the case when a relative probability becomes greater than 1.

$$\frac{p_{12}}{p_{21}} = \frac{p_2}{p_1} = \frac{\xi_2}{\xi_1} e^{-\beta(U_2 - U_1)} > 1 \tag{2.6}$$

There are two ways to understand this inequality. Straight from the definition of the relative probability as the ratio of the likelihood of the moves (state 1 → state

---

[2] All Monte Carlo simulations attempt to sample data from a probability distribution. In this way, there are two types of Monte Carlo simulations based on whether the probability distribution being sampled from is (1) known or (2) unknown.

2 to state 2 → state 1), a relative probability greater than 1 implies the move from state 1 to state 2 is more likely. Another interpretation is from the functional form of the relative probabilities, where the exponentials are always non-negative, so being greater than 1 further indicates this move is more likely because it means the energy change of the system ($\Delta U = U_2 - U_1 < 0$) is going in the direction of minimum energy. Otherwise stated, this move should always be accepted and in terms of the acceptance probabilities,

$$p_{acc}\left(1 \rightarrow 2\right) = 1 \qquad\qquad \frac{p_{12}}{p_{21}} \geq 1 \tag{2.7}$$

On the other hand, when the relative probability is less than 1 (i.e. behaving more like a probability), we are not so sure that the move from state 1 to state 2 is the more likely move in this ensemble. Further, we do not have the negative energy change ($\Delta U < 0$) as in the previous case. Here is where the "game of chance" (sampling work) of the Monte Carlo method comes into play [69]. The relative probability is less than 1, now, so we can treat it as a genuine probability. All that is left to do is randomly (fairly) draw from a uniform random distribution, and compare the random number, x_U we drew to the calculated relative probability, $\frac{p_{12}}{p_{21}} < 1$. If $\frac{p_{12}}{p_{21}} > x_U$ (i.e. closer to the upper cutoff of a probability), we accept the move, otherwise we reject it. We would have accepted the move if $\frac{p_{12}}{p_{21}} > 1$, but now we enlist an unbiased judge in the form of a uniform random distribution to assess how far $\frac{p_{12}}{p_{21}}$ is from our acceptance criterion. Completing our acceptance probabilities for $\frac{p_{12}}{p_{21}} < 1$:

$$p_{acc}\left(1 \rightarrow 2\right) = 1 \qquad\qquad 1 > \frac{p_{12}}{p_{21}} > x_U \tag{2.8}$$

$$p_{acc}\left(1 \rightarrow 2\right) = 0 \qquad\qquad \frac{p_{12}}{p_{21}} < x_U \leq 1 \tag{2.9}$$

In effect the acceptance probabilities can be thought of as the proximity of the relative probabilities to 1, which leads us to the more standard way of expressing p_{acc} as:

$$p_{acc}\left(1 \rightarrow 2\right) = \min\left(1, \frac{p_{12}}{p_{21}} = \frac{p_2}{p_1} = \frac{\xi_2}{\xi_1} e^{-\beta(U_2 - U_1)}\right) \tag{2.10}$$

In this form we can directly, compare p_{acc} with x_U, the value of a random number generated on the interval $[0, 1]$ drawn for every trial move. In this sense, comparing the constructed relative probability, p_{acc}, with the probability of drawing a random number, less than x_U, sets the bar for randomness, or if something is a fluke or deliberate. If $p_{acc} > x_U$, the trial move is accepted and performed in simulation, otherwise the trial move is rejected and the simulation attempts another trial move, and so on until equilibrium is reached so that there is no more likelihood of moving from one microstate to another.

A more subtle point arises here in terms of the formulation of the partition function and its implications on the algorithm for attempting Monte Carlo semigrand canonical trial moves [67]. When attempting a trial move, the aim is to change the bond number N by 1. This can be done one of two ways. One way to perform the trial move is to randomly choose a bond and switch its identity (toggling from ON to OFF or OFF to ON). The other way to perfrom the trial move is to first randomly choose which move the trial move will be, either ON to OFF or OFF to ON. Then, depending on this random first choice, randomly choose a bond of the appropriate identity for which to carry out the trial move. The choice of partition function in Eq. (2.3) that led to the derivation of the acceptance probabilities in Eq. (2.10) specifies how this trial move is performed. As the partition function in Eq. (2.3) sums over all the identities of all the bonds, the trial move must be to randomly choose a bond and then switch, or toggle, its identity.

We now return to the effect of the change in bond number on the system energy and stress and strain fields and how these relate to the allowed Monte Carlo trial moves in the semigrand canonical ensemble. In addition to the switching of bond identities, we must perform canonical Monte Carlo moves, which include translations and rotations, to resolve the changes in system energy and stress and strain fields caused by the change in bond number; in other words, we need to do force balance. In lieu of performing canonical Monte Carlo moves in order to reach equilibrium, we perform standard time integration molecular dynamics, periodically, as the semigrand canonical moves change the bond number composition. By assumption of the ergodic hypothesis there should be no difference in time-averaging versus ensemble-averaging as long as we remain in an equilibrium setting and run the molecular dynamics for a sufficient amount of time.

In the next section we proceed to outline the practical simulation details for the various systems considered in this thesis including homogeneous, heterogeneous, two-dimensional, and three-dimensional models.

2.4 Simulation setup

Monte Carlo simulations are carried out in the semigrand canonical (SGC) ensemble as has been so far developed. The semigrand canonical ensemble is characterized by four prescribed state variables: total number of bonds, N_0, bond rupture potential, $\Delta\mu$, volume, V, and temperature, T. In contrast to the grand canonical (μVT) ensemble, the SGC ensemble is termed a $\Delta\mu VT$ ensemble, because the total number of bonds, N_0, is constant, admitting only a change in identity of the bonds, being switched 'ON'– or 'OFF'. Therefore, N_0 is the sum of these 'ON'– and 'OFF'– bonds, $N_0 = N_{ON} + N_{OFF}$ [see Eq. (2.2)], with N_{ON} the work-conjugate of the prescribed bond potential $\Delta\mu$. Analogous to insertion/deletion moves in GCMC-simulations, the 'ON'– and 'OFF'– setting of bonds is at the core of SGCMC trial moves, together with the bond topology of the considered texture model. The bond topology is dictated by the nearest neighbors of a mass point in the reference lattice. Randomly chosen 'ON'– and 'OFF'– Monte Carlo moves are completed with alternating Molecular Dynamics (MD) runs in the NVT-ensemble, to reach relaxed equilibrium states.

Two types of bond potentials are considered: a truncated harmonic potential and a Morse potential (see Fig. 2-1), both defined by a groundstate energy parameter, ϵ_i^0, and a stiffness parameter, k_i, in addition to the reference bond length, r_0, and cutoff distance for the harmonic potential, $r_c = r_0(1 + \sqrt{2\epsilon_i^0/k_i})$, so that, for the harmonic case:

$$U_i^H = \begin{cases} -\epsilon_i^0 + \frac{1}{2}k_i\left(r_i - r_0\right)^2 & r_i \leq r_c \\ 0 & r_i > r_c \end{cases} \tag{2.11}$$

where r_i is the bond legngth of the i-th bond, and for the non-harmonic, Morse potential:

$$U_i^M = D_i \left(1 - \exp^{-\alpha(r_i - r_0)}\right)^2 - D_i \tag{2.12}$$

where the Morse parameters, $D_i = \epsilon_i^0$ and $\alpha_i = \sqrt{k_i/2D_i}$, are obtained from a Taylor expansion of the Morse potential around r_0, in order to match the harmonic case. The approach can be extended to heterogeneous solids by considering a distribution of ground state energies and stiffness values either through random placement or texture, as will be seen in more detail in Chs. 4 and 5. Furthermore, reduced units are employed for the groundstate energy considering a low enough temperature (and associated thermal energy, k_BT) for the lattice to be a solid; that is, in our simulations, $T^* = k_BT/\epsilon^0 = 0.1$, where we have dropped the subscript i because in the homogeneous[3] case all $\epsilon_i^0 = \epsilon^0$ (see Appendix B). Similarly, due to the choice of the reference bond length, $r_0 = 1$, in reduced units, the stiffness parameter, k_i, is expressed in reduced units, $k_i^* = k_i r_0^2/\epsilon_i^0$. The chosen value $k_i^* = 61.32$ is representative of concrete when translating material properties into energy potential parameters in the lattice element method [70].

The SGCMC approach requires specifying the state variables of the SGC ensemble: bond rupture potential $\Delta\mu$, volume V, and temperature T, in addition to the constraint of a constant total bond number, N_0, fixed by the choice of the system. The prescribed volume is parameterized in the form $V = V_0(1 + \varepsilon_V)$, with V_0 the undeformed reference volume of the simulation box, and ϵ_V the volume strain. In the quasi-static strain-controlled test, the volume is increased by equally stretching the simulation box side lengths $L_x = L_y = L_z = L_0(1 + \lambda)$. Strain increments of $\lambda \approx \varepsilon_V/3 = 0.1\%$ are prescribed followed by long enough MD-simulations to reach quasi-static conditions in the displacement controlled test. Uniaxial displacement-controlled tension tests are carried out in the same way applying strain in only one direction.

In these simulations, the reduced temperature is controlled by means of a Nosé-

---

[3] In the heterogeneous case, we normalize all the energies by the groundstate of baseline phase (phase A), ϵ_A^0, such that the reduced temperature for all bonds is $T^* = k_BT/\epsilon_A^0 = 0.1$.

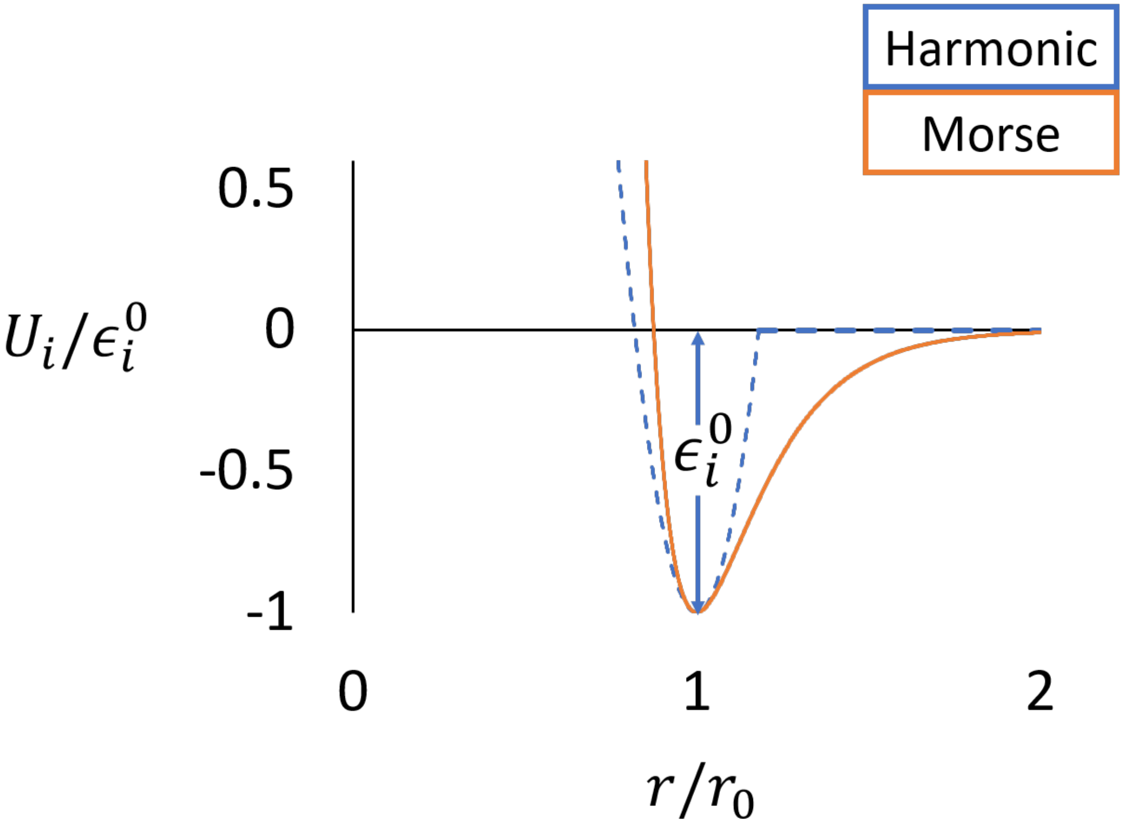

Figure 2-1: Truncated harmonic and Morse bond pontentials. Truncated harmonic and Morse bonds potential are used as model linear and nonlinear potential energy functionals for simulation. The harmonic potential does not taper off, so a truncated version is used as shown, imposing an energy cutoff at the x-intercept of potential energy function.

Hoover thermostat, with velocities sampled from a Gaussian distribution ensuring zero angular momentum. The timestep in MD-simulations is set to 0.005τ in Lennard-Jones reduced units (with unit LJ parameters). Between strain increments there are $1,500\tau$ and 2.1 million SGCMC swap moves. As this is a Monte Carlo simulation, the timestep is mostly relevant for the damping parameter of the Nose-Hoover thermostat, which is set to 100τ, in order to reach the prescribed temperature.

Simulation box details

In the two-dimensional SGCMC-simulations, we use a triangular lattice, where the reference bond lengths are $r_0 = 1$ in reduced units. The simulation box is a 72 x 42 lattice in a periodic box of side lengths $L_x = 72r_0$ x $L_y = 42\sqrt{3}r_0$, with 2 atoms in the unit cell for a total of $6,048$ atoms and $18,144$ bonds (coordination number of the triangular lattice is 6).

For three-dimensional SGCMC-simulations, we consider a face-centered cubic (FCC) lattice, with scale factor $\sqrt{2}$, for the reason of keeping identical the reference bond length, $r_0 = 1$ in reduced units (shown in Fig 2-2). The simulation box is a 10 x 10 x 10 lattice in a periodic box of side length $L_0 = 10\sqrt{2}r_0$, with 4 atoms in the unit cell for a total of $4,000$ atoms and $24,000$ bonds (coordination number of the FCC lattice is 12).

Simulations are carried out with the LAMMPS Molecular Dynamics Simulator [71] and visualizations are created using the Open Visualization Tool (OVITO) [72].

2.4.1 Extended methods for two-phase composites

In this section we outline the simulation models created for studying heterogeneous fracture in Chs. 4-6, considering two- and n- phase composites in two and three dimensions.

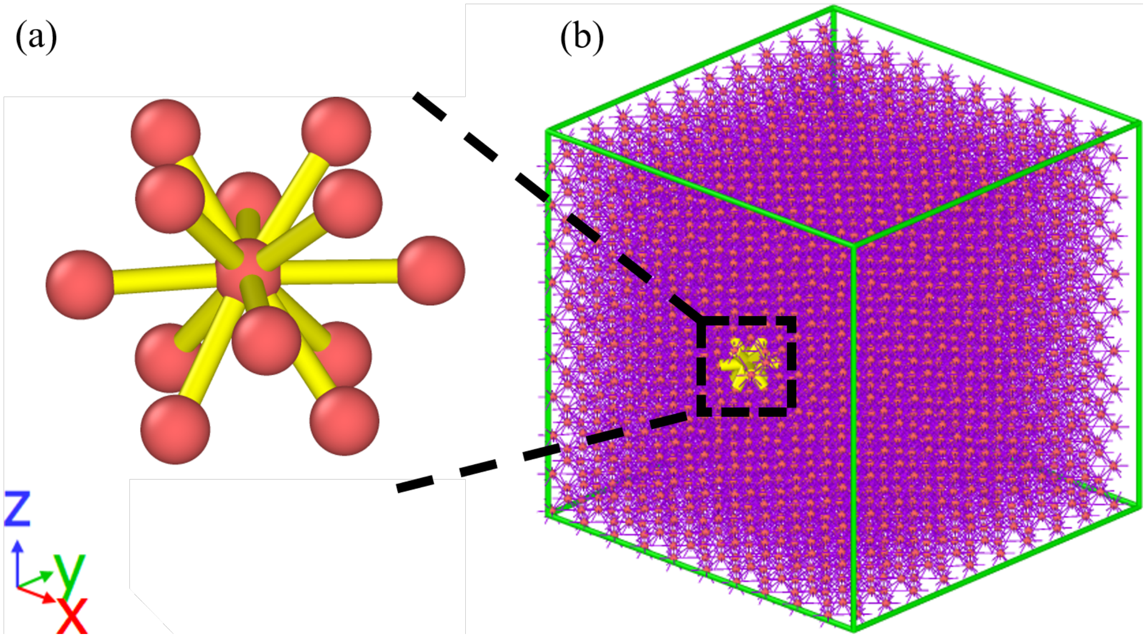

Figure 2-2: Bonds and mass points in the face-centered cubic (FCC) lattice. Three-dimensional simulations are performed with this FCC lattice. (a) A close-up view of the bonds (yellow tubes) and mass points (red spheres) shows what the semigrand canonical moves act on when they toggle bonds ON and OFF. (b) The full 10 x 10 x 10 FCC lattice with all the $4,000$ mass points and $24,000$ bonds (in purple). The green cube shows the edges of the periodic box.

Composites

Two-phase composites are considered in this study where each composite is made up of a combination of phase A and any one of possible J phases shown in Fig. 2-3(d). The phases are differentiated on the basis of their energy parameters. The energy parameters are related to the groundstate, ϵ_0, and stretching, ϵ_λ, terms of the potential energy formulation. Varying the elasticity mismatch, $\kappa_\lambda = \frac{\epsilon_\lambda^J}{\epsilon_\lambda^A}$, can lead to stiffer ($\kappa_\lambda > 1$) or more compliant ($\kappa_\lambda < 1$) composites. Varying the groundstate mismatch, $\kappa_0 = \frac{\epsilon_0^J}{\epsilon_0^A}$ can create weaker ($\kappa_0 < 1$) or tougher ($\kappa_0 > 1$) composites. Nominally, with respect to the baseline phase A, addition of a J phase from the β region in Fig. 2-3(d) will create a composite with higher fracture resistance than phase A, and the converse is true when adding a J phase from the α region. When performing simulations with composites a range of 21 to 22 different volume fractions is considered to capture composite material response.

Geometries

For each composite we arrange the phases into two different regular geometries or textures, and one random geometry (R) where we randomly assign the bonds to one of two phases. The regular geometries are layered (L) and checkerboard (K). Depictions at 50% volume fraction of these geometries are shown in Fig. 2-3. Under uniaxial stretching in parallel and perpendicular to the fibers, the layered composites correspond to the Voigt and Reuss stiffness bounds, respectively.

Loading

Each composite and each geometry, is subjected to uniaxial tension, simple shear, and biaxial tension through displacement-controlled boundary conditions. Displacement-control is necessary when performing simulations in a quasi-static Monte Carlo setting to circumvent unstable fracture. The orientation study in Chapter 6 applies displacement loading conditions following loading conditions specified by a strain Mohr circle, and further details are left to that chapter.

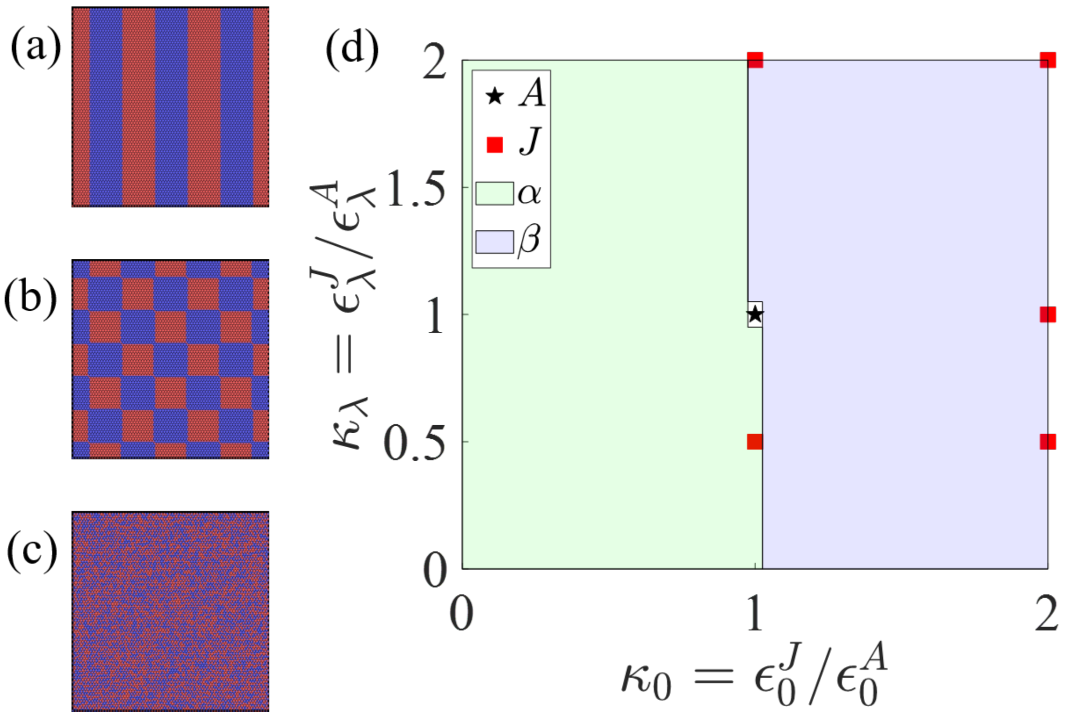

Figure 2-3: Geometries used to model heterogeneity in 2-D and 3-D composites and parameter space of composites around the baseline phase A. Geometries used to model heterogeneity in 2-D composites are shown at 50% volume fraction: (a) layered, (b) checkerboard, and (c) random. (d) Parameter space of all the J phases in terms of energy parameters normalized by phase A values.

2.4.2 Three-dimensional two-phase composites

We construct the prototypical geometries, the checkerboard and random geometries, in a face-centered cubic (FCC) lattice. The only difference arises for the checkerboard pattern, where in order to make the lattice dimension divisible by 6 layers, the three-dimensional lattice is of dimensions 12 x 12 x 12. The random geometry, on the other hand, is the standard 10 x 10 x 10 FCC lattice previously defined, except the bonds are not all identical to make it a random geometry. Fig. 2-4 shows the three-dimensional versions of the checkerboard and random geometries.

This chapter presents the simulations methods that are common to Ch. 3 through Ch. 7, where further details are needed they will be discussed in their respective chapters. Specifically the loading conditions for the orientation study are discussed in Chapter 6.

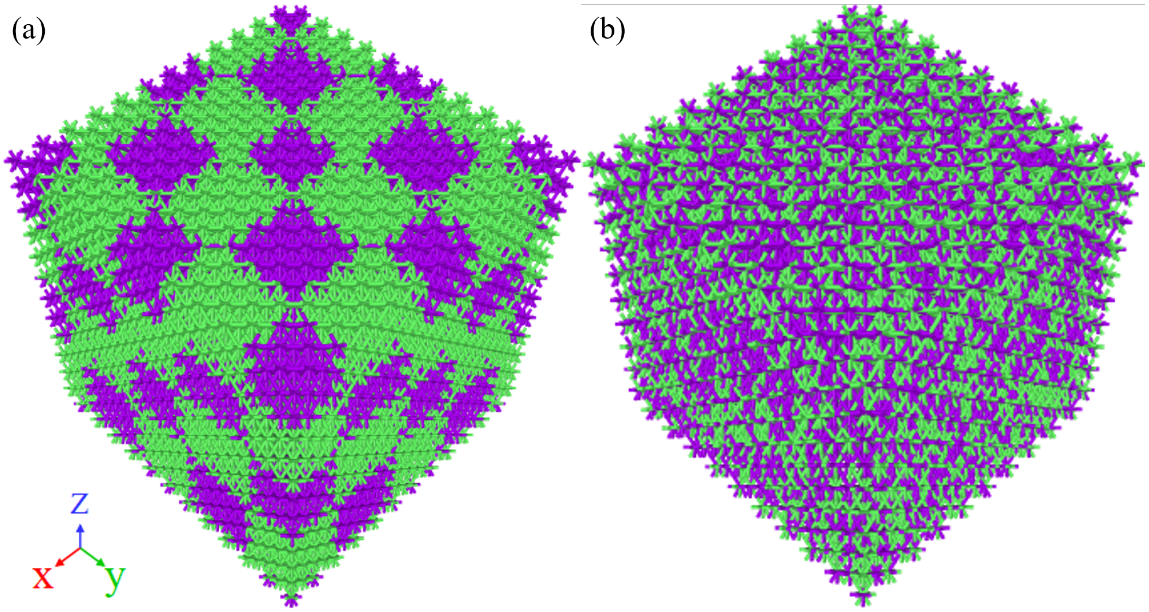

Figure 2-4: Checkerboard and random geometries in three dimensions, shown for $f_\beta = 50\%$. Three-dimensional reference lattices of the (a) checkerboard and (b) random geometries, shown omitting the mass points. Lattice dimension are 12 x 12 x 12 and 10 x 10 x 10 for the checkerboard and random geometries, respectively. Phase A and B bonds are purple and green, respectively.

Chapter 3

Phase diagram of brittle fracture in the semigrand canonical ensemble

We present a novel simulation method to assess the quasi-static fracture resistance of materials. Set within a semigrand canonical Monte Carlo (SGCMC) simulation environment, an auxiliary field –the bond rupture potential– is introduced to generate a sufficiently large number of possible microstates in the semigrand canonical ensemble, and associated energy and bond fluctuations. The SGCMC approach permits identifying the full phase diagram of brittle fracture for harmonic and non-harmonic bond potentials, analogous to the gas-liquid phase diagram, with the equivalent of a liquidus line ending in a critical point. The phase diagram delineates a solid phase, a fractured phase and a gas phase, and provides clear evidence of a first-order phase transition intrinsic to fracture. Moreover, energy and bond fluctuations generated with the SGCMC approach permit determination of the maximum energy dissipation associated with bond rupture, and hence of the fracture resistance of a widespread range of materials that can be described by bond potentials.

3.1 Gedankenexperiment

Consider a solid composed of particles subjected to a volume change at constant temperature. The system is further subjected to an external energy source that targets the bonds in the system, akin to a bulk radiation source. At a given energy of this radiation source, denoted by $\Delta\mu$, fracture at the macroscopic level of the sample may occur between two equilibrium states of the system. This transition is defined by the bond rupture potential, $\Delta\mu$, the prescribed volume, V, and temperature, T. In this semigrand canonical ensemble, we measure the ensemble energy average of possible microstates of the system, $\langle U \rangle$, and the energy fluctuations, in function of the average number of bonds, $\langle N \rangle$, and their fluctuations. As we repeat the experiment by sweeping possible values for volume changes, stress-strain curves can be traced out for different prescribed bond potentials, $\Delta\mu$ [Fig. 3-1(a-b)]. Similarly, sweeping all possible values of $\Delta\mu$ we obtain characteristic bond isochores, $\langle N \rangle - \Delta\mu$, for different prescribed volume strains [Fig. 3-1(c-d)].

The described thought-experiment aims at addressing some unsolved issues in fracture mechanics, such as homogenization of fracture properties of heterogeneous solids, which cannot be satisfactorily resolved with classical continuum theories based on Griffith's 1921 energy-based quasi-static fracture approach [1, 73], that requires notches and other discontinuities to trigger fracture propagation, local stress intensities [5], and cohesive crack zones [8, 74–76] to determine the fracture resistance of solids. More contemporary simulation approaches have extended the realm of classical fracture mechanics to discrete (incl. molecular) fracture processes [27, 77, 78]. Statistical lattice-based models of fracture addressed size effects of materials' strength, bursts of microfailures, and morphology of cracks [27, 33, 78–80]. Others consider the competition between crack propagation and dislocation mechanisms [81–83]; role of interatomic and mean force potentials [19, 84–87]; role of phonons [85, 88, 89]; crack velocity and dynamic instability [87, 90–93], crack growth kinetics of microcracks in crystals [94]; effect of crystal orientation, grain boundaries, texture, chemical environment, and impurities [17, 91, 95–100]. Compared to this rich and insistently increasing body of fracture literature, our approach differs in two fundamental aspects: (1) it defines the fracture process as bond rupture in the semigrand canonical ensemble ($\Delta\mu VT$), in contrast to the canonical (NVT) and microcanonical (NVE) ensembles that restrain our current knowledge of the physics of fracture processes; and by do-

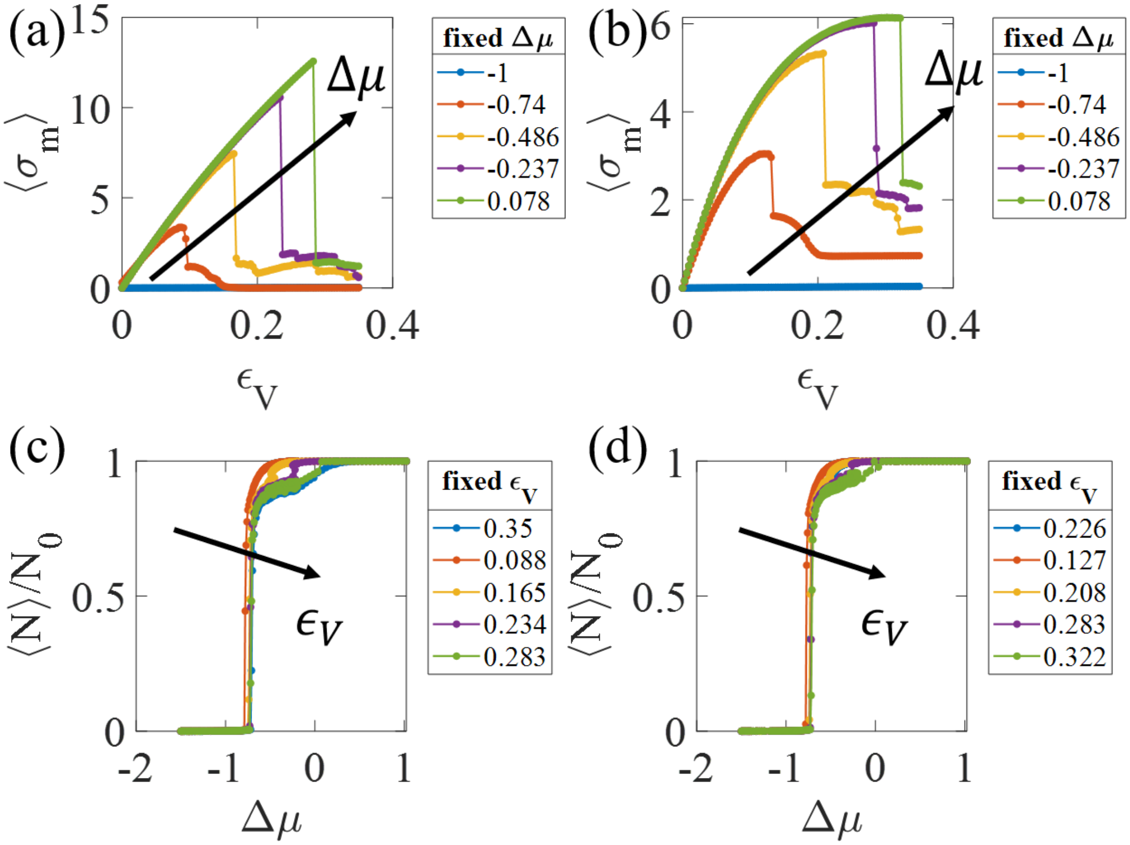

Figure 3-1: Work-conjugate pairs in the semigrand canonical Ensemble. At fixed bond potential, $\Delta\mu$, successive MC simulations at different prescribed strains trace out a stress-strain curve for (a) harmonic and (b) Morse potential. For a fixed volume strain, at different $\Delta\mu$, bond number, N, is measured generating bond isochores for (c) harmonic and (d) Morse potential.

ing so (2) it enables a new understanding of fracture resistance of solids, in terms of energy and bond fluctuations, in the $\Delta\mu VT$ ensemble.

We start by rationalizing the thought-experiment into a simulation framework for equilibrium-based fracture analysis. First, we perform the thought-experiment by means of almost classical Monte Carlo simulations [68], with one exception: instead of inserting or deleting randomly selected particles (GCMC), the acceptance criterion in the SGCMC approach changes the identity of bonds:

$$acc\,(o \to n) = \min\,(1, p_{o\to n}) \tag{3.1}$$

where $p_{o\to n}$ stands for the probability of either switching a bond from OFF to ON, $(N \to N+1)$, or from ON to OFF $(N \to N-1)$:

$$p_{N\to N+1} = \exp\left[\frac{1}{k_B T}\left(+\Delta\mu - \Delta U_{N\to N+1}\right)\right] \tag{3.2a}$$

$$p_{N\to N-1} = \exp\left[\frac{1}{k_B T}\left(-\Delta\mu - \Delta U_{N\to N-1}\right)\right] \tag{3.2b}$$

with $\Delta U_{o\to n} = U_n - U_o$ the difference in potential energy of microstate $\mathcal{M} = (o, n)$.

3.2 Phase diagram of brittle fracture

We now corroborate the predictive power of the proposed SGCMC bond-fracture approach. For illustration, we consider a 10x10x10 face-centered cubic (FCC) lattice with 4 atoms in each unit cell ($4,000$ atoms in total, $N_0 = 24,000$ bonds), and periodic boundary conditions. Simulations start with fully bonded particles. Two types of bond potentials are considered: a truncated harmonic potential and the Morse potential [101]. We begin with an analysis of recorded stress-strain curves [Figs. 3-1(a-b)]. In the semigrand canonical ensemble, we prescribe the volume in the form $V = V_0(1+\epsilon_V)$, where V_0 is the volume of the undeformed simulation box, and ϵ_V the volume strain. In this displacement-controlled test set-up, simulations are carried out at different volume strains, whereas the bond potential, $\Delta\mu$, is held constant over the entire range of the volume strain applied. The displacement-controlled test set-up is repeated for different values of $\Delta\mu$. The impact of the prescribed bond potential on the stress-strain response is shown in Figs. 3-1(a-b), in form of a decrease in stress-strain capacity with decreasing bond potential. Alternatively, in a bond potential-controlled set-up, we analyze the work-conjugated bond number N at constant volume strain, i.e. the bond isochores [Figs. 3-1(c-d)]. Akin to a gas, the number of bonds goes to zero as the bond potential tends to negative values; whereas no bonds break when bond potential tends to positive values. The bond isochores [Figs. 3-1(c-d)] provide a means to understand the flattening of the stress-strain response [Figs. 3-1(a-b)] with decreasing bond potential. Indeed, the lowering of the bond potential entails bond breakage, which ultimately shifts the system from a bonded solid state to an unbonded gas-like state.

The analysis of the stress-strain diagrams and bond isochores calls for a generalization in form of a phase diagram. This is achieved by sweeping the $(\Delta\mu, V)$ phase space in search of phase boundaries defined by the pair of coordinates at which fracture occurs, namely the critical bond rupture potential $(\Delta\mu_{crit} = \Delta\hat{\mu}_{crit}\left(\langle N\rangle_{crit}\right))$ and the critical volumetric strain $(V_{crit} = V_0(1+\epsilon_{V_{crit}}))$. Construction of phase diagrams is done through repeated simulations iterating over different bond rupture potentials $\Delta\mu$ and volumes V in different $\Delta\mu VT$ ensembles. Once relaxed, Monte Carlo simulations are carried out for each strain-controlled test (volume V_k) at a given prescribed bond rupture potential, $\Delta\mu_j$, representative of the $\Delta\mu_j V_k T$ ensemble. That is, to sweep the $(\Delta\mu, V)$ phase space, a total of $j \times k$ individual Monte Carlo simulations for each choice of prescribed energy functional (harmonic or Morse) are carried out. Starting with a fully bonded system, $N = N_0$, displacement loading is applied first before Monte-Carlo simulations in the $\Delta\mu_j V_k T$ ensemble are performed. Fig. 3-2 displays the phase diagrams for the harmonic and Morse potentials, including the transition lines between solid and gas state of the system.

Irrespective of the bond potential, the phase boundary begins with a near vertical line delineating the minimum bond rupture potential below which the system is effectively a gas (domain I), and above which the bonded system is fractured or

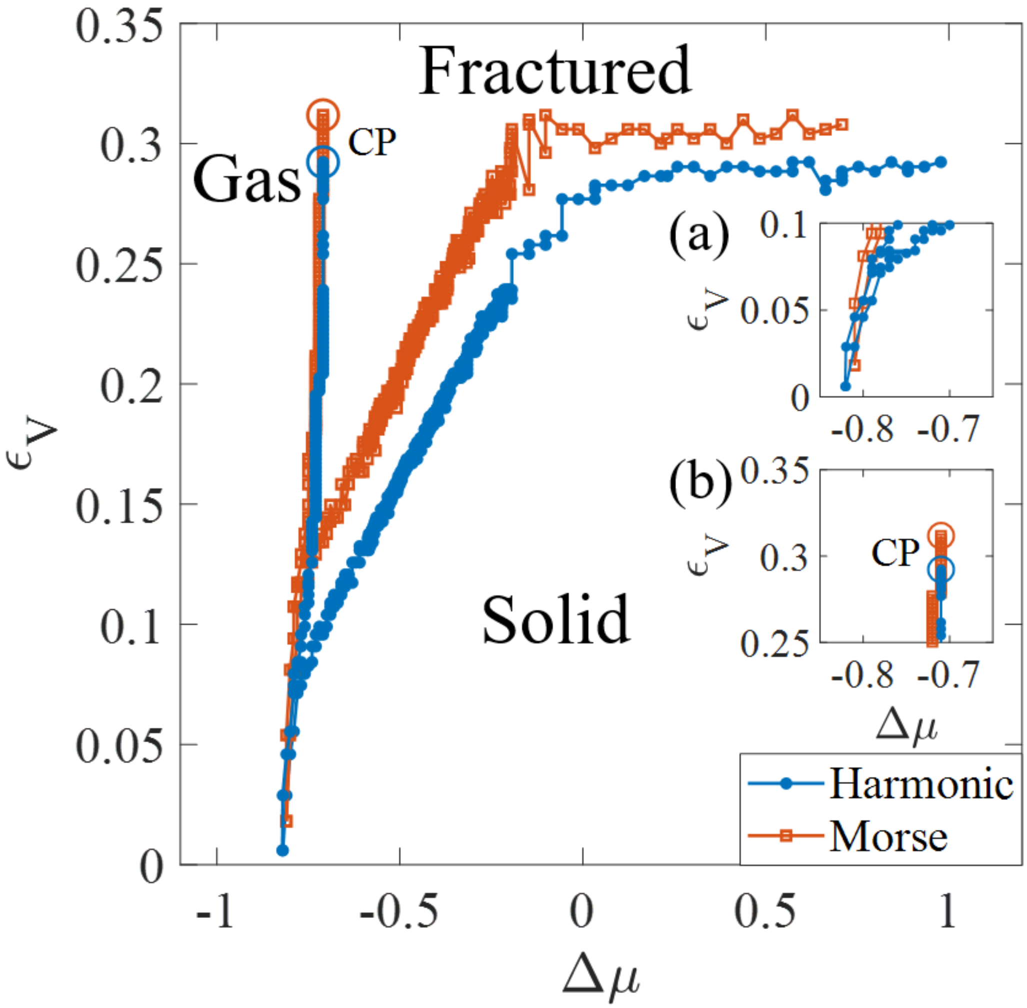

Figure 3-2: Phase diagrams of brittle fracture for harmonic (closed circles) and Morse (open squares) bond potential systems. The phase diagram is characterized by three domains corresponding to I) $\Delta\mu < \Delta\mu_{gas}$: the system is a collection of non-interacting particles and cannot undergo fracture. The line terminates in a critical point, CP (near-vertical line, $\Delta\mu$-controlled); II) $\Delta\mu_{gas} \leq \Delta\mu \leq 0$: solid undergoes fracture when $\epsilon_V > \epsilon_{V_{crit}}$ or $\Delta\mu < \Delta\mu_{crit}$ (sloped line); and III) $\Delta\mu > 0$: fracture is controlled by constant $\epsilon_{V_{crit}}$ (flat line). Insets: (a) Near zero strain the phase boundaries meet at a triple point. (b) Liquidus lines terminate at a CP.

a solid. In this domain, the phase diagram has much in common with classical pressure-temperature phase diagrams of pure substances, when considering the prescribed strain as the analogue of temperature, the prescribed bond rupture potential as the analogue of pressure, and the fractured state as analogue of the liquid phase. In fact, the phase line starts at a triple point close to $\epsilon_V = 0$ (inset (a) in Fig. 3-2), and terminates in a critical point, CP (inset (b) in Fig. 3-2). In between these two, we recognize – by analogy with pressure-temperature phase diagrams – the existence of a liquidus line, along which the bond rupture potential has such a low value that bonds dissolve (rather than fracture due to bond stretching) independent of the applied strain. The system is thus reduced to a collection of non-interacting particles. In this unbonded ($N = 0$) gas-like state there are effectively no interactions. Mapped onto the pressure-temperature analogy, the measured critical exponents near the critical point where the liquidus line ends, fall in the range of $0.1075 < \alpha < 0.114$, when extending the analogy to include the mean stress as the analog of the isochoric heat capacity in the Ising model. Similarly, taking the bond number as the analog of the magnetic order parameter, we can measure $0.3246 < \beta < 0.3292$, (see Fig. 3-3), in close agreement with the values of the three-dimensional Ising model ($\alpha = 0.1096$ and $\beta = 0.32653$ [102]). This shows that the proposed SGCMC-model around the critical point exhibits similar features as the compressible Ising model [103], which merits further exploration.

The remaining part of the $(\Delta\mu, \varepsilon_V)$ phase diagram defines the phase transition between the solid and the fractured phase. The solid–fracture phase transition is a first order phase transition, as all work-conjugated energy derivatives (i.e., mean stress, bond number) exhibit discontinuities at fracture. Specifically, these quantities exhibit jump discontinuities at a critical value corresponding to the crossing of the phase boundary, shown for $\Delta\mu_{crit} = 0.033$ and $\varepsilon_V^{crit} = 0.3216$ in Fig. 3-4. Moreover, these discontinuities occur in the first order derivative of the energy; namely: the mean stress, $\sigma_m = \partial U/\partial\varepsilon_V$, bond number, $N = -\partial U(= -k_B T \ln \Upsilon)/\partial\mu$, and heat of bond rupture, $q_{br} = -\partial U/\partial N$, where Υ is the semigrand canonical partition function. The combination of these observations unambiguously defines fracture at the crossing

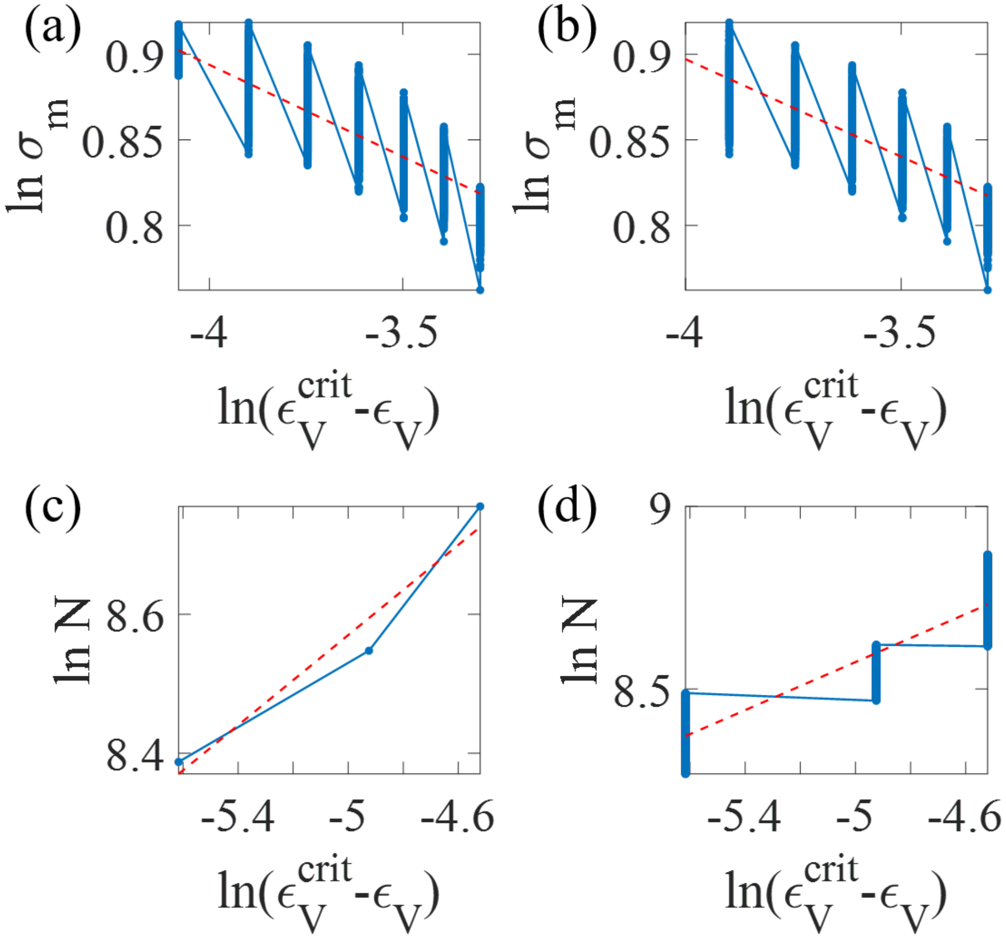

Figure 3-3: Critical exponents fit from the simulation results. Lower and upper bounds of the fits (red dashed lines) for the stress critical exponent, α, (a and b, respectively) as well as for the bond number critical exponent, β, (c and d, respectively) are in good agreement with the same exponents in the Ising model.

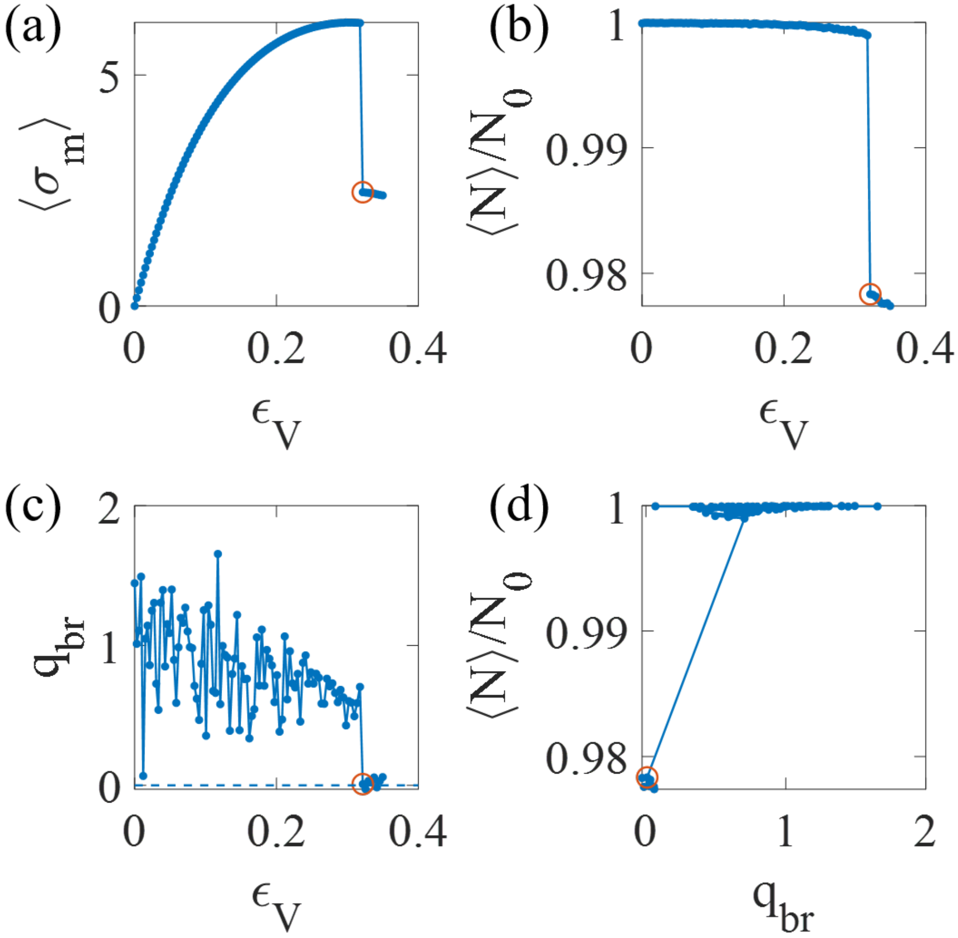

Figure 3-4: First order phase transition of brittle fracture: Jump discontinuities in (a) stress, (b) bond number, and (c) heat of bond rupture occur at the same point (red open circles) $q_{br} = 0$ as predicted by the fluctuation-dissipation approach to fracture mechanics.

of the phase boundary as a first order phase transition.

Furthermore, the phase boundaries exhibit a characteristic shape, namely a phase line with a finite slope for $\Delta\mu_{gas} < \Delta\mu < 0$ (domain II) and a horizontal line defined by a constant maximum critical strain for $\Delta\mu > 0$ (domain III). In domain II, the solid region is characterized by strains below the phase boundary, $\epsilon_V < \epsilon_{V_{crit}}$, corresponding to stress-strain curves with a positive slope [Figs. 3-1(a-b)] and by bond rupture potentials to the right of the phase boundary, $\Delta\mu > \Delta\mu_{crit}$, in accordance with the bond isochores [Figs. 3-1(c-d)]. In contrast, domain III ($\Delta\mu > 0$) is characterized by a maximum critical stress and strain at fracture. Increasing the bond rupture potential does not yield higher strains at fracture. These observations explain the (close to) zero-slope of the phase boundary in the $(\Delta\mu, \varepsilon_V)$-space. If we remind ourselves that classical fracture mechanics operates at $\Delta\mu = 0$ with notches or other initial discontinuities to trigger fracture propagation, we recognize from analyzing the phase diagram that $\Delta\mu = 0$ defines the onset of the maximum critical strain capacity of any (un-notched) material, and that this critical strain holds for higher positive values of bond rupture potential as well (Fig. 3-2). This suggests that the constant critical strain delineating the solid-fracture phase transition is an order parameter.

To further characterize the different phases of the system, Fig. 3-5 displays the radial distribution functions (RDFs) obtained from simulations, together with characteristic sample snapshots of the particle energies. The RDFs illustrate the impact of fracture on relative position of the particles in consequence of the energy release due to bond breakage. In fact, as the system is strained from the undeformed reference configuration (Fig. 3-5a) to just before fracture (25.2% strain, $\Delta\mu = -0.354$, Fig. 3-5b) the RDF shifts to higher distance values as energy is stored into the stretched bonds. After fracture (25.6% strain, Fig. 3-5c), a part of this energy is released in bond breakage across a crack surface which leads to a visible shift of the RDF to the left. Finally, for domain I we obtain an RDF (shown for $\Delta\mu = -1$, Fig. 3-5d) reminiscent of an ideal gas of non-interacting particles, with a first shell distance peak much smaller than the reference FCC lattice distance. Before catastrophic failure, damage is sustained in the system through a series of microcracks that form randomly throughout the material. Precursory to the macrocrack formation, several microcracks are created throughout the entire system. At a critical strain, the fluctuating number of microcracks exhibits collective behavior marked by percolation across the entire sample to form the macrocrack as shown in the simulation snapshots in Fig. 3-6 [104]. This microcrack formation is heterogeneous even in the case of a homogeneous reference lattice.

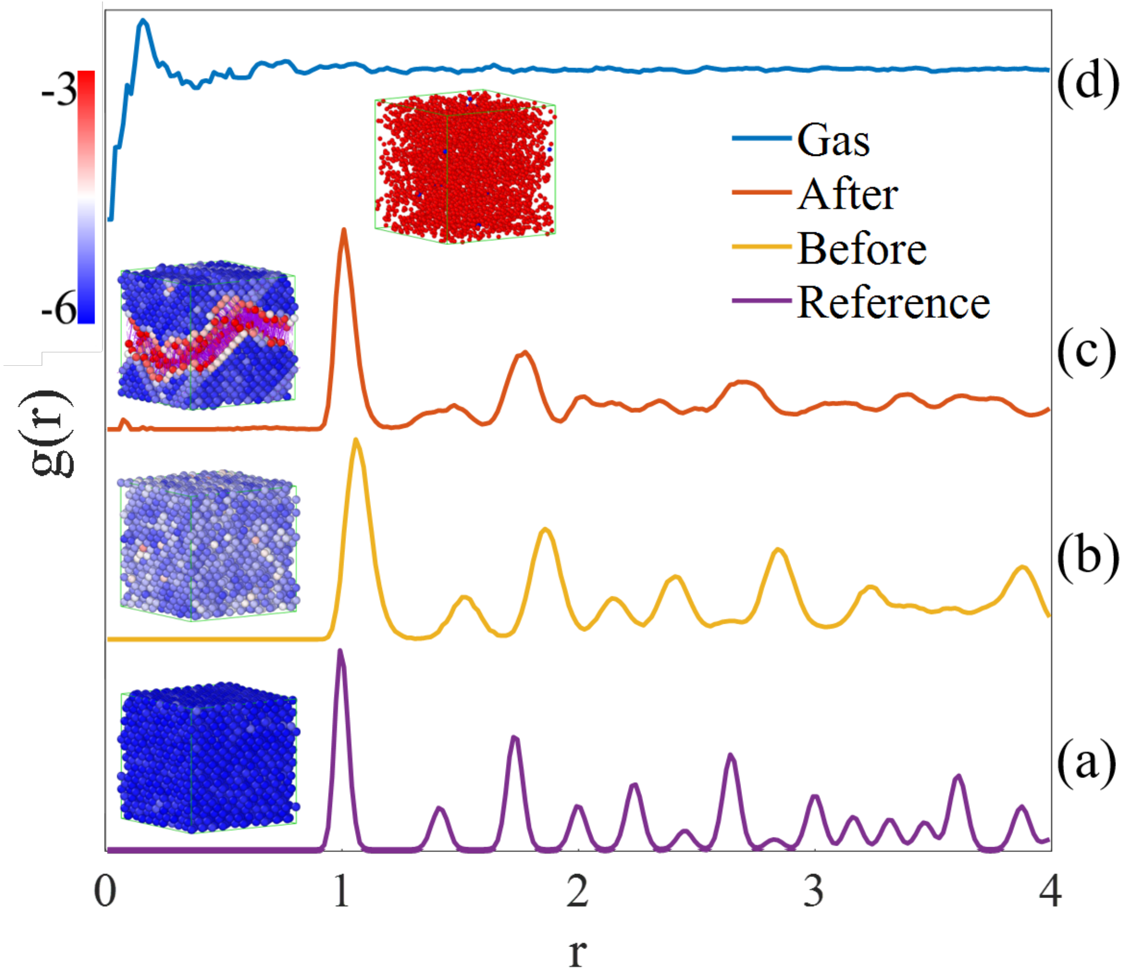

Figure 3-5: Radial distribution functions around fracture and in the gas phase. Starting from (a) the reference (unstrained) state, the system is (b) stretched, storing energy and shifting the RDF peaks to higher lattice distances. Comparing the RDFs before and after fracture, (c) peaks are noticeably shifted back to lower distances, indicative of a fracture-induced energy release in the system. (d) The gas RDF approaches ideal gas behavior as the system is a set of non-interacting particles. (Insets) color-coded simulation snapshots of the potential energy (colorbar on the far left).

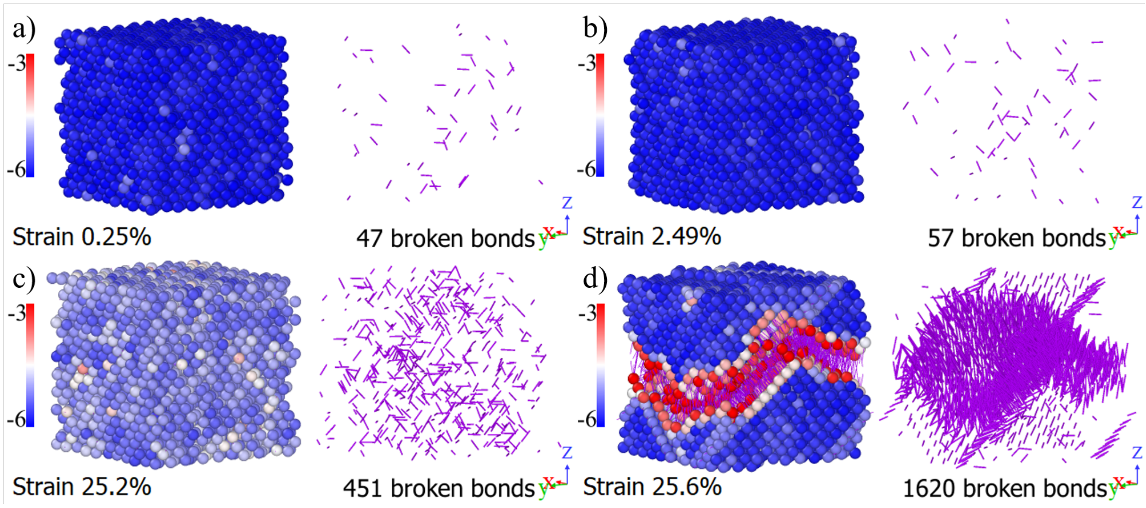

Figure 3-6: Percolation of macrocrack from assembly of microcracks. In each panel, evolution of the mass point potential energy in function of strain is shown on the left, while the right shows corresponding images of the broken bonds. Simulation snapshots are shown for (a) 0.25%, (b) 2.49%, (c) 25.2%, and (d) 25.6% volumetric strain. As strain is increased a small number of bonds are broken erratically over the entire sample. At fracture, there is a drastic drop in potential energy (becoming less negative) as the broken bonds percolate across the entire sample rendering the material unable to transmit load over the newly created traction-free crack surfaces. With $N_0 = 24,000$, $1,620$ broken bonds in (d) amounts to 6.75% of the total number of bonds.

3.3 Heats of bond rupture

The last focus of our analysis is to quantitatively pin down the fracture resistance of the material. This is achieved by considering (1) the bond number fluctuations, $\mathrm{Var}\,(N) = \langle N^2 \rangle - \langle N \rangle^2$; and (2) the associated energy fluctuations, $\mathrm{Cov}\,(U, N) = \langle UN \rangle - \langle U \rangle \langle N \rangle$. These fluctuations, outputs from the SGCMC simulations, are key to assessing the fracture resistance of a material. In fact, akin to adsorption processes [105, 106], equate energy fluctuations with the heat of bond rupture [107]:

$$q_{br} = -\frac{\partial \langle U \rangle}{\partial \langle N \rangle} = -\frac{\mathrm{Cov}\,(U, N)}{\mathrm{Var}\,(N)} \tag{3.3}$$

Then, split the total energy U in two parts, one related to the groundstate energy of the system, $U^0 = \sum_i^N U^i \left(\overrightarrow{r}_i\right)$, representative of the internal bond energy (cohesion) in the absence of any deformation of the system, the other related to the deformation in consequence of e.g. two-body interactions between particles i, j, $U^\lambda = \sum_{i,j}^N U^{ij} \left(\overrightarrow{r}_{ij} = \overrightarrow{r}_j - \overrightarrow{r}_i\right)$. Consequently, a critical value of the bond rupture resistance can be defined at which the heat associated with the change in strain energy, $\left(q_{br}^\lambda = -\partial \left\langle U^\lambda \right\rangle / \partial \langle N \rangle\right)$, is equal with opposite sign to the heat release due to groundstate energy release, $\left(q_{br}^0 = -\partial \langle U^0 \rangle / \partial \langle N \rangle\right)$; that is for $q_{br} = 0$:

$$q_{br}^\lambda = -\frac{\mathrm{Cov}\left(U^\lambda, N\right)}{\mathrm{Var}\,(N)} \equiv -q_{br}^0 = \frac{\mathrm{Cov}\,(U^0, N)}{\mathrm{Var}\,(N)} \tag{3.4}$$

Expression (3.4) is nothing but Griffith's quasi-static fracture criterion [1] expressed in terms of energy fluctuations: $-q_{br}^\lambda$ is the bond energy release rate (analogous to Griffith's energy release rate [73]), and q_{br}^0 its critical value (analogous to Griffith's fracture energy). In this sense, for $-q_{br}^\lambda < q_{br}^0$, there are still enough strain energy reserves in the system to redistribute the elastic strain energy due to a prescribed volume change without further bond breakage. This process can be associated with a stable bond fracture process. In contrast, for $-q_{br}^\lambda > q_{br}^0$, the system has exhausted its maximum energy release capacity, defined by Eq. (3.4), releasing more groundstate energy in form of heat than redistributing work internally in form of recoverable energy. This is shown in Fig. 3-7 for the three domains identified from the phase diagram. It is of interest to condense these results into simplified bond fracture criteria. To this end, consider the probability of switching a bond ON, $p_{N\to N+1}$, equal to the probability of switching a bond OFF, $p_{N\to N-1}$, and rewrite the acceptance criteria (3.2), while approximating the change in energy by $\Delta U_{N\to N+1} \simeq \partial \langle U \rangle / \partial \langle N+1 \rangle = -q_{br}$:

$$\exp\left[\beta\left(\Delta\mu + q_{br}\right)\right] = \exp\left[\beta\left(-\Delta\mu - q_{br}\right)\right] \tag{3.5a}$$

$$\Delta\mu = -q_{br} = -q_{br}^{0} - q_{br}^{\lambda} \tag{3.5b}$$

Eqs. (3.5) suggest two limit states that link the external fields $(\Delta\mu, V, T)$ to the fracture resistance q_{br}^{0}; i.e. $0 \leq -q_{br}^{\lambda} = q_{br}^{0} + \Delta\mu \leq q_{br}^{0}$ (noting that $-q_{br}^{\lambda} > 0$). Furthermore, the bond rupture potential exhibits two bounds, $-q_{br}^{0} \leq \Delta\mu \leq 0$. The upper bound of Eq. (3.5b), $\Delta\mu = 0$, coincides with definition (3.4) of the critical bond energy release rate, and is thus recognized as the critical fracture point, associated with the maximum release of strain energy due to the dissipation of groundstate energy. The bound of $\Delta\mu = 0$ also marks the point of equilibrium of the bond rupture potentials where $\Delta\mu = \mu_{OFF} - \mu_{ON} = 0$. The lower bound $\Delta\mu = -q_{br}^{0}$ can be attributed to the depletion of the energy storage of the bonds before any strain is applied in accordance with Eqs. (3.2) and (3.5a). Such a drastic shift in energy content of the bonds pushes the system into a gas-like state where the most favorable configuration of the system has no bonds, $N = 0$. The actual lower bound found from simulations, while close to $-q_{br}^{0}$, is denoted by $\Delta\mu_{gas}$ in order to reflect its deviation from the predicted value and to associate it with the gas phase of the system for $\Delta\mu < \Delta\mu_{gas}$. In between these two limit states the effect of the bond rupture potential on the potential energy of the system is absorbed by q_{br}^{λ} in the acceptance probabilities of the SGCMC moves, and therefore visible from the bond number of the system. These limit states are summarized by the following set of fracture criteria in function of the bond rupture potential across the considered domains I, II, and III:

$$q_{br} = q_{br}^{0} \begin{cases} 1 & \Delta\mu < \Delta\mu_{gas} \qquad (I) \\ \frac{\Delta\mu}{\Delta\mu_{gas}} & \Delta\mu_{gas} \leq \Delta\mu \leq 0 (II) \\ 0 & \Delta\mu > 0 \qquad (III) \end{cases} \tag{3.6}$$

The agreement of the fracture criteria (3.6) with simulation results for the entire phase space is shown in Fig. 3-7. Specifically, domain I corresponding to the gas phase exhibits no fracture, since the system has no bonds to carry load. This results in a zero heat of stretching ($q_{br}^{\lambda} = 0$, thus $q_{br} = q_{br}^{0}$). Domain II is characterized by a solid phase where fracture occurs before complete exhaustion of the groundstate energy of the material along fracture surfaces; hence $q_{br} > 0$. Finally, domain III corresponds to the solid phase where fracture occurs when the heat associated with the change in strain energy is equal with opposite sign to the heat due to groundstate energy release in accordance with Eq. (3.4).

3.4 Conclusions

In summary, we have shown that quasi-static fracture mechanics in the semigrand canonical ensemble provides a versatile means to determine phase diagrams of brittle fracture of solids. Modularity of the framework with respect to choice of energy potential and geometry leaves open avenues for investigation of fracture of heterogeneous materials. While heats of bond rupture in the context of fracture have not been measured, the simulation measurements can still be compared to existing fracture resistance measurement techniques. Furthermore, heats of bond rupture formulated in this work can — at least theoretically — be measured through calorimetry experiments. This work can lead to better understanding and implementation of such experiments in the future. Furthermore, the approach permits assessment of the fracture resistance of materials based upon fluctuations without the need to concentrate these fluctuations into notches and other discontinuities. The fact that the proposed

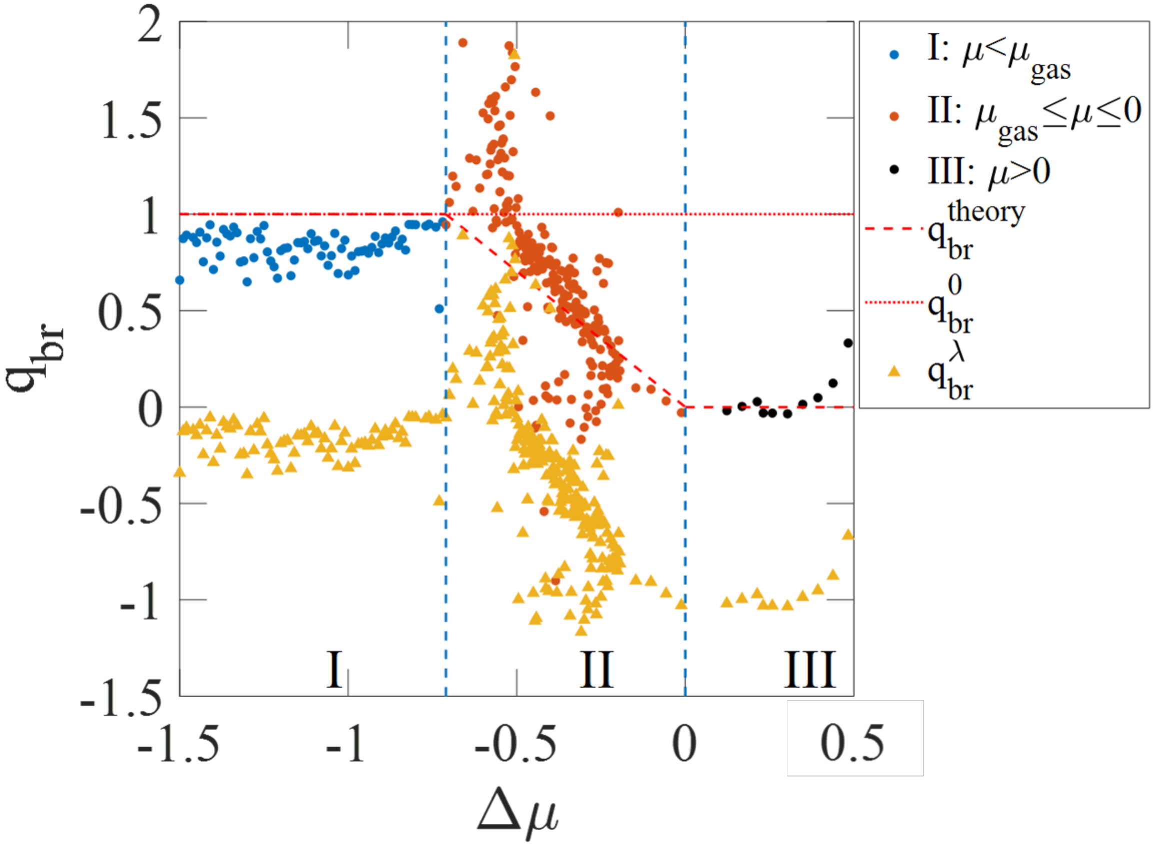

Figure 3-7: Heat of bond rupture when crossing phase boundaries. There is no unique condition for fracture across all values of imposed bond rupture potential, across all domains. This is evidenced by the value of the heat of bond rupture when crossing a phase boundary in the different domains I, II, and III. Instead the value of q_{br} when crossing a phase boundary serves to identify the different domains or phases of brittle fracture across all possible values of bond rupture potential.

semigrand canonical method is not limited by bond potential expressions and geometric texture of materials provides a promising venue to investigate fracture phenomena of heterogeneous materials with reference to the intimate interplay between structure and fracture resistance.

Chapter 4

Fluctuation-based fracture mechanics of heterogeneous materials

We present results of a hybrid analytical-simulation investigation of the fracture resistance of heterogeneous materials. We show that bond-energy fluctuations sampled by Monte Carlo simulations in the semigrand canonical ensemble provide a means to rationalize the complexity of heterogeneous fracture processes, encompassing probability and percolation theories of fracture within a unified framework of fluctuation-based fracture mechanics. For a number of random and textured model materials, we derive upper and lower bounds of fracture resistance, which are critical to identify toughening mechanisms. Specifically, elastic toughening mechanisms due to elastic energy mismatch are shown to result from both the activation of cooperative interactions in soft-tough bulk phases, and the transition from critical to subcritical bond fracture percolation in textured materials. While counter-intuitive on first sight, this soft-tough paradigm can explain a number of experimental observations, including toughening of brittle solids by deformable polymers or organics, such as gas shale, nacre, stress-induced transformational toughening mechanisms in ceramics, and toughening of sparse elastic networks in hydrogels, to name a few.

4.1 Fracture mechanics of heterogeneous materials

Fracture of heterogeneous materials remains an important topic amid the backdrop of an ever-increasing demand for new materials specifically designed to overcome intrinsic trade-offs between competing material properties within composites [108–110], porous media [100, 111], additively manufactured materials [112–114], and biological or bioinspired tissues [115–118]. However, this ever expanding roster of heterogeneous materials has yet to find a consolidating theory of fracture mechanics, which bridges between two apparently disparate lines of advanced theories. On the one hand, early approaches based on Griffith's energy release rate [1, 6] and Irwin's stress intensity factor [4, 5] provide useful insights into benchmark phenomena in fracture of textured matrix-inclusion composites, such as crack trapping or bridging by arrays of obstacles (e.g. particles) [47, 50, 53, 119], crack deflection, shielding or penetration at interfaces of dissimilar solids [48, 49, 51] and so on, which continue to reverberate in contemporary computational fracture mechanics of multiscale composites (see, for instance, [19, 120, 121]) and composite material design [52, 54–57]. On the other hand, statistical models of fracture in disordered materials have been derived from extreme value theory [26, 28, 122], applied to random fiber-bundle [24] and lattice models [27, 123, 124], including their electric analogs, random fuse networks [25], presenting an initial disorder in, or random field of, fracture strength or fracture strain threshold. Motivated by the intimate interplay of disorder and long-range correlations in fracture [29], such statistical physics approaches point to a number of intriguing features of fracture of heterogeneous materials ranging from universality and scale-invariance of the crack morphology or roughness [30–34], to power-law percolation behavior due to disorder in heterogeneous materials [35–38], and dynamical order parameters associated with crack front propagation [39–42].

4.2 Effective fracture resistance

Herein we approach fracture of heterogeneous materials through a combination of both schools of thought. On the one side, we preserve the classical equilibrium-based Griffith-type fracture approach in the form of an energy release criterion of bond fracture. On the other, we follow the statistical physics approach by considering the overriding strength of bond-energy fluctuations in the very definition of Griffith's energy release rate and fracture energy dissipation. We apply this synergistic approach to a suite of 2-D and 3-D multiphase sample materials which range from textured to random heterogeneous model materials (Fig. 4-1). We show that the combination of the two schools of thought within the framework of fluctuation-based fracture

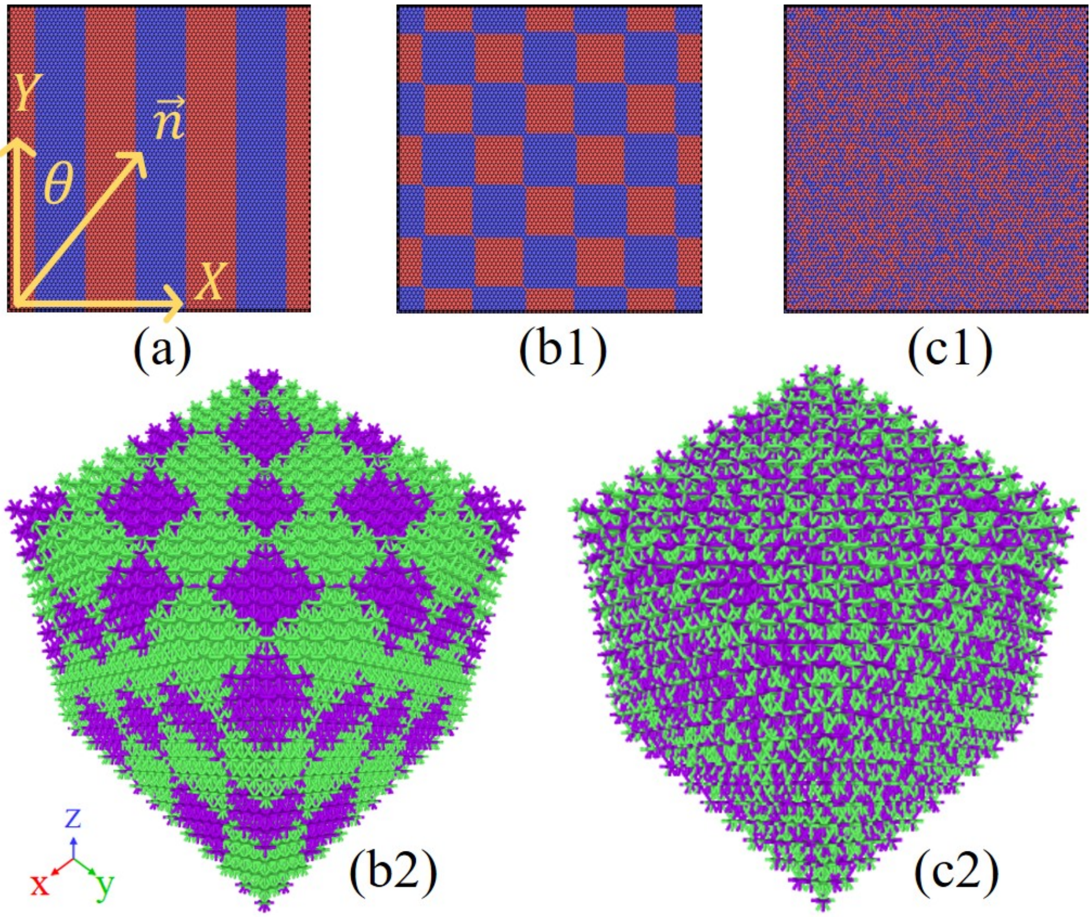

Figure 4-1: Geometrically ordered and disordered two-phase materials: (a) layered material with inclined uniaxial stretch direction; (b1-b2) 2-D and 3-D checkerboard; (c1-c2) 2-D and 3-D random material (visualized at $f_\beta = 50\%$).

mechanics [125] lends itself readily for derivation of effective fracture toughness of heterogeneous materials, including rigorous upper and lower bounds and percolation thresholds.

Our starting point is a dual definition of fracture in a multiphase material probed in the semigrand canonical ensemble ($\Delta\mu VT$). Each phase is defined by a fixed number of mass points, and interactions in between mass points are determined by groundstate energies, $\mathbf{E^0} = (\epsilon_A^0, \epsilon_B^0, ..., \epsilon_n^0)$, and elastic energies, $\mathbf{E}^\lambda = (\epsilon_A^\lambda, \epsilon_B^\lambda, ..., \epsilon_n^\lambda)$, such that the bond energy is $u_J = -\epsilon_J^0 + \epsilon_J^\lambda \overline{u}_J^{ij}$ for phases $J = A, B, ..., n$, with $\overline{u}_J^{ij}(r_{ij})$ a dimensionless expression of the two-point stretch potential in function of the bond distance r_{ij} (for potentials defined in §2.4). Admitting that cracks initiate and propagate in consequence of a concerted breaking of bonds, we probe all bonds in the system in the $\Delta\mu VT$-ensemble by sampling from an ensemble of equilibrated states at fixed bond rupture potential, $\Delta\mu$, volume, $V = V_0(1+\lambda)$, and temperature, T, with V_0 the initial volume and λ a dilation factor. Introduced for homogeneous materials [125], the bond rupture potential, $\Delta\mu$, is an auxiliary field which — akin to a radiation source — can switch bonds on or off, but does not directly affect mass points. In the $\Delta\mu VT$-ensemble, we evaluate Griffith's energy release criterion for bond fracture from fluctuations of the bond energy $U = \sum_{i=1}^N u_J^i$ of unbroken bonds $N = N_0 - M$ (with N, M, and N_0 the number of intact, broken, and total bonds, respectively) by means of the heat of bond rupture at the fracture phase transition [125]:

$$\frac{\mathrm{Cov}(U^\lambda, N)}{\mathrm{Cov}(N, N)} = -q_{br}^\lambda \equiv q_{br}^0 = -\frac{\mathrm{Cov}(U^0, N)}{\mathrm{Cov}(N, N)} \tag{4.1}$$

where $-q_{br}^\lambda$ stands for the bond energy release rate due to bond stretching U^λ. In accordance with Griffith's fracture theory, this strain energy release rate equals the heat of bond rupture q_{br}^0: it is the energy dissipated into heat by bond fracture of groundstate energy, $U^0 = -\mathbf{E^0} \cdot \mathbf{N}$, associated with bond numbers $\mathbf{N} = (N_A, N_B, ..., N_n)^T$:

$$q_{br}^0 = \mathbf{E^0} \cdot \frac{\mathrm{Cov}(\mathbf{N}, \mathbf{N})}{\mathrm{Cov}(N, N)} \cdot \mathbf{1}_{n,1} = \mathbf{E^0} \cdot \mathbf{S} \tag{4.2}$$

with $\mathbf{1}_{n,1}$ the vector of ones. In terms of Griffith's coining, q_{br}^0 can be viewed as the bond fracture energy of the n-phase heterogeneous material, defined by the $(n \times n)$ covariance matrix, $\mathrm{Cov}(\mathbf{N},\mathbf{N})$ of bond numbers of the phases, normalized by the variance of the total bond number, $\mathrm{Cov}(N,N) = \sigma_N^2$, which defines the overall bond compressibility [107]. In return, enabled by the semigrand canonical sampling, the bond fraction of each phase participating in the fracture process, $\mathbf{S} = (S_\alpha, S_\beta, ...S_n)^T$, permits a dual definition from both fluctuation and probability theory:

$$0 \leq S_\beta = \sum_{i=1}^{n} \frac{\mathrm{Cov}(N_i, N_B)}{\mathrm{Cov}(N,N)} \equiv \sum_{i=1}^{n} P(\beta \cap f_i) \leq 1 \tag{4.3}$$

for all $S_i \in \mathcal{S} = \{S_i \mid \sum_{(n)} S_i = 1\} \subseteq \mathcal{F} = \{f_i \mid \sum_{(n)} f_i = 1\}$. Herein, $\beta = M^B/\langle M\rangle$ stands for the random vector of bonds in phase B breaking at a probability

$$S_\beta = P(\beta) \tag{4.4}$$

According to the axiom of total probabilities, this probability, $P(\beta) = \mathrm{E}[\beta]$, is the sum of the joint probabilities $P(\beta \cap f_i) = P(f_i)P(\beta \mid f_i)$, with $f_i = P(f_i) \sim N_{i,0}/N_0$ the volume fraction of each phase, and $P(\beta \mid f_i)$ the conditional probability. The synergy of the dual definition (4.3) is recognized in the determination of bounds of the "effective" fracture resistance (4.2). In fact, among all uncorrelated (i.e., $\mathrm{Cov}(N_{i\neq B}, N_B) = 0$) *and* independent (i.e., $P(\beta \cap f_{i \neq B}) = 0$) fracture events in the n-phases, for which $S_\beta^{\lim} = (\sigma_{N_B}/\sigma_N)^2 \equiv P(\beta \cap f_\beta)$ defines the bond fractions $S_i \in \mathcal{S}$ in the eigenvector base of the bond convariance matrix, the lower and upper bounds are defined by the min-max values of the conditional probability, $0 \leq P(\beta \mid f_\beta) \leq 1$; that is:

$$\inf_{S_i \in \mathcal{S}, \mathbf{S}\cdot\mathbf{S}=1} (\mathbf{E^0} \cdot \mathbf{S}) \leq q_{br}^0 \leq \sup_{S_i \in \mathcal{S}, \mathbf{S}\cdot\mathbf{f}=\|\mathbf{S}\|^2} (\mathbf{E^0} \cdot \mathbf{S}) \tag{4.5}$$

where $\mathbf{f} = (f_\alpha, f_\beta, ..., f_n)^T$ is the vector of volume fractions of the phases. These bounds include the case of equiprobable fracture events in n-phases, for which $P(\beta \mid f_\beta) = 1/n$, and which entails the arithmetic mean as the effective fracture resistance, $q_{br}^{0,\mathrm{Hill}} = \mathbf{E^0} \cdot \mathbf{f}/n$, reminiscent of the Hill bound.

We proceed by exploring bond fracture correlations and dependence for limit cases of geometrically ordered and disordered two-phase materials [Fig. 4-1], for which $q_{br}^{0} = \epsilon_{A}^{0} + (\epsilon_{B}^{0} - \epsilon_{A}^{0})S_{\beta}$ for $S_{\alpha} = 1 - S_{\beta}$. More specifically, we carry out bond fracture simulations in the semigrand canonical ensemble, using a Monte Carlo technique (SGCMC) recently proposed for bond fracture simulations and related phase change phenomena in the brittle fracture of homogeneous materials [125]. On 2-D triangular and 3-D face-centered cubic (fcc) lattices, we perform SGCMC bond-swapping trial moves and canonical displacement moves that are supplanted with molecular dynamics (MD) time integration in the NVT-ensemble. A Nosé-Hoover thermostat is employed to maintain an average temperature of $T^{*} = k_{B}T/\epsilon_{0} = 0.1$ in reduced Lennard-Jones (LJ) units. The timestep for the MD runs is set to 0.005τ in LJ reduced units (with unit LJ parameters) (for simulation details, see §2.4). From converged Monte-Carlo simulations, we extract the random variables, N_{A}, N_{B}. We determine bond number fluctuations of the two phases, $\sigma_{N_A}^{2}$ and $\sigma_{N_B}^{2}$, and the total bond number fluctuation, $\sigma_{N}^{2} = \sigma_{N_A}^{2} + \sigma_{N_B}^{2} + 2\text{Cov}(N_{A}, N_{B})$, and obtain from Eq. (4.3) the participating bond fraction, S_{β}.

4.3 Upper and lower bounds

We begin with the predicted upper and lower bounds of fracture resistance from probability considerations of the participant volume fraction, S_{β} shown in Fig. 4-2. The upper bound for fracture resistance is manifested by loading in the y-direction of the layered composite, i.e. loading parallel to the fiber orientation where $\theta = 0$. Conversely, the lower bound occurs when the loading is perpendicular to the orientation of the composite geometry, loading in the x-direction of the layered composite. Furthermore, superposition of these two loading cases results in a Hill bound for the fracture resistance in the biaxial tension case shown in Fig. 4-2b. In terms of probability, the superposition comes from adding and normalizing the upper and lower bounds $\left(\frac{S_{\beta}}{f_{\beta}} = 0.5 = \frac{1}{n}\right)$. As predicted from Eq. (4.5) the lower bound yields a weakest-link model, where only the weaker phase, phase α, is involved in fracture. On the other

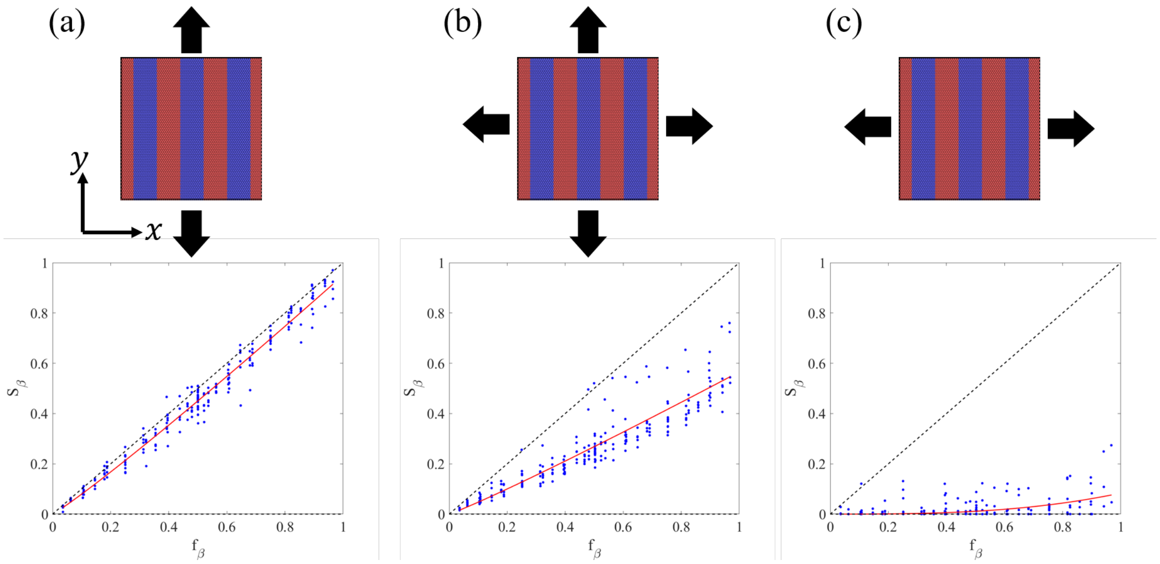

Figure 4-2: Fracture analogs of the Voigt-Hill-Reuss stiffness bounds. Loading (a) parallel to the composite orientation yields an upper (Voigt) bound for fracture resistance; (c) perpendicular to the geometry orientation results in a lower (Reuss-like) bound; (b) and superposition of the two bounds reproduces the Hill bound for fracture resistance. Simulation data for all different loading schemes, pertinent to the bound, are shown as blue dots. Fits of the data shown as red lines. Guides for the upper and lower bounds are shown as dashed lines.

hand, the upper bound describes an equal distribution of broken bonds based on the volume fractions of each phase in agreement with Eq. (4.5).

The bounds defined so far stem from the inherent bounds on a probability, namely any probability is a nonnegative number less than 1. The spectrum of probabilities between these bounds describes all other fracture configurations (geometry and loading pairs) of any two-phase composite in two dimensions and even higher dimensions since probabilities are always between 0 and 1.

4.3.1 Percolation parameters for the analytically derived upper and lower bounds

The functional forms of the participant volume fractions for the lower and upper bounds are analytically derived in Eq. (4.5) as $S_\beta^{\text{lower}} = 0$ and $S_\beta^{\text{upper}} = f_\beta$. Owing to this derivation and from results shown in Fig. 4-2, we recognize the participant volume fraction of the tough phase as a percolation order parameter. As such, the most general functional form for the S_β can be written in the form of a percolation strength as

$$S_\beta = a|f_\beta - p_c|^\gamma \tag{4.6}$$

where a and γ are fitting parameters and p_c, the critical percolation threshold in terms of volume fraction of the tougher phase in a two-phase material.

The percolation threshold, p_c, describes the onset of fracture in the tougher β phase, so the lower the percolation threshold, the sooner the tougher phase participates in the fracture and the higher the fracture resistance of the composite. Therefore, the percolation threshold is $p_c = 0$ and $p_c = 1$ for the upper and lower bounds of fracture resistance for any given composite geometry, respectively. In the case of the lower bound, a weakest link model is recovered and the crack only traverses through the weaker α phase as shown in Fig. 4-3(a,c). At the upper bound, the tougher β phase breaks with the weaker α phase such that the volume fractions of broken bonds are equal to the volume fractions of the intact bonds, $f_\beta = \frac{N_\beta}{N} = \frac{M_\beta}{M}$, as shown in Fig. 4-3(b,d).

This analysis is extended to the exponent, γ, from Eq. (4.6), for the upper and lower bounds. For the upper bound $p_c = 0$ and $a = \gamma = 1$, giving a participant volume fraction that is $S_\beta = (f_\beta - 0)^1$. In the case of the lower bound, $p_c = 1$, and so the only way to recover the lower bound solution would be through a γ that tends to infinity, resulting in $S_\beta = f_\beta^\infty \to 0$, for $0 < f_\beta < 1$.

The upper and lower bounds also serve as prototypical models of the sense of percolation in the fracture of two-phase composites in the semigrand canonical ensemble, as shown in Fig. 4-3(a, b), respectively. Percolation, here, is defined in terms of the participation of the α and β phases in the fracture process. In other words, percolation only happens when both S_α and S_β are greater than zero, and in the case of n-phase composites, if $S_i > 0$ for $i = 1, \ldots, n$. The α phase is defined as the phase that breaks first, so when loading a composite to failure, S_α will always be greater than zero. The important parameter, then, becomes S_β. In the case of a lower bound configuration, e.g. layered system loaded perpendicular to the layer orientation, only the α bonds break and no percolation occurs, as shown in Fig. 4-3(c). Percolation only happens when $S_\beta > 0$, when the percolation threshold is passed, and the meaning of this is shown in Fig. 4-3(d), where the bonds of all phases break. Effectively, the complicated interactions of volume fraction, geometry, energy parameters, and loading conditions can be reduced to a two-cell percolation problem as shown in the insets in Fig. 4-3(c, d), where the probabilities of each cell being filled in are the participant volume fractions. However, since S_α is always greater than 0, the percolation order parameter is S_β.

4.4 Random geometry

The second case we consider is a two-phase material with randomly assigned binary groundstate and elastic bond energies, $(\epsilon_A^0, \epsilon_A^\lambda)$ or $(\epsilon_B^0, \epsilon_B^\lambda)$ [Fig. 4-1(b)], which is most likely the simplest, i.e. analytically tractable, system among random lattice models [27, 123, 124], exhibiting probabilistic dependency. In fact, SGCMC simulations show that the bond fraction scales as:

$$S_\beta \sim f_\beta^\gamma \tag{4.7}$$

with an exponent $\gamma > 1$, mediated only by the elasticity mismatch between the two phases, $\kappa_\lambda = \epsilon_B^\lambda / \epsilon_A^\lambda$ [Fig. 4-4(a)]. Akin to weighted coin flipping, the conditional probability at high values of κ_λ can be estimated to be $P(\beta \mid f_\beta) = f_\beta$, for which reason $S_\beta = P(\beta \mid f_\beta) P(f_\beta) = f_\beta^2$. As a consequence, bond fracture events in the two phases are (close to) uncorrelated (i.e., $\mathrm{Cov}(N_A, N_B) \approx 0$) *and* independent (i.e., $P(\alpha \cap f_\beta) = P(\beta \cap f_\alpha) = 0$) independent of the stretch direction [Figs. 4-4(a,c)]. But when the elastic mismatch is inversed (from stiff-tough to soft-tough), an increasing probabilistic dependence between fracture events in the two phases readily explains an apparent elastic toughening, which will be explored in greater depth for the case of 3-D random geometries in the next chapter. In fact, at small values of κ_λ we recover the binomial distribution, $P(\alpha \cap f_\beta) = P(\beta \cap f_\alpha) = f_\beta(1 - f_\beta)$, for which Eqn. (4.3) and (4.5) predict $S_\beta = P(\beta \cap f_\alpha) + P(\beta \cap f_\beta) = f_\beta$, and which coincides with the

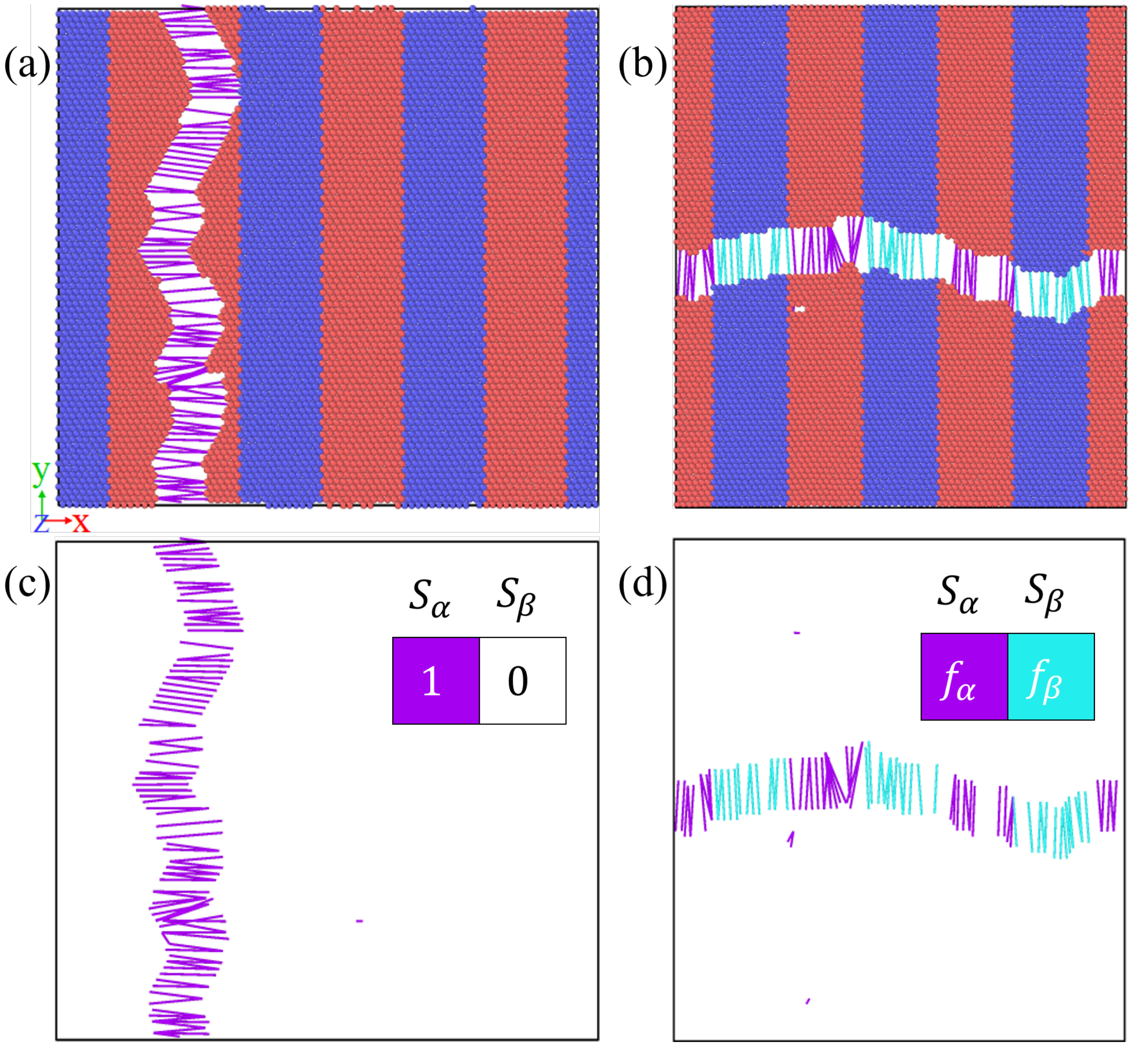

Figure 4-3: Sense of percolation in two dimensions. The AB composite is shown to demonstrate the sense of percolation using configurations for (a) lower: layered system stretched in the x-direction and (b) upper: layered system stretched in the y-direction bounds of effective fracture resistance. (c) In the case of the lower bound only the purple A bonds break. (d) For the upper bound bonds of all phases break (purple, A and teal, B) such that the volume fractions of broken and intact bonds of the same phase are equal, $S_\alpha = f_\alpha$ and $S_\beta = f_\beta$.

upper bound [Figs. 4-4(a-b)]. – That is, an elastic toughening mechanism in random binary systems mediated by elastic mismatch, κ_λ [inlet Fig. 4-4(a)].

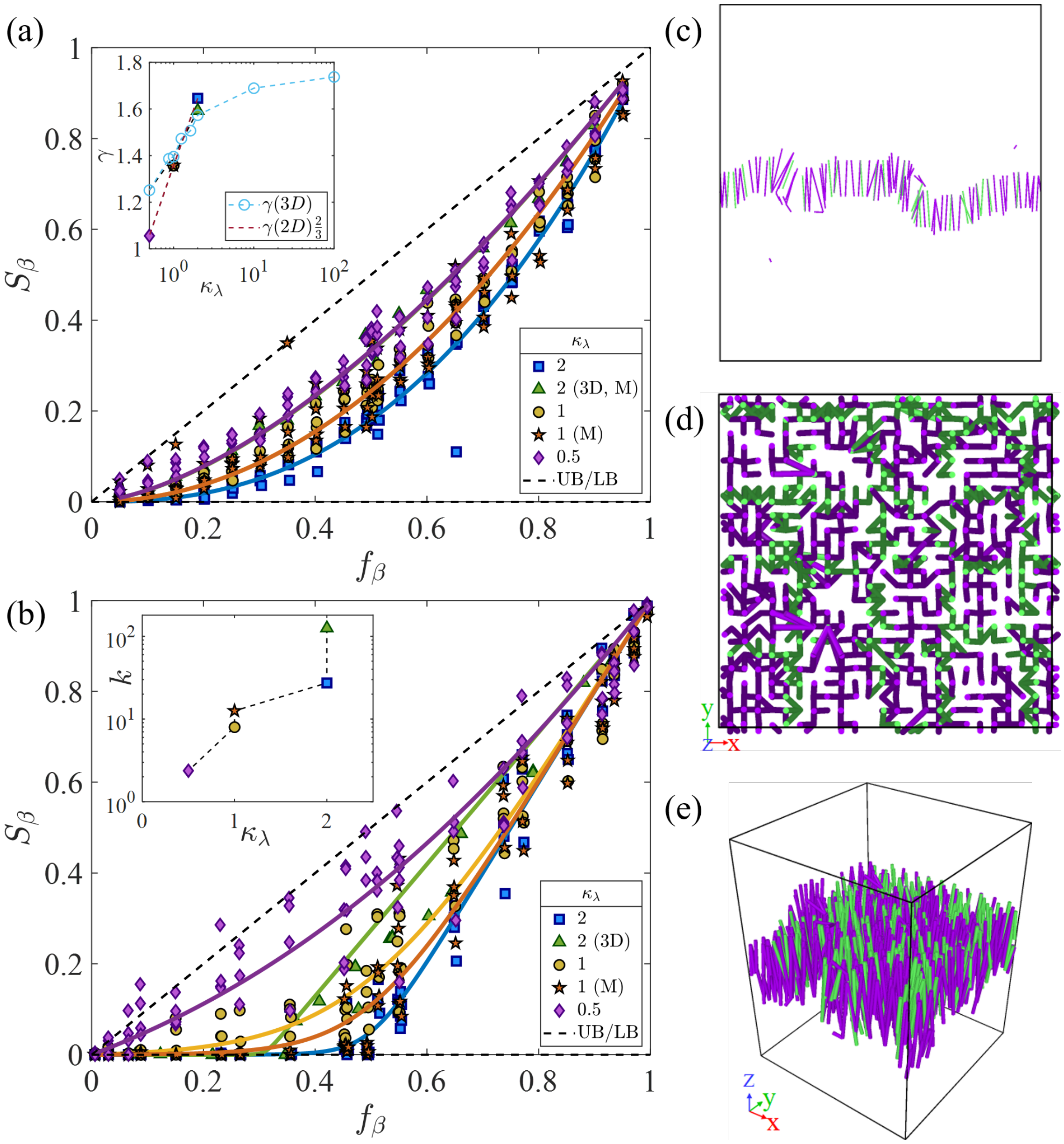

Figure 4-4: Elastic Toughening in fracture of two-phase (a,c) random and (b,d,e) textured material under uniaxial stretching in semigrand canonical ensemble: (a-b) bond fraction, $S_\beta(f_\beta) \sim f_\beta^\gamma$, contributing to "effective" bond fracture energy, $q_{br}^0 = \epsilon_A^0 + (\epsilon_B^0 - \epsilon_A^0)S_\beta$. Inset (a): exponent γ vs. elastic energy mismatch $\kappa_\lambda = \epsilon_B^\lambda/\epsilon_A^\lambda$. Inset (b): percolation correlation factor k vs. κ_λ. [SGCMC results obtained with harmonic and Morse potential (M) of groundstate energy ratio $\kappa_0 = \epsilon_B^0/\epsilon_A^0 = 2$.

4.5 Checkerboard geometry

Moreover, this soft-tough paradigm is not restricted to random materials; but manifests itself for highly textured materials as well. For illustration, consider the prototype of a two-phase textured material: a 2-D checkerboard [Fig. 4-1(c)] and a 3-D "checkercube", constructed in a simple cubic (sc) fashion by adjacent cubes of different groundstate and elastic bond energy [Fig. 4-1(d)]. In contrast to layered and random materials, textured materials may exhibit a percolation threshold ($p_C > 0$) for the activation of the reinforcing phase. From site percolation theory, the percolation threshold p_c is the critical probability of phase B to be part of an infinite "cluster". Indeed, for high elasticity contrast ($\kappa_\lambda > 1$), we observe in SGCMC-simulations that the participating bond fraction, S_β vs. f_β [Fig. 4-4(b)], exhibits the site percolation threshold of the considered textured material, i.e., the square-lattice percolation threshold $p_c = 1/2$ for the 2-D checkerboard, and the simple cubic percolation threshold $p_c = 0.31$ for the "checkercube". From a probabilistic point of view, percolation can be captured by a step-function conditional probability $P(\beta \mid f_\beta) = H(f_\beta - p_c)$, to obtain from Eq. (4.3) the participating bond fraction, $S_\beta = \int_{(f_\beta)} P\left(\beta \mid f_\beta\right) \mathrm{d}P = |f_\beta - p_c|/(1 - p_c)$. On the other hand, when the elastic energy contrast between the two phases is reduced ($\kappa_\lambda \leq 1$), we observe a change from critical to subcritical percolation behavior. To capture this transition, we introduce a smoothed step function, $P(\beta \mid f_\beta) = \left[1 + \exp(-k(f_\beta - p_c)\right]^{-1}$, where the regularization factor k permits transitioning from the step function ($k \to \infty$) to a smooth transition, in terms of the conditional and the joint probabilities:

$$P(\beta \mid f_\beta) = H^*(f_\beta - pc) \tag{4.8}$$

$$P(\beta \cap f_\beta) = \frac{\int_0^{f_\beta} H^*\left(f_\beta - p_c\right) \mathrm{d}f_\beta}{\int_0^1 H^*(f_\beta - p_c)\mathrm{d}f_\beta} \tag{4.9}$$

That is,

$$S_\beta(f_\beta) = \frac{\ln(1 + e^{-k(f_\beta - p_c)}) - \ln(1 + e^{kp_c}) + kf_\beta}{\ln(1 + e^{-k(1-p_c)}) - \ln(1 + e^{kp_c}) + k} \tag{4.10}$$

Using Eq. (4.10) to fit the simulation results, we obtain k in function of the elastic mismatch ratio, inset of Fig. 3(b), showing that the regularization factor k diverges for large values of κ_λ, which mimics the a correlation diverging at continuous phase transition. The fits shown in Fig. 4-4(b) confirm that the elastic toughening mechanism in textured materials results from a transition from a hard step-function percolation probability at high κ_λ-values where $k >> 1$, to a subcritical percolation at low κ_λ-values, where $k = O(1)$ [inset Fig. 4-4(b)]; whilst S_β approaches the upper bound [Fig. 4-4(b)].

4.6 Conclusion

In summary, enabled by the unique access to bond-energy fluctuations, we have shown that SGCMC simulations provide a means to rationalize the complexity of fracture of heterogeneous materials, from random to highly textured materials, encompassing percolation and statistical theories of fracture within a unified framework of fluctuation-based fracture mechanics. True to the fluctuation-dissipation theorem [126], bond-energy fluctuations permit identifying theoretical upper and lower bounds of fracture resistance, which are critical to ascertain toughening mechanism in composite materials, such as the soft-tough paradigm which results from elastic mismatch between phases. At low elastic contrast, toughening can result from a variety of intriguing features which to the best of our knowledge have been overlooked so far. This includes softening of probabilistic dependence of bond fracture processes in random binary systems to softening of sharp site percolation thresholds in textured materials. While counter-intuitive on first sight, the soft-tough paradigm can be connected to a number of experimental observations, ranging from toughening of brittle solids by highly deformable polymers or organics, such as gas shale (brittle clay minerals reinforced by soft kerogen) [127], nacre (brittle bricks of aragonite glued together by thin biofilms at interfaces) [128], to stress-induced transformational toughening mechanisms in ceramics [129, 130], and toughening of sparse elastic networks relevant for e.g. hydrogels [131], to name a few. For such specific applications, the highly idealized model composites considered in this Chapter need to be refined to account for realistic texture. Another important step beyond this work is the consideration of three- and four-point interactions required for the application of the SGCMC methodology to molecular-scale structures and molecular-inspired structural mechanics.

Chapter 5

Fracture of random and checkerboard geometries in three dimensions

Dimensionality remains another modular aspect of the semigrand canonical approach to fracture mechanics as demonstrated by the three- and two-dimensional work for homogeneous (see Ch. 3) and heterogeneous (see Ch. 4) materials, respectively. We start by reexamining the meaning of percolation, this time in three dimensions, similar to the what is demonstrated in Fig. 4-3 for two dimensions. In three dimensions the crack occurs in a plane, providing a larger dataset to perform useful analysis such as measuring the two-point correlation function, which is shown to measure S_β directly from fracture surfaces, providing a path for experimental measurement of the participant volume fraction [132]. This, in turn, warrants closer examination of the link between the participant volume fraction and the two-point correlation function. The soft-tough paradigm is also examined in the third dimension, confirming quantitatively the results from the previous chapter for two-phase materials. Specifically, a wide range of elasticity mismatch ratios for three-dimensional random and checkerboard geometries are probed through SGCMC simulation and related to the specific functional parameters Eqn. (4.7) and (4.10), revealing the microstructure-specific mechanisms of the soft-tough paradigm and corroborating the choice of functional forms.

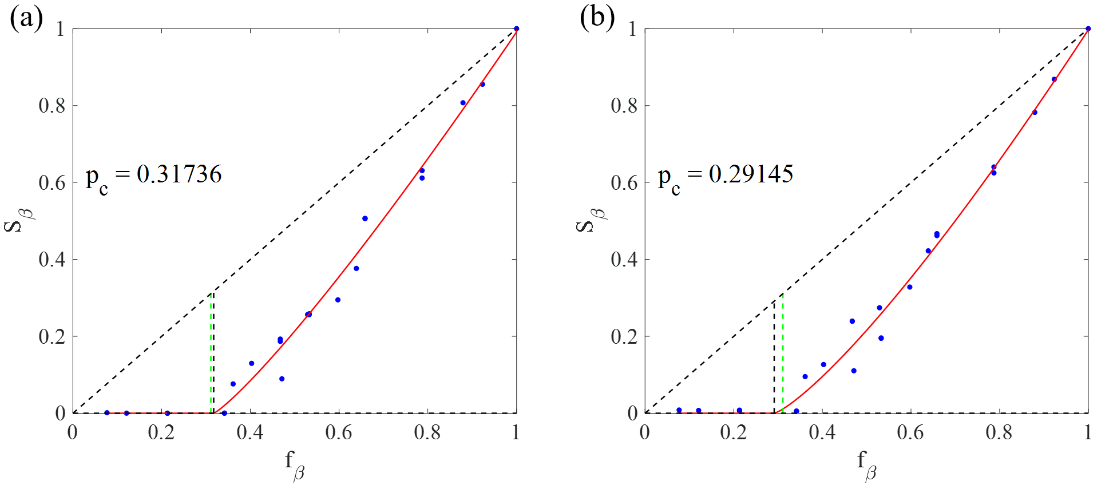

Figure 5-1: Participant volume fractions in three dimensions for the checkerboard composite. Simulation data (blue dots) and fits to obtain percolation thresholds (red lines) for the checkerboard geometry for the (a) uniaxial and (b) triaxial loading cases. Guides for the upper and lower bounds are shown as dashed lines. The vertical black dashed line indicates the location of p_c from fitting.

5.1 Percolation in three dimensions

After constructing the geometries in the FCC lattice, semigrand canonical Monte Carlo simulations are executed to measure the S_β curves for the checkerboard and random geometries. Results of the simulations are depicted in Fig. 5-1. As expected for the checkerboard geometry the percolation threshold, for the uniaxial and triaxial displacement-controlled tension tests are lower in three dimensions than they are in two dimensions. This is readily understood from the analogy with the lower stress intensity factors for the “penny-shaped” crack compared to the edge and central Griffith cracks. The extra dimension manifests into a crack plane resulting in earlier participation of the tougher β phase in the cracking. In the case of the z-axis uniaxial loading, the crack now has two axes it can grow along, namely the $x - y$ plane, as shown Fig. 5-2(c,d). This results in a lower percolation threshold in three dimensions ($p_c^{3D} = 0.31736$) compared to the two-dimensional case ($p_c^{2D} = 0.47641$, see Ch. 4), as shown in Fig. 5-1(a). Percolation thresholds in the checkerboard pattern are lower because the extra dimension provides more paths for the crack to be able to grow along in a plane as opposed to in a line as shown in Fig. 5-2.

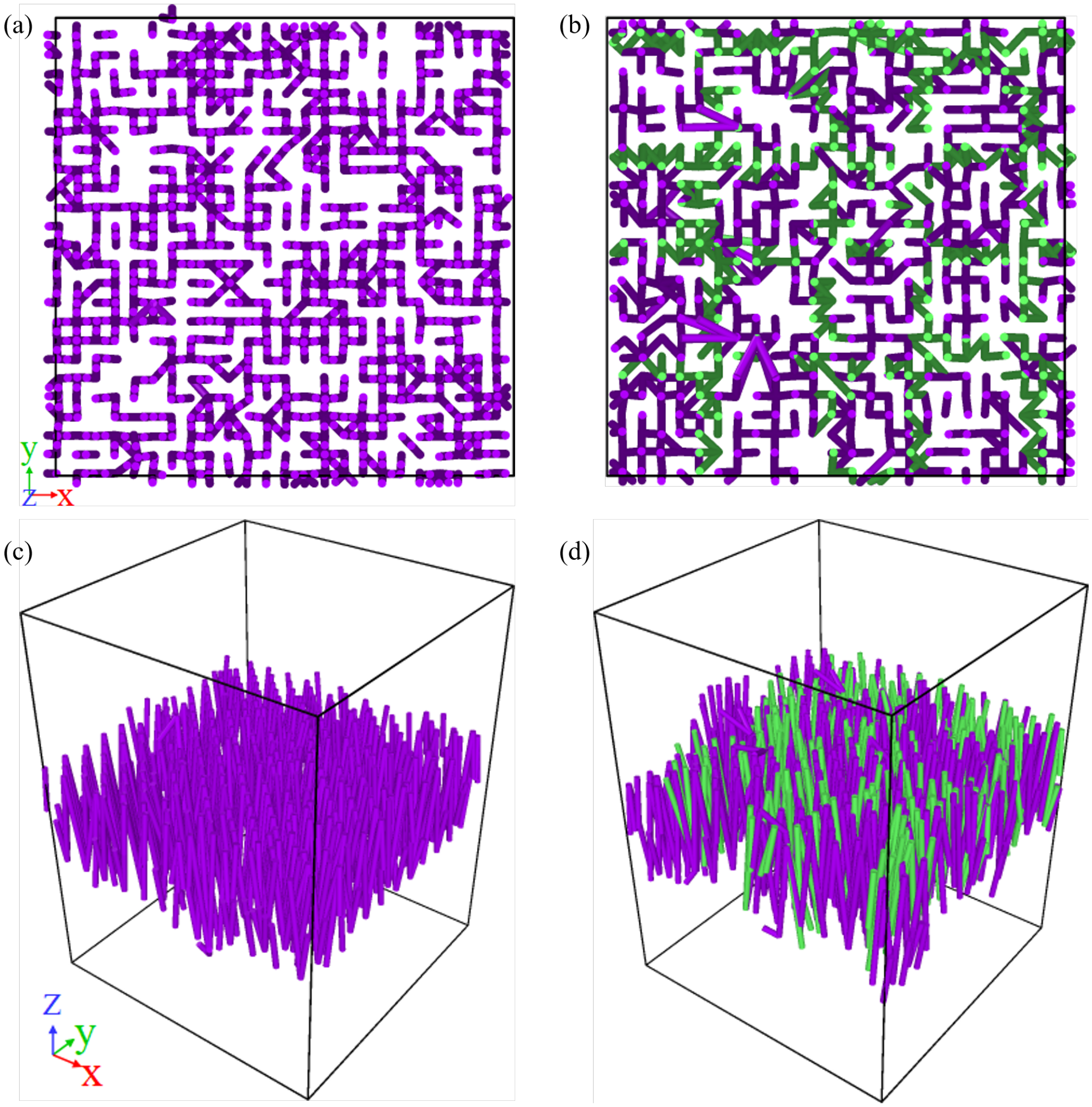

Figure 5-2: Percolation of broken phases in three dimensions: uniaxial z-loading case. Top views of the crack plane for the checkerboard geometry at (a) $f_\beta = 21.3\%$ where no percolation occurs and (b) $f_\beta = 61.3\%$ where bonds of all (both) phases break. Purple bonds are the $\alpha = A$ phase bonds, and green bonds are the $\beta = B$ phase bonds. (c, d) Perspective views of (a, b), respectively, showing the bonds breaking along a plane.

5.2 Equivalent measures of bond fraction S_β in the semigrand canonical ensemble

The determination of the bond fraction S_β from SGCMC simulations is based on the outcome of converged SGCMC simulations; that is a large number of – say C – realizations for which the probability of bond switching 'ON' [i.e. Eq. (3.2a)] is equal to the probability of bond switching 'OFF' [i.e. Eq. (3.2b)]. Restricting ourselves to two phase materials, we denote by N^j, N_A^j, N_B^j ($j = 1, \ldots, C$) the corresponding bond numbers of these realizations; respectively their broken complements, $N_{br}^j = N_0 - N^j, N_{A,br}^j = N_\alpha^j, N_{B,br}^j = N_\beta^j$.

The reference measure is the fluctuation-based definition (4.3). It can be viewed as a linear regression of (N_B^j, N_j):

$$\widehat{N_B}^j = \overline{N_B} + S_\beta(N^j - \overline{N}) \tag{5.1}$$

with

$$S_\beta = \frac{\partial \widehat{N_B}^j}{\partial(N^j - \overline{N})} = \frac{\mathrm{Cov}(N_B, N)}{\sigma_N^2} \tag{5.2}$$

where $\overline{N_B}$ and $\overline{N}$ are the means of N_B^j and N^j, respectively. By definition, the same holds for the broken bonds, when letting $\widehat{N_\beta}^j = N_{B,0} - \widehat{N_B}^j$:

$$\widehat{N_\beta}^j = \overline{N_\beta} + S_\beta(N_{br}^j - \overline{N_{br}}) \tag{5.3}$$

with:

$$S_\beta = \frac{\partial \widehat{N_\beta}^j}{\partial(N_{br}^j - \overline{N_{br}})} = \frac{\mathrm{Cov}(N_\beta, N_{br})}{\sigma_{N_{br}}^2} \tag{5.4}$$

Then, let $e^j = N_\beta^j - \widehat{N_\beta}^j$ be the residuals between the realization N_β^j and the linear regression $\widehat{N_\beta}^j$; of zero mean ($\overline{e} = 0$). Furthermore, let $N_\beta^j = S_\beta^j N_{br}^j$ and $\overline{N_\beta} = \overline{S_\beta^j N_{br}^j}$; and hence:

$$\widehat{N_\beta}^j = S_\beta N_{br}^j + \overline{(S_\beta^j - S_\beta) N_{br}^j}; \tag{5.5}$$

If we remind us of the dual definition (4.4), which implies $\overline{N_\beta} = S_\beta \overline{N_{br}}$, the second term in Eq. (5.5) is zero, while $e^j/N^j_{br} = S^j_\beta - S^\beta$. A single realization j out of an equilibrated semigrand canonical ensemble thus provides a first-order estimate of the bond fraction:

$$\forall j; \quad S^j_\beta = S_\beta + \frac{e^j}{N^j_{br}} \tag{5.6}$$

A cross-plot of $S^j_\beta = N^j_\beta/N^j_{br}$ vs. $S_\beta = \mathrm{Cov}(N_B, N)/\sigma^2_N$ allows one to ascertain relevance of the first-order approximation $S_\beta \approx S^j_\beta$.

5.3 Link with two-point correlation function of broken bonds

In this section, we determine S^j_β from the two-point correlation function of broken bonds of a realization j:

$$S^j_\beta = S^\beta_2(r=0) = \sqrt{S^\beta_2(r \to \infty)} \tag{5.7}$$

As a reminder, the two-point correlation function for a phase J is defined by [58,133]:

$$S^J_2(r = ||\vec{r}_2 - \vec{r}_1||) = \langle I^J(\vec{r}_1), I^J(\vec{r}_2)\rangle \tag{5.8}$$

where $I^J(\vec{r}_i)$ is the indicator function of phase J:

$$I^J(\vec{r}_i) = \begin{cases} 1 & \text{if} \quad i \in J \\ \\ 0 & \text{if} \quad i \notin J \end{cases} \tag{5.9}$$

A second important quantity provided by the two-point correlation function is the mean chord length, ℓ_c:

$$\left.\frac{\mathrm{d}S^J_2}{\mathrm{d}r}\right|_{r\to 0} = -\frac{S^J_2(0)}{\ell_c} \tag{5.10}$$

The mean chord length is close to a multiplying function equal to the specific surface [134]. Therefore, for a homogeneous material ($f_J = 1$), for which $S_2(r) = 1$, the slope is zero, and hence $\ell_c \to \infty$; and in the dilute limit of $f_J << 1$, the slope is infinite, and hence $\ell_c \to 0$. We keep these asymptotes in mind for the pursuing analysis.

5.4 Random binary system

In the case of a random binary system, SGCMC results provide:

$$S_\beta = f_B^\gamma \tag{5.11}$$

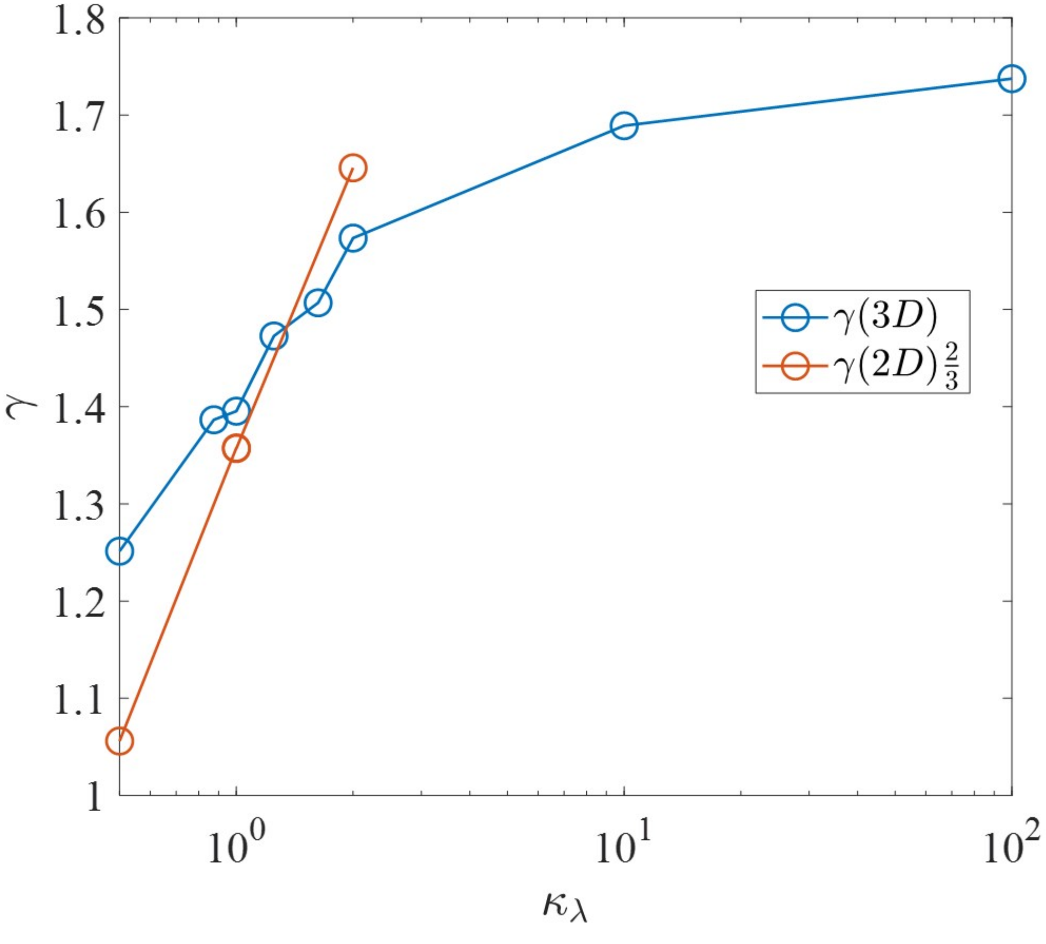

Figure 5-3: Fracture of random binary two-phase material under uniaxial stretching in semigrand canonical ensemble: Fitted exponent γ from SGCMC results, $S_\beta(f_B) = f_B^\gamma$. In order to compare 2-D with 3-D simulations, the exponent $\gamma(2D)$ obtained from 2-D simulations is re-scaled to account for different sampling volumes in the SGC-ensemble.

with an exponent γ which depends on (i) the elastic energy mismatch parameter, κ_λ, and (ii) the dimension $d = 2$ or $d = 3$, inset of Fig. 4-4(a). In order to compare results from 2-D and 3-D simulations, we note that 3-D simulations sample bond fracture in a volume, whereas 2-D simulations sample bond fracture on a surface. If we associate with the sampling a length scale $S_\beta \sim \mathcal{L}^d$, we correct, for the sole purpose of comparison, the exponent obtained from 2-D simulations by

$$S_\beta^{(d=3)} = \left(S_\beta^{(d=2)}\right)^{2/3} = f_B^{\frac{2}{3}\gamma} \tag{5.12}$$

This is shown in Fig. 5-3, from which we conclude that the exponent approaches the lower bound of γ, $\gamma = 1$, for low values of the elastic mismatch ratio, $\kappa_\lambda = \epsilon_B^\lambda / \epsilon_A^\lambda < 1$, and approaches asymptotically $\gamma = 2$ for high values of κ_λ. The question is why?

Our starting point is a probability estimate of bond fracture. Akin to weighted coin flipping, the conditional probability of a binary system is:

$$P(\beta \mid f_B) = f_B \tag{5.13}$$

Whence the joint and total probability according to Eq. (4.3):

$$S_\beta = P(\beta) = P(\beta \mid f_B) P(f_B) = f_B^2 \tag{5.14}$$

That is, $\gamma = 2$. This probability estimate ignores bond interactions. Insight into these interactions is provided by the two-point correlation function (5.8), applied to the broken bonds of the two phases [i.e., $J = \alpha, \beta$] for different volume fractions and elastic mismatch ratios. Typical examples of two-point correlation functions for the two phases $(S_2^\alpha(r), S_2^\beta(r))$, together with the cross correlation $(S_2^{(\alpha,\beta)})$, are shown in Fig. 5-4(a). Following Eq. (5.6), we verify that the value of $S_2^\beta(r)$ respects the asymptotes (5.7); that is,

$$\forall f_B; \quad S_2^\beta(r = 0) = S_\beta; \quad S_2^\beta(r \to \infty) = S_\beta^2 \tag{5.15}$$

This is shown in Fig. 5-4(b), where we plot $S_2^\beta(r=0)$ vs. $S_\beta = \mathrm{Cov}(N_B, N)/\sigma_N^2$ from Eq. (4.3).

A second important information provided by the two-point correlation function is the mean chord length of broken bonds, ℓ_c^β, which we obtain from Eq. (5.10) in a dimensionless form:

$$\left.\frac{\mathrm{d}S_2^\beta}{\mathrm{d}(r/r_c^B)}\right|_{r\to 0} = -\frac{S_2^\beta(0)}{(\ell_c^\beta/r_c^B)} \tag{5.16}$$

where r_c^B is the potential cut-off radius [see Eqn. (2.11)]:

$$r_c^B = r_0\left(1+\sqrt{2\frac{\epsilon_B^0}{\epsilon_B^\lambda}}\right) = r_0\left(1+\left(1-\frac{r_c^A}{r_0}\right)\sqrt{\frac{\kappa_0}{\kappa_\lambda}}\right) \tag{5.17}$$

Fig. 5-4(c) displays the normalized mean chord length ℓ_c^β/r_c^B in function of the volume fraction f_B. It is remarkable to note that the normalized mean chord length, ℓ_c/r_c^B collapses onto a single master curve for all f_B and all mismatch ratios κ_λ; that is:

$$\forall f_B, \forall \kappa_\lambda; \quad \frac{\ell_c^\beta}{r_c^B} = \mathcal{S}_0'(f_B) \tag{5.18}$$

where $\mathcal{S}_0'(f_\beta)$ [displayed in Fig. (5-4(c)] has asymptotes $\mathcal{S}_0'(f_\beta=0)=0$ and $\mathcal{S}_0'(f_\beta = 1)\to\infty$ [see Section 5.3]. Hence, for high values of $\kappa_\lambda = \epsilon_B^\lambda/\epsilon_A^\lambda$, the mean chord length of the fractured bonds is conditioned by short-term interactions defined by the bond length, $\ell_c^\beta \sim r_0$. In return, as the elastic mismatch is inversed, so that the tougher phase (B) is more compliant than the weaker phase (A), the mean chord length of fracture bonds increases, $\ell_c^\beta \sim r_0\kappa_\lambda^{(-1/2)}$, reminiscent of long-range, collective interactions. This suggests that the elastic toughening which we observe for the random system in form of exponent $\gamma = \gamma(\kappa_\lambda) \in [1,2]$ [see Eq. (5.11) and Fig. 5-3] is due to a shift from short-range interactions at high κ_λ-values to long-range interactions at low κ_λ-values.

5.5 Checkerboard geometry

The last case considered in our analysis is the 2-D checkerboard and 3-D checkercube. These textured model materials were chosen because of their known geometric site percolation at respectively $p_c = 0.5$ for the 2-D square-lattice and $p_c = 0.31$ for the 3-D simple cubic lattice. The site percolation thresholds are readily obtained from the mean chord length derived from the two-point correlation functions of the lattice bonds of the two phases of volume fraction $S_2^A(0) = f_A$ and $S_2^B(0) = f_B$:

$$\left.\frac{\mathrm{d}S_2^A}{\mathrm{d}r}\right|_{r\to 0} = -\frac{f_A}{\ell_c^A}; \quad \left.\frac{\mathrm{d}S_2^B}{\mathrm{d}r}\right|_{r\to 0} = -\frac{f_B}{\ell_c^B} \tag{5.19}$$

In fact, as shown in Fig. 5-5, the chord lengths for different volume fractions exhibit Dirac-delta -type behavior at the site percolation threshold p_c. The question we herein address is how this site percolation affects bond fracture of the textured system.

We recall from §4.5, we obtain an estimate of the probability of bond fracture for "hard" site percolation:

$$S_\beta = P(\beta) = P(\beta \cap f_\beta) = \frac{|f_\beta - p_c|}{1 - p_c} \tag{5.20}$$

A comparison with SGCMC results readily shows that site percolation dominates the composite response for large κ_λ values, but fails to capture the bond fraction at lower elastic mismatch values, $\kappa_\lambda < 1$, see Fig. 4-4(b). The question is why?

Proceeding as before, an insight is provided by the two-point correlation of the *broken* bonds of each phase [inset of Fig. 5-6(a)]. We verify that their respective values at $r = 0$ provides an estimate of the participating bond fraction, $S_2^\alpha(r = 0) = S_\alpha$ and $S_2^\beta(r = 0) = S_\beta$; according to Eq. (5.6) [Fig. 5-6(a)]. This allows us to inspect the mean chord length of the broken bonds for both phases from Eq. (5.10). The results are displayed in Fig. 5-6(b-c). The following observations deserve attention: (i) For high values of elastic mismatch, $\kappa_\lambda = \epsilon_B^\lambda/\epsilon_A^\lambda > 1$, the mean chord length of the weaker phase, ℓ_c^α (broken A bonds) diverges at the geometric site percolation threshold $f_\beta = p_c$, at which point the weaker phase (A) becomes part of a continuous (i.e., infinite) cluster of broken A bonds (α), as one expects from a site percolation phenomenon [Fig. 5-5(a)]. (*ii*) As the elastic mismatch is reduced and inversed ($\kappa_\lambda < 1$), the divergence disappears – a hallmark of a smooth phase transition. Otherwise said, a more compliant B phase de-activates bond fracture in phase A (α), in favor of bond fracture in phase B (β). (*iii*) The mean chord length of broken B bonds, ℓ_c^β, remains (almost) continuous, shifting from a constant value below the percolation threshold to a monotonically increasing value above, determined by texture. More specifically, below percolation, $f_B < p_c$, the mean chord length scales with the cut-off radius, $\ell_c^\beta \sim r_c^B$ [see Eq. (5.17)], until it reaches the mean chord length which characterizes the texture, defined by $\ell_c^\beta \sim f_B^2(1 - f_B)^{(1/d-1)}$ considering the specific surface, $s \sim f_B/\ell_c$, of the B-phase beyond percolation in the checkerboard ($d = 2$) or checker-cube ($d = 3$).

In summary, the comparative analysis of the mean chord length of intact and broken bonds shows that the elastic toughening of the considered textured materials is due to the smoothing of the hard percolation of the weaker phase (A) at the geometric percolation threshold of the tougher phase (B). To capture this transition in terms of the participating bond fraction, we consider a smooth approximation of the Heaviside function. Using Eq. (4.10) to fit the simulation results, we obtain k in function of the elastic mismatch ratio, inset of Fig. 34-4(b), showing that the regularization factor k diverges for large values of κ_λ, which mimics the mean chord length of the weaker phase.

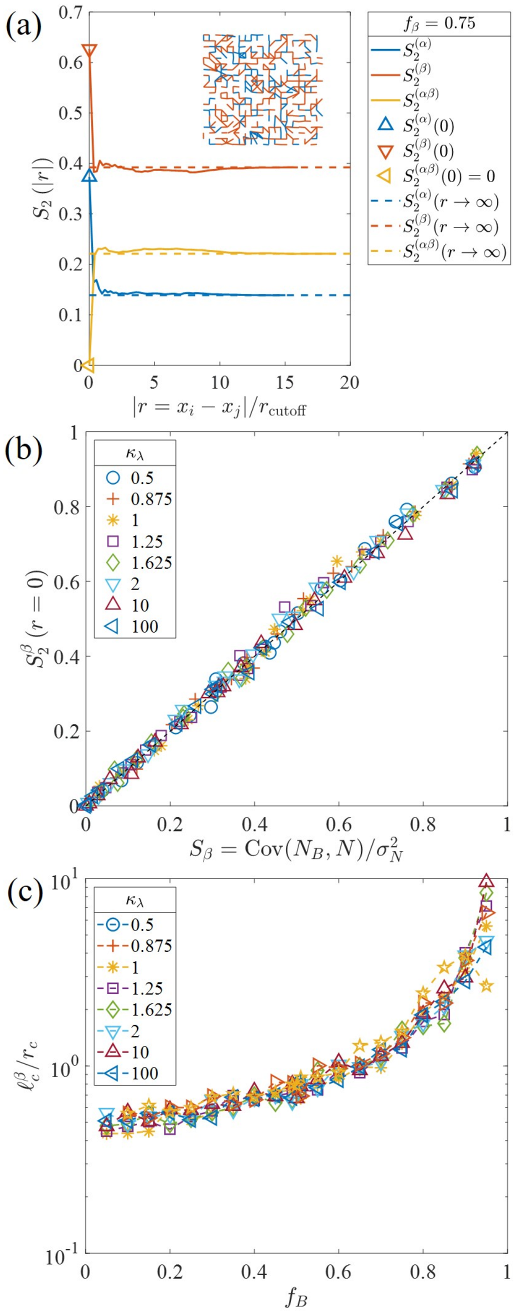

Figure 5-4: Two-Point Correlation Function, S_2^β, of broken bonds for random binary two-phase material: (a) example of two-point correlation function $S_2^\alpha(r)$, $S_2^\beta(r)$, $S_2^{(\alpha,\beta)}(r)$ for $f_B = 0.75$. Inset displays broken bonds of the two phases projected on fracture plane orthogonal to load direction. (b) Cross-plot of $S_2^\beta(r = 0)$ obtained from single realizations vs. S_β obtained from bond fluctuations of the (entire) equilibrated semigrand canonical ensemble at different elastic mismatch ratio, $\kappa_\lambda = \epsilon_B^\lambda / \epsilon_A^\lambda$. (c) Normalized mean chord length of broken bonds ℓ_c^β / r_c^B vs. volume fraction f_B ($r_c^B = r_{\text{cutoff}}$ is the potential cutoff radius).

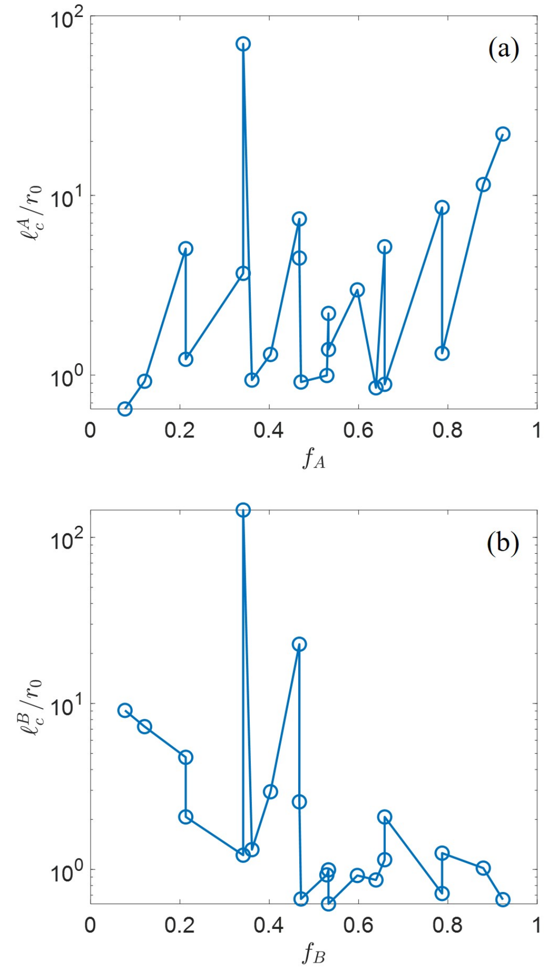

Figure 5-5: Mean chord length of 3-D checkercube vs. volume fraction for (a) phase A, ℓ_c^A/r_0 vs. f_A; and (b) phase B, ℓ_c^B/r_0 vs. f_B; obtained from the two-point correlation function, $S_2^J(r)$ $(J = A, B)$, of intact lattice bonds (r_0 is lattice distance).

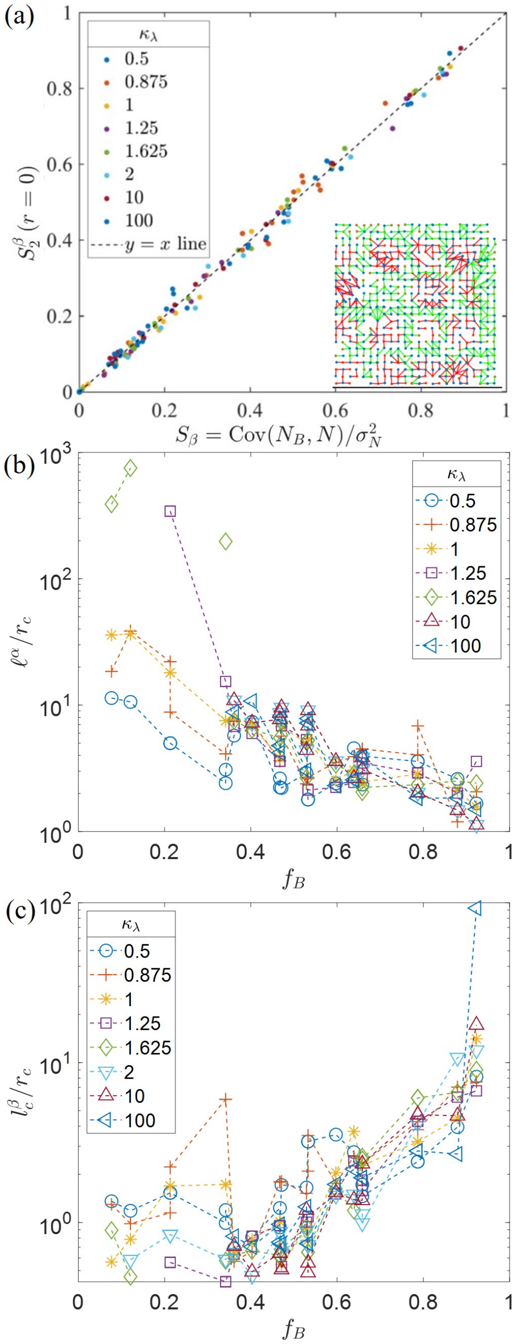

Figure 5-6: Two-point correlation function and mean chord length of broken bonds for two-phase checkercube composite: (a) Cross-plot of $S_2^\beta(r=0)$ obtained from single realizations vs. S_β obtained from bond fluctuations of the (entire) equilibrated semigrand canonical ensemble at different elastic mismatch ratio, $\kappa_\lambda = \epsilon_B^\lambda/\epsilon_A^\lambda$. Inset displays broken bonds of the two phases projected on fracture plane orthogonal to load direction for $f_B = 0.75$. (b-c) Normalized mean chord length of broken bonds: (b) ℓ_c^α/r_c^A and (c) ℓ_c^β/r_c^B vs. volume fraction f_B (r_c^A and r_c^B are potential cutoff radius of phase A and B).

Chapter 6

Loading orientation and interface effects

Upper and lower bounds can be understood intuitively for two-dimensional materials. Here, we more systematically probe the region between the prototypical upper and lower bounds in two dimensions by considering different intermediate loading orientations. Moving along a strain Mohr circle, the effect of loading orientation on a layered material is shown to delineate a state line separating cooperative and exclusive bonding interactions around the Hill bound. Separation of bonding interaction modes identifies critical volume fractions and loading orientation angles where loss of fracture resistance recovers the lower bound (weakest link model) for fracture. In addition to effect of loading orientation, we also examine the effect of the interface in a layered material subjected to uniaxial loading. Results of the interface study are in line with the soft-tough paradigm demonstrated in previous chapters, where the more compliant and tougher interface outperforms its stiffer counterparts leading to a more fracture resistant composite on the whole. Interfaces can be seamlessly incorporated into the semigrand canonical approach by treating each interface as an additional phase, where the n-phase extension of the governing equations is used.

6.1 Effect of loading orientation

Fracture resistance of a material can depend on loading orientation [57,135–137]. An immediate example following Ch. 4 is the orthogonal and parallel load application with respect to fiber orientation in the layered composite. Loading parallel to the fibers results in an upper bound in terms of fracture resistance, and loading orthogonally yields a weakest link model where the fracture process is constrained to the weaker phase (see Fig.4-2). Herein, we consider layered, random and checkerboard geometries, fixing the geometry axis, and sweeping across different loading orientations to examine the effect on fracture resistance.

6.1.1 Layered geometry

With a layered material, a geometry axis can be readily defined by the layer fiber orientation. The application of load further sets a second vector defining a loading axis. Then, the angle between these two axes, in two dimensions, defines an angle, θ, describing the loading orientation with respect to the fiber angle orientation. This angle becomes a loading parameter to define a set of displacement loading conditions that can be graphically represented by a strain Mohr circle, shown in Fig. 6-1. From the upper and lower bounds, the highest and lowest fracture resistance occur at $\theta = 0°$ and $90°$, respectively. We use the Mohr circle, to systematically map out the intermediate regions of fracture resistance for $0° \leq \theta \leq 90°$.

For $\theta > 0°$, the particpant volume fraction starts to deviate from the upper bound, $S_\beta = mf_\beta$, for $\frac{1}{2} \leq m < 1$. At $\theta \geq 45°$, the bond fraction follows the Hill bound up to $f_\beta = 1/2$, beyond which $S_\beta = 0$ [Figs. 6-2(a)]. More generally, we appeal to probability considerations to understand the effect of loading orientation on the fracture process for the layered system. Given f_β and θ, the conditional probability $P(\beta \mid f_\beta, \theta)$ of a bond in the β-phase to be activated by the load direction is:

$$P(\beta \mid f_\beta, \theta) = \vec{e_f} \cdot \vec{n} = \cos\theta \qquad (6.1)$$

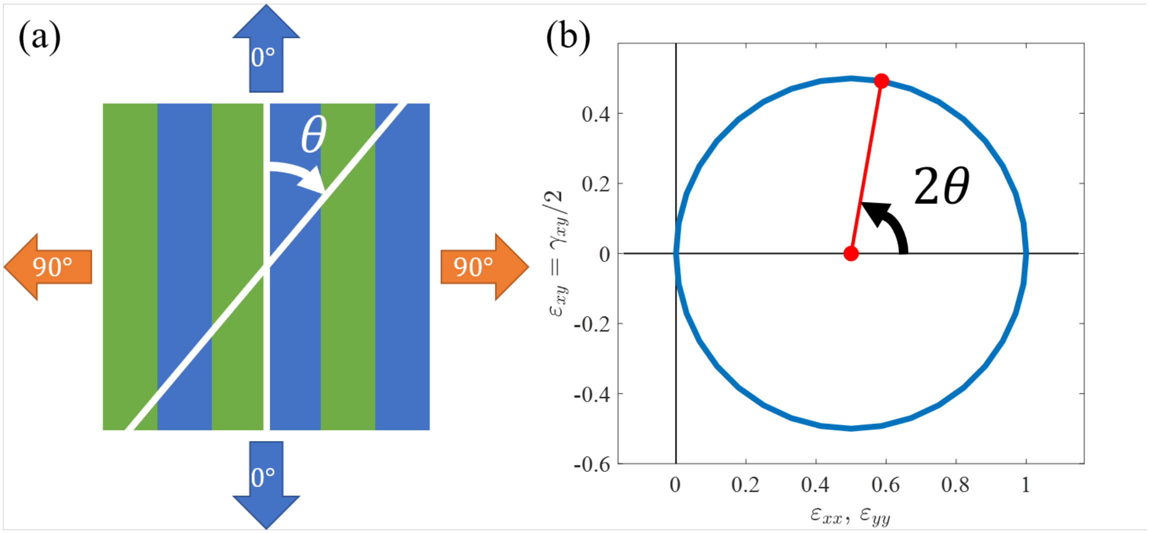

Figure 6-1: Schematic orientation study and strain Mohr circle

where $\vec{e}_f$ is the layer orientation, and $\vec{n}$ the stretch direction. In return, since the volume fraction, f_β, and the angle of load application, θ, are independent, the joint probability $P(f_\beta \cap \theta) = P(f_\beta)P(\theta) = f_\beta \cos\theta$. The joint probability of β and (f_β, θ) is obtained, when noting:

$$P(\beta \mid f_\beta, \theta) = \frac{\mathrm{d}P(\beta \cap f_\beta, \theta)}{\mathrm{d}P(f_\beta, \theta)} \tag{6.2}$$

and considering the Radon–Nikodym theorem, to give:

$$P(\beta \cap f_\beta, \theta) = \int_{(f_\beta,\theta)} P\left(\beta \mid f_\beta, \theta\right) \mathrm{d}P(f_\beta, \theta) \tag{6.3}$$

Denoting $\mathrm{d}P(f_\beta, \theta) = \mathrm{d}f_\beta \cos\theta - \mathrm{d}\theta f_\beta \sin\theta$, we obtain after integration:

$$P(\beta \cap f_\beta, \theta) = \frac{f_\beta}{2}(3\cos^2\theta - 1) \geq 0 \tag{6.4}$$

Finally, considering the fracture processes in the two phases as independent, $P\left(\beta \cap f_\alpha, \theta\right) = 0$, the participant bond fraction is obtained as:

$$S_\beta = P(\beta) = P(\beta \cap f_\beta, \theta) \geq 0 \tag{6.5}$$

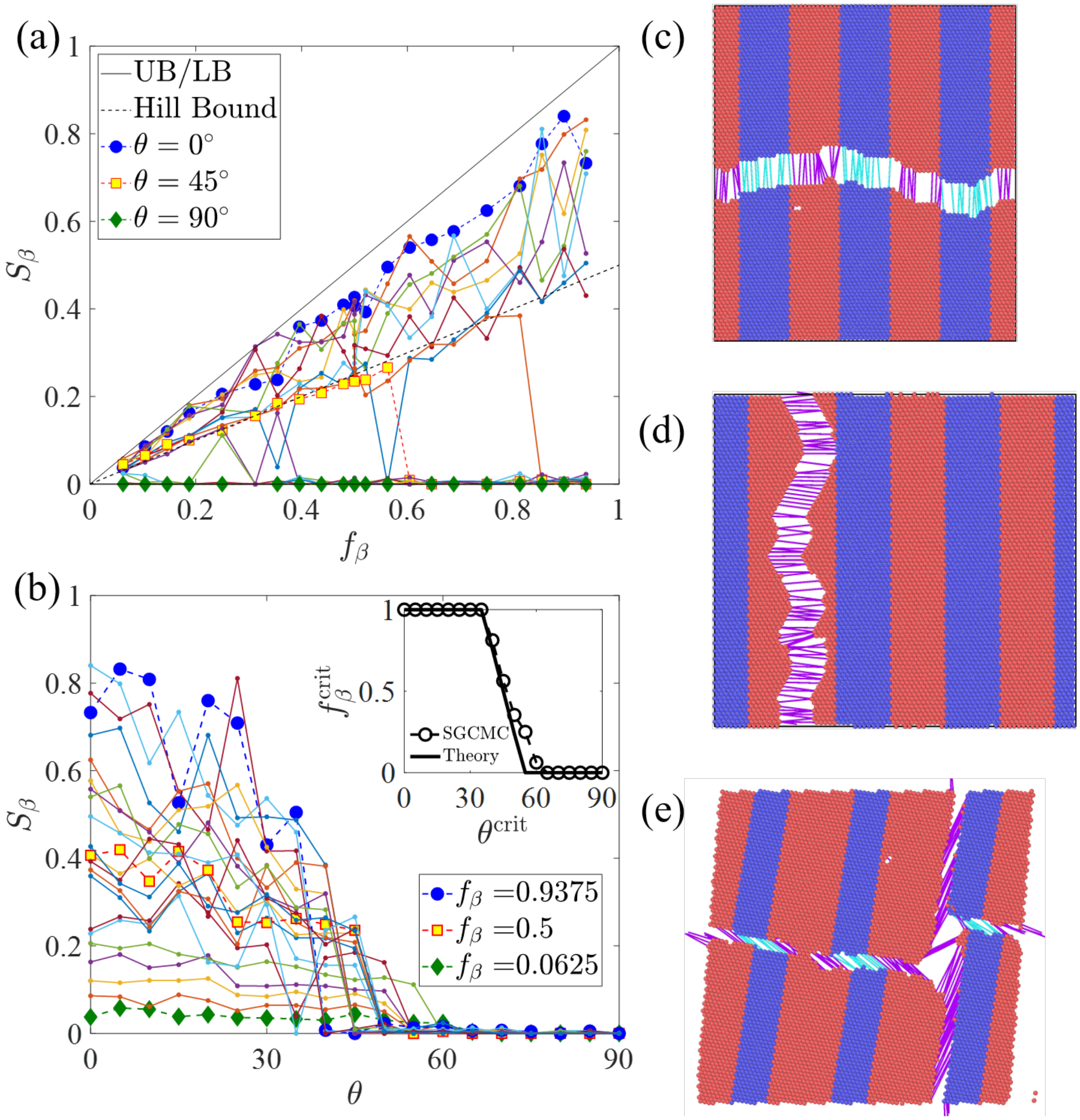

Figure 6-2: Fracture of two-phase layered material under uniaxial stretching in the semigrand canonical ensemble: (a-b) bond fraction, $S_\beta(f_\beta, \theta)$, contributing to “effective” bond fracture energy, $q^0_{br} = \epsilon^0_A + (\epsilon^0_B - \epsilon^0_A)S_\beta$; with critical state line (inset), and bond fracture patterns: (c) upper bound ($\theta = 0$), (d) lower bound ($\theta = \pi/2$), (e) Hill bound at ($\theta = \pi/4$). [SGCMC results obtained with harmonic potentials of groundstate energy ratio $\kappa_0 = \epsilon^0_\beta/\epsilon^0_A = 2$ and elastic energy ratio $\kappa_\lambda = \epsilon^\lambda_\beta/\epsilon^\lambda_A = 2$].

From SGCMC simulations we find (1) that the fracture processes in the two phases are almost uncorrelated (i.e., $\mathrm{Cov}(N_\alpha, N_\beta) = 0$), and that $S_\beta = 0$ as soon as the layered system has exhausted the equiprobable Hill bound for all f_β and θ:

$$S_\beta = H(f_\beta^{\mathrm{crit}} - f_\beta)\frac{f_\beta}{2}(3\cos^2\theta - 1) \geq 0 \tag{6.6}$$

where H is the Heaviside step function. This functional form of the participant bond fraction not only defines a range of loading angles $\theta \in [0, 54.74°]$, in which at a given volume fraction, f_β, the reinforcing phase contributes to the "effective" fracture resistance of the composite [Fig. 6-2(b)], but also defines a critical state line. When constrained by the Hill bound (i.e., $S_\beta(f_\beta, \theta) \geq S_\beta^{\mathrm{Hill}} = f_\beta/2$) a critical state line, $f_\beta^{\mathrm{crit}} - \theta^{\mathrm{crit}}$ [inset of Fig. 6-2(b)], is obtained as:

$$0 \leq f_\beta^{\mathrm{crit}} = 3\cos^2\theta^{\mathrm{crit}} - 1 \leq 1 \tag{6.7}$$

which separates – in uniaxial tension – cooperative interactions [Fig. 6-2(c)] between the two phases from exclusive interactions defined by the lower bound [Fig. 6-2(d)], once the equiprobability of bond fracture is exhausted [Fig. 6-2(e)]. Next, we consider effect of loading orientation on random and checkerboard geometries.

6.1.2 Random and checkerboard geometries

Changing orientation of the loading for the layered geometry, a geometry characterized by a definite fiber directionality, generates different S_β curves. On the other hand, for the random and checkerboard geometries, changing the orientation of the loading has no effect on the measured S_β curves (see Fig. 6-3). The order parameter S_β, in both these cases, is independent of loading orientation as a result of the lack of a single fiber orientation, as opposed to the layered composites, where the fiber orientation is clearly defined. This reaffirms the definition of θ as the angle between the loading and geometry vectors. In terms of fracture resistance, the random and checkerboard geometries are more suited for use in applications where the loading

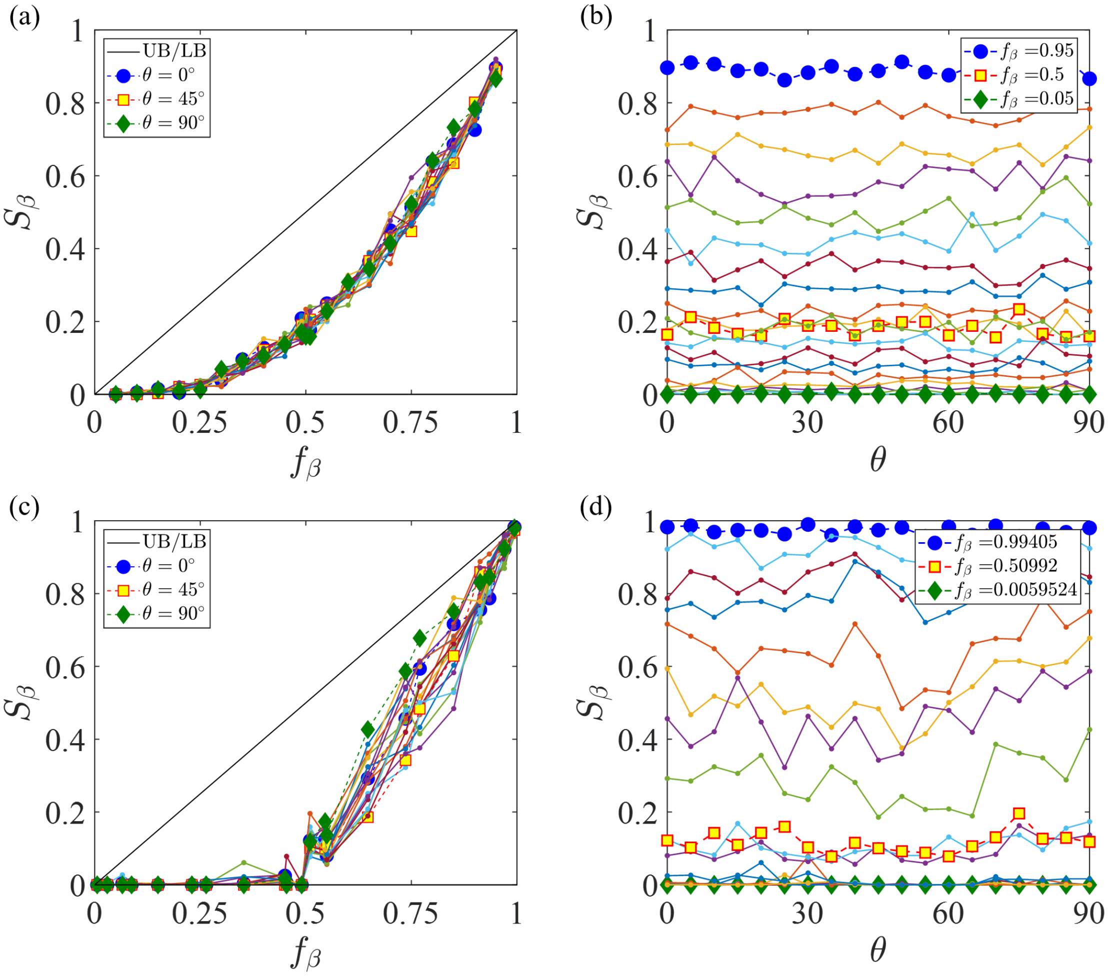

Figure 6-3: Fracture resistance of random and checkerboard geometries are independent of loading orientation. For any θ, the participant volume fraction is the same for the (a) random and (c) checkerboard geometry. As a function of θ, the participant volume fraction fluctuates around a flat line, i.e. independent of the angle,for both (c) random and (d) checkerboard geometries. [SGCMC results obtained with harmonic potentials of groundstate energy ratio $\kappa_0 = \epsilon^0_\beta/\epsilon^0_A = 2$ and elastic energy ratio $\kappa_\lambda = \epsilon^\lambda_\beta/\epsilon^\lambda_A = 2$].

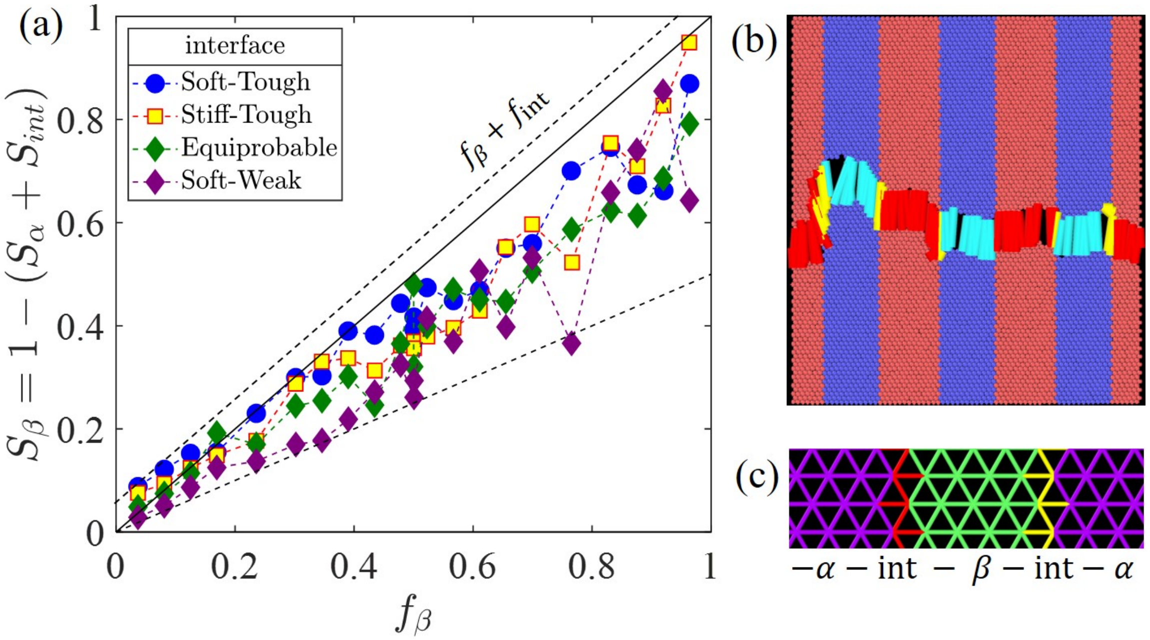

Figure 6-4: Elastic toughening due to interfaces of two-phase layered material: (a) bond fraction of reinforcing phase, $S_\beta(f_\beta)$, contributing to "effective" bond fracture energy, $q_{br}^0 = \epsilon_A^0 + (\epsilon_B^0 - \epsilon_A^0)S_\beta + (\epsilon_{\text{int}}^0 - \epsilon_A^0)S_{\text{int}}$, with upper, lower and Hill bound of two-phase material; (b) bond fracture pattern in uniaxial stretching with (c) interface bonds as a separate phase; (d) bond interface fracture for soft-weak interfaces. [SGCMC results obtained with harmonic potentials].

direction is unpredictable, for example, due to this isotropy with respect to loading orientation.

6.2 Role of interface

A last point of inquiry we here address is the role of interfaces on the probability of bond fracture, as all results so-far obtained are obtained considering two-phase "equiprobable" interface conditions, i.e., alternating interface properties derived from the properties of the bulk phase from which the interface bond originates. This excludes weak or strong bonding at interfaces, which has been suggested as cause of fiber pull-out and delamination of inclusions in e.g. ceramic matrix composites [138, 139]. An explicit account of interface behavior requires consideration of a three phase material to estimate from Eq. (4.3) the participating bond volume fractions of bulk and interface phases, $\mathbf{S} = (S_\alpha, S_\beta, S_{\text{int}})^T$ for $S_\alpha + S_\beta + S_{\text{int}} = 1$, with interface properties $(\epsilon^0_{\text{int}}, \epsilon^\lambda_{\text{int}})$ that differ from the bulk phase properties [Fig. 6-4(c)]. By way of example, we re-consider the layered system, and investigate the impact of interface conditions (Fig. 6-4). Tough interfaces $(\epsilon^0_{\text{int}} > \epsilon^0_A)$ are expected to increase the "effective" bond fracture energy according to Eq. (4.3) within the equiprobable Hill bound of the two phase material and the upper bound of the three phase material, $f_\beta/2 \leq S_\beta \leq f_\beta + f_{\text{int}}$. Yet, an added elastic toughening is achieved when the tough interface bonds are simultaneously compliant [Fig. 6-4(a)]. That is, yet another example of the soft-tough paradigm in composite materials.

It is noteworthy that Eq. (4.2) is of a form common in data analytics, for which linear algebra methods are available to ascertain the strength of correlations. One of these methods is Principal Component Analysis (PCA), a dimensionality-reduction method which transforms a large set of variables into a smaller one that still contains most of the information in the large set (for a recent review, see [140]). PCA permits a straightforward investigation of the role of a specific phase on the overall fracture resistance, and consists of:

1. Standardizing the range of initial variables so that each phase contributes equally to the analysis:
$$\overline{N}_J = \frac{N_J - \mu_J}{\sigma_{N_J}}; \quad J = (A, B, ..., n) \tag{6.8}$$
where μ_J and σ_{N_J} are the mean value and standard deviation, respectively, of the bond number of each phase $J = (A, B, ..., n)$.

2. Determining the correlation matrix:
$$\overline{\boldsymbol{\Sigma}} = \text{Corr}(\mathbf{N}, \mathbf{N}) = \text{Cov}(\overline{\mathbf{N}}, \overline{\mathbf{N}}) \tag{6.9}$$
where $\overline{\mathbf{N}} = (\overline{N}_A, \overline{N}_B, ..., \overline{N}_n)^T$.

3. The eigenvalues and eigenvectors of the correlation matrix $\overline{\boldsymbol{\Sigma}}$ carry the information about the principal components. That is, the highest eigenvalue, $\overline{\Sigma}_I \geq \overline{\Sigma}_{II} \geq, ..., \geq \overline{\Sigma}_n$ and associated eigenvalue $\mathbf{v}_I$ quantifies the amount and

direction of the axis where there are the greatest bond number fluctuations, contributing the most to the overall fluctuation-based groundstate energy dissipation.

If the covariance matrix of the bond numbers has zero off-diagonals, then, since, the covariance is always a nonzero quantity and the matrix is symmetric, the main diagonal contains the eigenvalues of $\overline{\Sigma}$. This main diagonal would also coincide with participant bond volume fractions S_J. Fig. 6-5 plots the eigenvalues and S_J for composites with different interfaces. In all cases, the eigenvalues of the covariance matrix. The contribution of the interface to the effective fracture resistance, due its small volume fraction in the composite, is on the order of $5\% - 10\%$, but this is sufficient to cause a general trend where soft-tough interfaces provide additional toughening compared to stiff-tough, equiprobable or soft–weak interfaces. In summary, based on an evaluation of the energy release rate from fluctuations [i.e., Eq. (3.3)], the sampling of bond numbers **N** provides an explicit means to evaluate an effective bond fracture energy, from Eq. (4.2).

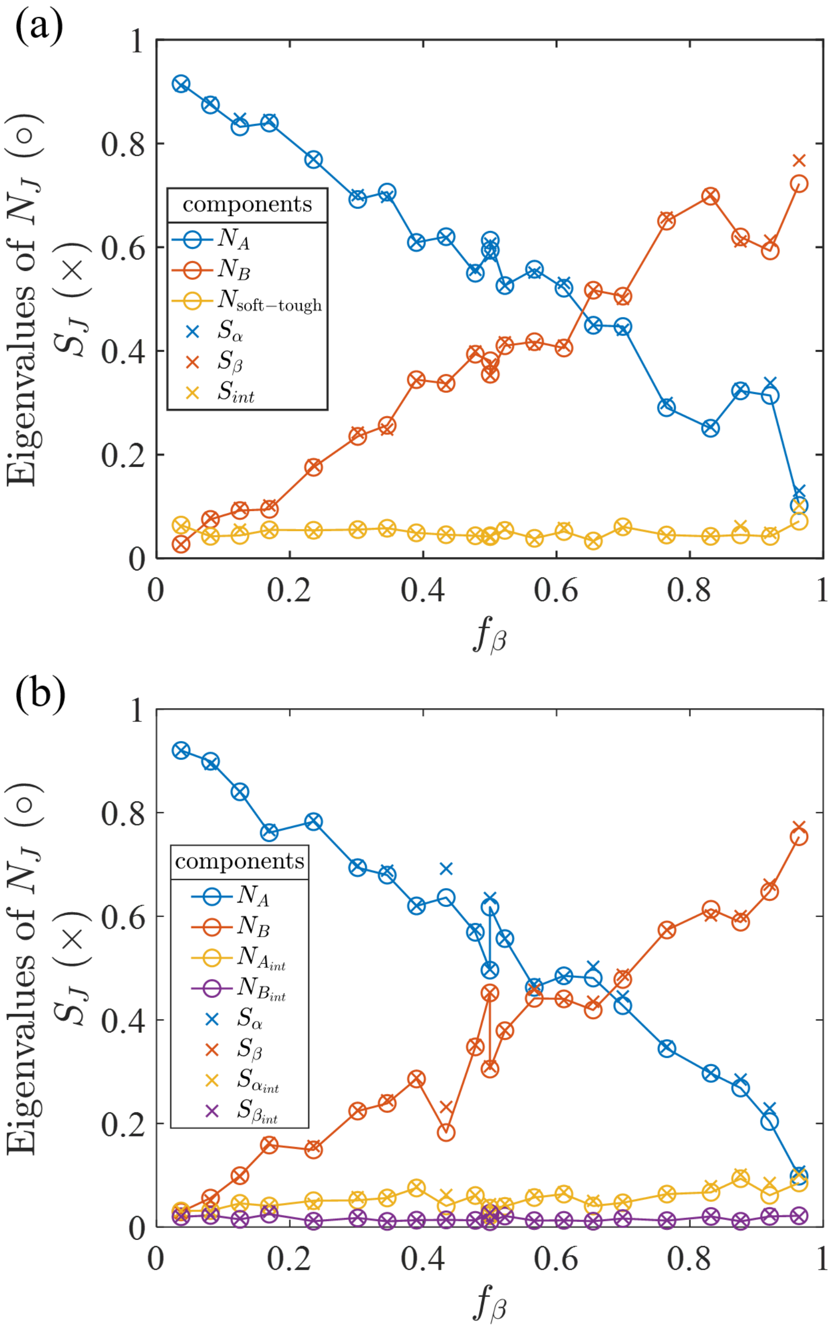

Figure 6-5: Comparison of eigenvalues of the bond number covariance matrix with the participant volume fraction of the same AB composite with different interfaces. (a) Soft-tough bonds are place at every interface creating an effective third phase. (b) The equiprobable interface is made up of alternating regions of soft-weak (A, α) and stiff-tough (B, β), so that a four phase material is effectively created.

Chapter 7

Beyond bond-view of fracture

This thesis presents a semigrand canonical picture of fracture mechanics. An overarching goal of this reinterpretation of fracture mechanics is developing a robust measure for fracture resistance of heterogeneous materials. Key insights and results are summarized in this final chapter with a prospective on future work.

Fracture is breaking of bonds. Cracks form after bond breaking. Griffith posed fracture as a sequence of bond rupture events in thermodynamic equilibrium. In addressing each of these points, equilibrium Monte Carlo simulations are designed such that the bonds, not the mass points, are the targets of trial moves. The Monte Carlo moves are performed in a semigrand canonical ensemble to allow for the necessary bond breaking that is requisite for fracture.

The ensuing developments bring on definitions of a bond rupture potential, $\Delta\mu$ and heat of bond rupture, q_{br}. Displacement-controlled tests in the equilibrium Monte Carlo simulations map out a $(\varepsilon_V - \Delta\mu)$ phase diagram, with its own set of continuous and discontinuous phase transitions, a triple point, and a critical point. From the phase diagram, universality at the critical point can be established with the 3D Ising model and brittle fracture is shown to be a discontinuous phase transition. Finally, a Griffith criterion for fracture in the semigrand canonical ensemble, suitable for homogeneous and heterogeneous materials alike, is defined as $q_{br} = 0 \leftrightarrow q_{br}^{0} = -q_{br}^{\lambda}$ at $\Delta\mu = 0$, the condition for maximum dissipation.

Developing fracture mechanics in the semigrand canonical ensemble makes use of scalar-valued averaged energy quantities such as the bond rupture potential and heats of bond rupture, $q_{br} = q_{br}^{0} + q_{br}^{\lambda}$ in an equilibrium setting. In line with the objectives of this thesis, these quantities are directly expanded to include fracture of heterogeneous materials. To this end, fracture of two-phase composites (in two and three dimensions) is analyzed through introduction of a percolation order parameter, the β-phase participant volume fraction, S_{β}, making explicit the continuous phase transition embedded in the fracture of two-phase composite materials. The participant volume fraction further allows for construction of upper and lower bounds on fracture resistance through the axiomatic bounds of a probability and volume fraction, as these quantities can only take values be between 0 and 1 (inclusive).

Two-phase composites featuring different ordered and disordered heterogeneity, interfaces, displacement-controlled loading conditions, volume fractions, and energy potential formulations can all be modeled with the semigrand canonical approach to fracture, as long as the material model can be rendered in terms of mass points and bonds. Furthermore, the semigrand canonical method maps out a path towards effective fracture toughness of heterogeneous materials through Eq. (4.2). Reexamining the steps taken to define the effective fracture resistance, q_{0}^{eff}, illustrates how effective fracture properties of materials are hidden within at least two layers of obscurity. First, the partition function presents as an intractable necessary quantity for formulation of microstate probabilities. Second, the percolation that arises due to the interplay between different phases of a composite. In this thesis, both obstacles are resolved using Monte Carlo simulations. The embedded layers of unknowns are summarized in Table 7.1.

By analyzing results of the semigrand canonical approach to fracture of heterogeneous materials through the lens of probability and percolation, we are able to identify elasticity versus texture control effects in composites. Stiffer composites, thus tend to be less fracture resistant in recurring examples of the soft-tough paradigm encountered throughout this thesis when modulating elasticity mismatch.

Table 7.1: Graphical representations of the unknown partition function, percolation order parameter, and effective fracture resistance. The partition function, Υ, is represented by an example probability mass function for an arbitrarily small system. Percolation is reprinted graphically through the tough phase participant volume fraction, S_β. Semigrand canonical Monte Carlo simulations are performed to obtain the necessary coefficients for the analytically derived effective fracture resistance, q_0^{eff}.

$\Upsilon(\Delta\mu, V, T)$	$S_\beta(f_\beta, p_c, \gamma)$	$q_0^{eff}\left(\epsilon_0^\alpha, \epsilon_0^\beta, S_\beta\right)$
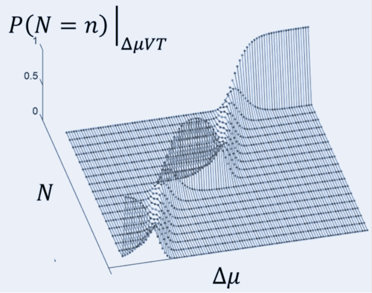	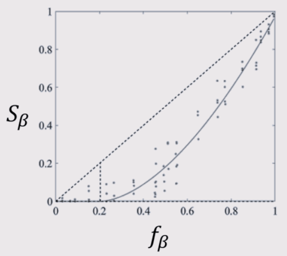	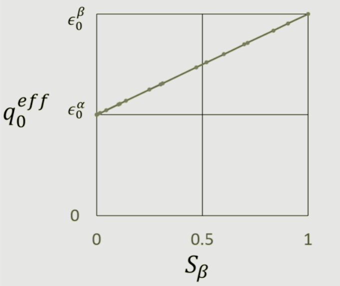

7.1 Bonding spectrum

Bonds in the model presented in this thesis are treated as springs that can only stretch or be toggled between 'on' and 'off' states. This is very much in line with a bead-spring model, and while this representation is useful for a wide range of applications, we, here, discuss further opportunities to extend the SGCMC method to model different types of chemical bonding and intermolecular interactions. Our starting point is surveying different types of bonds from intramolecular to intermolecular interactions.

Before going into too much chemistry, we begin (with English or Latin) by recognizing the distinction between the prefixes intra- (within) and inter- (between). Hence, intramolecular interactions refer to bonding *within* the same molecule. Everything else is classified as intermolecular interactions, which are not so much bonds as they are more electrostatic forces, that are much weaker than intramolecular interactions and occur *between* separate molecules. The three fundamental intramolecular interations are covalent, ionic, and metallic. Intermolecular interactions can be grouped into dipole-dipole and dispersion forces, with much more subcategories possible for each group. In what follows we will discuss these different bonds and interactions in terms of how they can be modeled in the SGCMC approach.

The three types of intramolecular interactions are ionic, covalent, and metallic. These fundamental bonds differ in the way the outer electrons of the atoms in the bond are distributed[1]. Ionic bonds form between a cation (positively charged; loses its electron) and an anion (negatively charged; gains the lost electron). The loss and gain of electrons is indicative of the large difference in electronegativities, measure of electron affinity, of the cation and anion. When the participating atoms do not have such a great discrepancy in electronegativity, a covalent bond can form where electrons are shared. Still, this sharing lies on a spectrum of electronegativity and polar colvaent bonds can form, especially when the masses of the atoms sharing the electrons are very different. For example, small hydrogen, H, atoms form polar covalent bonds with the much larger oxygen, O, atom in water, H_2O. These bonds are readily incorporated in the SGCMC method because they are distinct, localized, and permanent. Metallic bonding is distinct from the other two, because the metal atoms do not pair up and share electrons or give-and-take their electrons. Instead, all the metal atoms contribute their outer electrons to a "sea of electrons," thereby resisting the idea of a bond between two mass points. Modeling these bonds, in particular when it comes to ductility and necking, will be discussed in §7.3.

Electronegativities play a large role in the definition of the fundamental intramolecular interactions; they do so in terms of intermolecular interactions, as well. Charge differences within a molecule result in dipoles, oppositely charged ends in the same molecule, that can interact with dipoles that from in another molecule. These dipoles can be permanent, as in the case of ions and polar covalent bonds, or they can be temporary, since the the moving electrons in all atoms can, at any given instance, concentrate in one position in the electron cloud. Dipoles can also be induced because electrostatic forces of a nearby permanent dipole act on the electrons of a neighboring molecule. In terms of the SGCMC method, permanent dipoles can be treated as static bonds used for Monte Carlo trial moves. However, temporary and induced

---

[1] The three types of intramolecular interactions can be represented in a van Arkel–Ketelaar (VAK) triangle, which illustrates the differences in electonegativity of the atoms participating in the bond, underscoring the fact that these bonds lie on a spectrum.

dipoles pose challenges because they cannot be treated as static particles. All intermolecular interactions are further influenced by temperature and electrostatic forces, which brings in extra parameters in the simulation (for a discussion on temperature effects see Appendix B). These different definitions of a bond need to be fixed before running SGCMC simulations and this is discussed next.

First, the SGCMC method requires identification of the particles on which the MC trial moves will act. Second, the appropriate assumptions about all the different types of bonds and interactions will explictly define the system and physical phenmomen being modeled. For example, frozen water, or ice, is a solid made up of polar covalent bonds and hydrogen bonds. When modeling fracture of ice, the bonds that break are the hydrogen bonds, a special case of dipole-dipole interactions that emerge when hydrogen is one of the atoms involved. Morevoer, modeling ice means the temperature must be set low enough that fracture tests on the ice can be performed. Another example is salt. Salt contains ionic bonds between sodium and chloride ions and ionic-dipole bonds between salt molecules. When you model fracture of salt, you are, again, breaking the intermolecular bonds, not the much stronger intramolecular, ionic bonds. Therefore, modeling intermolecular interactions in the SGCMC method is possible, but it depends on the particular situation and requires a few assumptions specific to the phenomena being modeled.

Allowing intermolecular interations means considering pair-wise and long-range Coulombic potentials as opposed to bonded interactions. Bonded interactions work exceedingly well in terms of a semigrand canonical ensemble where the total number of broken and intact bonds is always a constant, and a bond list can be defined with the geometry of the simulation. Nonbonded potentials would relax this constant reservoir constraint, but, as such, in terms of Monte Carlo simulations, grand canonical insertion and deletion moves from an infinite reservoir must also be performed. Here, the choice becomes whether or not to stay in a semigrand canonical ensemble with added grand canonical moves or move entirely to a grand canonical setting. In addition to reformulating the ensemble, the practical aspects of the Monte Carlo simulation will have to be addressed for disappearing and reappearing nonbonded interactions. This fleeting behaviour is readily handled by most molecular software packages, and the challenge is mostly on the accounting side of things, keeping track of the number nonbonded interactions and their state ('on' or 'off'). In this regard, a different running measure might be more useful in these simulations.

Nonbonded interactions, still, might be too cumbersome to deal with in a semi-grand Monte Carlo simulation. Instead of trying to attempt the Monte Carlo trial moves on these nonbonded interactions, it might be more efficient to build-in the "Monte Carlo trial moves" into the functional forms of the potentials, directly. This amounts to creating step-function potentials that mimic the 'on' and 'off' trial moves of the Monte Carlo simulation. The acceptance probabilities for the Monte Carlo moves would have to be included in these potentials, as well, and care must be taken to construct the equations in a way that minimizes computational overhead in the simulations. For example, the MC-augmented potentials should not try to attempt a step-function switch at every timestep, so a timer could be added so that the slower acceptance probability evaluations are performed only at certain intervals.

7.2 Positive and negative heat release

Two tenets of the bond-view of fracture are (1) realizing fracture and crack propagation are the aftermath of bond breaking and (2) treating the bonds in a system as particles that can be directly probed, for example, through Monte Carlo trial moves. As particles, the energy of each bond is explicitly defined, but bonds are only one example of a cohesive element in a material. Specifically, bonds are line segments defined by two mass points in a system, and therefore constitute the manifestation of two-point energy interactions. Similar to how two mass points define a bond, two bonds (that share one mass point) define an angle, which can be viewed as a three-body interaction. Upscaling the interactions, further, we can consider two planes (that share share two mass points) that contain four mass points to define four-body interactions. Here, we discuss the extension of the SGCMC approach to include four-body interactions, specifically in dealing with flexural versus tensile toughness of a material.

Adding n-body interactions in the SGCMC approach amounts to adding more particles in the system. Monte Carlo simulations need to be run longer to make sure enough particles are sampled. In the four-body, $n = 4$, extension, for example, SGCMC trial moves will now include turning 'on' or 'off' bonds, N_B, and dihedral angles, N_D. Introducing the variables N_B and N_D allows us to write the total number of particles as $N^0 = N_B^0 + N_D^0$, the point being that now the different types of particles (bonds and dihedrals) can readily be handled by the heterogeneous implementation of the SGCMC method presented in Chs. 4-6. The SGC Griffith criterion of fracture, Eq. (3.4), remains unchanged. All that changes is that the energy potentials are now the sum of the energy potential of the two types of particles, $U^x = U_B^x + U_D^x$ for $x = 0, \lambda$, again reinforcing the direct application of the heterogeneous implementation of the SGCMC method. The reason this extension is possible is because the SGCMC Griffith criterion only requires equal and opposite heat release. Heat release from strain energy is negative, meaning energy needs to be put into the system to strain it. Heat release from the groundstate energy is positive because this is the energy inherent to the system.

Groundstate energy heat release, in particular, becomes an added degree of freedom in the system when considering multiple n-body interactions. Keeping with the $n = 4$ case, there are two groundstate energies: that of the bonds, $\epsilon_B^0 = \sum_{i=1}^{N_B^0} \epsilon_{B,i}^0$, and that of the dihedral angles, $\epsilon_D^0 = \sum_{i=1}^{N_D^0} \epsilon_{D,i}^0$. The question becomes how to split the total system groundstate energy between the two different types of particles. Here, again, is another direct implementation of the SGCMC method as presented in Ch. 3. Since the ratio of dihedral to bond groundstate energy is an unknown, treat it as a parameter and do a parameter study. Let us call this parameter $\phi = \frac{\epsilon_D^0}{\epsilon_0^B}$, and vary ϕ very much in the same way $\Delta\mu$ is varied when generating the phase diagram of brittle fracture. This time, however, the plot of interest is the critical strain at failure versus ϕ. Considering the range $\phi = 0$ to $\phi \rightarrow \infty$ will capture the spectrum of loading from pure stretching to pure bending.

7.3 Other ensembles

Material presented in thesis is constrained to brittle failure. This is because the semigrand canonical ensemble is used exclusively in homogeneous and multi-phase heterogeneous materials, with *localized* bonds that can only ever be broken or stretched. In other words, no further mechanisms of energy dissipation can be simulated with this model. An immediate extension of this work would be to ease this restriction. For example, future work can include constructing plasticity, rheology, or ductility based semigrand canonical trial moves where a bond can take intermediate damage states between intact (no damage or elastically stretched) and broken (complete loss of modulus and ability for force transmission). Different ensembles can be chosen that allow for different Monte Carlo trial moves to model work of plasticity, for example, for metallic bonding. For example, a Gibbs ensemble that allows MC moves that change the type or species of a particle can be useful in modeling certain fracture dissipation mechanisms at the crack tip. Here, again, manipulating the functional forms of the energy potentials can be useful when mimicking different ensembles by introducing coefficients that directly change the value of the energy parameters of the energy functional. While this holds great promise in terms of the mechanics canon, establishing the proper statistical mechanics framework may prove to be a nontrivial endeavor.

7.4 Estimating the number of broken bonds

We look back at all the hundreds of thousands of simulations that have been performed and make an observation as to how many broken bonds it takes to fracture a material. In doing so we connect our method to relevant work in extreme value theory and fracture mechanics [24, 25, 141–145].

We remain with our bond-view approach to fracture mechanics and idealize the crack as a line and a plane in two and three dimensions, respectively. In doing so we have begun to underestimate the number of broken bonds it would take to fracture a material. As we have seen in many examples throughout this thesis, the crack is more tortuous than an idealized line or plane (see Figs. 3-6, 4-3, 5-2). Furthermore, we pay no attention to the microstructure in estimating the number of broken bonds that constitute a macrocrack, and instead discretize the simulation model based on its dimension, d, and total number of bonds, N_0. In two dimension this corresponds to a square of side lengths $\sqrt{N_0} \times \sqrt{N_0}$, in three dimensions, a cube of side lengths $\sqrt[3]{N_0} \times \sqrt[3]{N_0} \times \sqrt[3]{N_0}$, and in d dimensions, a d-dimensional hypercube of side length $\sqrt[d]{N_0}$.

With the expression of the dimensions of the bond lattice model in hand, we proceed by removing one dimension, effectively prescribing the fracture to happen in dimension $d-1$. This gives us the idealized crack line and plane in two and three dimensions, as shown in Fig. 7-1(a, b), respectively. Next, we construct a dimensionless ratio of broken bonds to total bonds as a measure of the bonds that break during fracture.

We start with the numerator of the ratio, the number of broken bonds across the idealized crack line and plane in two and three dimensions, represented by the white line and light blue plane in Fig. 7-1(a, b), respectively. The numerator represents the volume of the broken bonds in d dimensions. The broken bonds are prescribed to exist in $d-1$ dimensional-space, so the area of the broken bonds is $\sqrt[d]{N_0}^{d-1}$. To get the volume measure of the broken bonds an additional factor is required in the numerator as a thickness to be multiplied with the area. The thickness is effectively the measure of the number of bonds that the area cuts through as a crack is created and bonds are broken. Coordination number is inherently attributed to mass points in a lattice and not the bonds, so that the coordination number is a density measure of bonds per mass point, i.e. an inverse density measure with respect to the bond-view method. The coordination number Z, thus, acts as a bond-volume element per mass point, and this volume element, just like a mass point, can be situated anywhere in the $(d-1)$-dimensional space of broken bonds. Therefore the desired thickness is $\left(\frac{Z}{2}\right)^{\frac{1}{d-1}}$, where a correction factor of 2 is included because of the double-counting of bonds shared by two mass points in the definition of Z. Implied in this definition is the assumption that all the bonds in the volume, generated by sweeping the derived thickness, $\left(\frac{Z}{2}\right)^{\frac{1}{d-1}}$, over the area, $\sqrt[d]{N_0}^{d-1}$, will break. This yields an upper bound estimate of the number of broken bonds at fracture, and the numerator, as $\left(\frac{Z}{2}\right)^{\frac{1}{d-1}} \sqrt[d]{N_0}^{d-1}$.

In all dimensions the denominator is the bond-volume of the total bonds $\left(\sqrt[d]{N_0}\right)^d = N_0$, represented by the dark blue d-dimensional volumes in Fig. 7-1(a, b). Finally, we can construct the upper bound dimensionless ratio of broken bonds to total bonds by combining the derived numerator and denominator and simplifying to obtain:

$$\frac{N_{\text{broken}}}{N_0} < \left(\frac{Z}{2}\right)^{\frac{1}{d-1}} {N_0}^{-\frac{1}{d}} \tag{7.1}$$

where $Z = 6$ and $Z = 12$ are the lattice coordination numbers for the triangular and face-centered cubic (FCC) lattices in two and three dimensions, respectively. The interpretation of Eq. (7.1) follows directly from the graphical derivation in Fig. 7-1(a, b).

The form of Eq. (7.1) can be derived a second way by making use of the dimensional spaces in which each bond identity exists. From the outset we have presecribed the broken bonds to lie in $(d-1)$-dimensional space. The intact bonds, on the other hand, belong in d-dimensional space. Then, using the equation for the side length of a d-dimensional hypercube, $\sqrt[d]{N_0}$, the same ratio in Eq. (7.1) can be constructed as the ratio of the side lengths of the hyper-dimensional cubes in which the broken and intact bonds exist. The side length of the broken bonds hypercube is $\sqrt[d-1]{\frac{Z}{2}}$ becasue as discussed earlier the coordination number, Z, is a bond volume element (and the factor of 2 corrects for double-counting). The side length of the intact bonds hypercube is $\sqrt[d]{N_0}$. Here, the assumption is made that the number of broken bonds is much less than the number of intact bonds, such that, $N \approx N_0$. Taking the ratio of these two side lengths recovers Eq. (7.1).

Simulation measurements of the ratio of broken bonds to the total number of bonds in two and three dimensions are shown in Fig. 7-1(c, d). In both cases, the predicted upper bound in Eq. (7.1) is in excellent agreement with the simulation results. In the

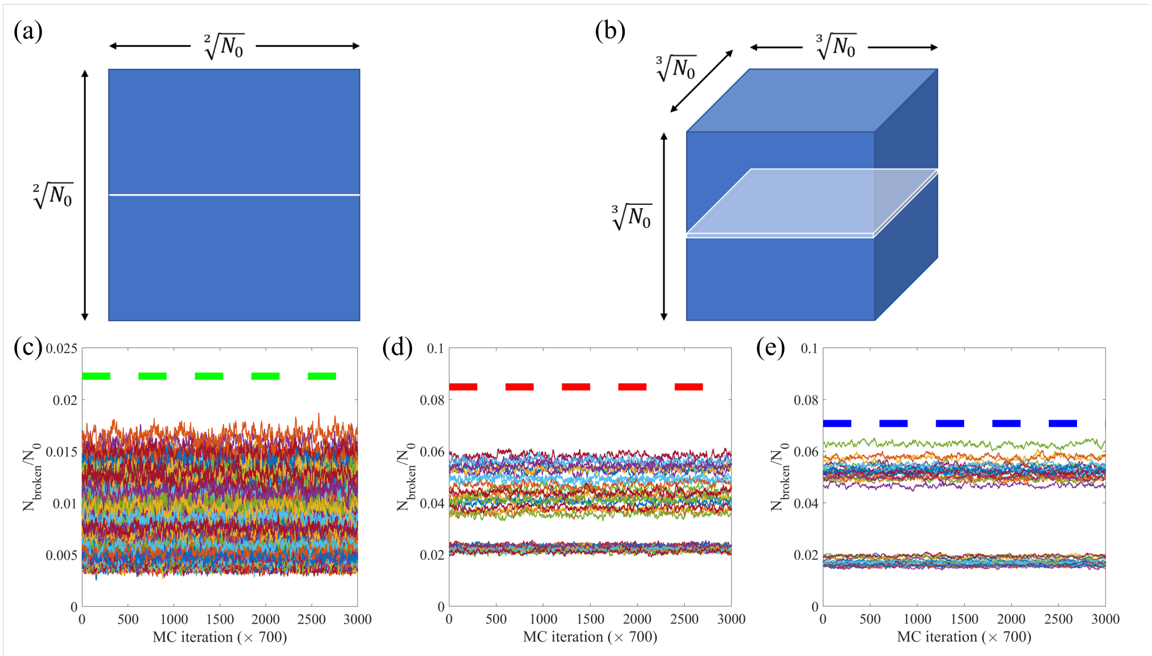

Figure 7-1: Upper bound for number of broken bonds at fracture. Schematics motivating the derivation of the upper bound of the number of broken bonds at fracture for (a) two- and (b) three-dimensional systems. The blue regions correspond to intact material; the white horizontal line and light blue plane correspond to an idealized crack in the material. Broken number of bonds as measured during Monte Carlo simulations are shown for (c) two- and (d, e) three-dimensional systems. The (c) green, (d) red, and (e) blue thick dashed lines correspond to the predicted maximum percentages of bonds that will break for two-dimensional systems with $N_0 = 18,144$, 2.23% and three-dimensional random, $N_0 = 24,00$, 8.49%, and checkerboard, $N_0 = 41,472$, 7.08%, systems, respectively. The upper bound only depends on dimension, d, total bond number, N_0, and coordination number, Z, and is independent of volume fraction, composite geometry, or loading orientation.

case of two dimensions, ($d = 2, N_0 = 18,144, Z = 6$), the upper bound is calculated to be 2.23%. In three dimensions, we have two upper bounds corresponding to two different total number of bonds corresponding to the 10 x 10 x 10 (random geometry) and 12 x 12 x 12 (checkerboard geometry) FCC lattices. For the smaller FCC lattice, ($d = 3, N_0 = 24,000, Z = 12$), the upper bound is calculated to be 8.49%, and for the larger FCC lattice, ($d = 3, N_0 = 41,472, Z = 12$), the upper bound is calculated to be 7.08%. From these results we can see dimension alters the number of broken bonds by more than 300%. It takes far fewer broken bonds to fracture a material in two dimensions than it does in three dimensions, supporting the results of lower percolation thresholds in three dimensions and in line with linear elastic fracture mechanics (see discussion in Ch. 5).

7.5 Correlation lengths of fracture surfaces

Given the analytical link between energy and geometry through the participant volume fractions and two-point correlation functions, respectively, analytical results from SGCMC, summarized in Table 7.2 (see Chs. 4-6), suggest that the effective fracture toughness of heterogeneous materials can be measured from fracture surfaces in experiments. Statistical physics approaches have been employed in terms of studying fracture surfaces, but the finding of universality of exponents in the fracture surface roughness has proven to be a red herring. Recent experiments have focused on the correlation measured from the fracture surface and report a linear relation between the fracture toughness and these correlations for aluminum alloys [132]. The SGCMC results predict a linear slope of unity but this is because the units in SGCMC are per bond number whereas the units in experiment are per area. This difference in units is readily reconciled when using the coordination number as a conversion factor as demonstrated in §7.4, where the expected slope of $Z = 12$ is a good approximation of the measured slope of 12.49 from experiments. The measured slope is taken from the plot of the normalized lateral fracture surface correlation length versus fracture toughness measured by the J-integral [132]. Furthermore, when measuring the

Table 7.2: Energy, geometry, and probability descriptors of fracture of heterogeneous materials in the semigrand canonical ensemble. From purely energy considerations derivatives of the groundstate energy yield important quantities such as the heat of groundstate bond rupture and participant volume fractions for each phase in a composite (where $M^J = N^J_{br} = N^J_0 - N^J$ is the number of broken phase J bonds). From geometry considerations the participant volume fraction is exactly the two-point correlation function of the fracture surface at $r = 0$. The dual probability definition of the participant volume fraction further adds to the analysis (where L, R and K stand for the layered, random and checkerboard geometries, respectively).

Energy	Geometry	Probability
$U_0 = -\epsilon_0^i N^i$ $q_0 = -\frac{dU_0}{dN} = \epsilon_0^i S_i$ $S_\beta = -\frac{d^2 U_0}{d\epsilon_0^\beta dN} = \frac{dN^\beta}{dN}$ $= \frac{M^\beta}{M}$	$S_2^\beta(r=0) = S_\beta$ $l_c^\beta = -\frac{S_\beta}{S_2^{\beta\prime}\Big\rvert_{r\to 0}}$	$S_\beta = \int P[\beta \mid f_\beta]\, dP$ $L: P[\beta \mid f_\beta, \theta] = \cos\theta$ $R: P[\beta \mid f_\beta] \propto f^{\gamma-1}$ $K: P[\beta \mid f_\beta] = \frac{H}{\int_0^1 H\, df_\beta}$

fracture surface height correlation length, the slope is reduced to 9.31, and the coordination number must be discounted by the ratio of the planar densities of ⟨110⟩ to ⟨100⟩ planes yielding an expected slope of 8.5 [132]. This agreement between our analytical results and experiments from literature is further validation of the method and describes new paths forward in fracture mechanics characterization of heterogeneous materials through the participant volume fractions and their link to fracture surfaces.

It is remarkable the analytical SGCMC predictions come so close to the experimental results, even though throughout this thesis we have only considered brittle fracture while aluminum alloy exhibits ductile failure. This suggests the derived equations in the *Energy* column of Table 7.2 are independent of the failure mechanisms.

7.6 Outlook

The method presented in this thesis is the first of its kind to the knowledge of the author. Applying an established statistical mechanics framework to the long-standing problem of fracture of heterogeneous materials, and even homogeneous materials, yields several insights. The current SGCMC method is firmly rooted in static equilibrium statistical mechanics. The Monte Carlo simulations performed erase any time-dependence, meaning crack velocity, tracing of the crack roughness, crack propagation, and dynamic fracture behavior require extension of the method considering nonequilibrium statistical physics, including nonequilibrium Monte Carlo methods [146–150].

There are still further developments that can be made to the present semigrand canonical method and problems to explore including augmenting the phase diagram to include temperature on a third axis, examining different heterogeneous and porous structures in three dimensions, geometric studies on the crack paths and tortuosity output from simulations, experimental determination of the S_i from fracture surface semantic segmentation imaging, and much more. This thesis establishes some key concepts in introducing and applying the semigrand canonical approach to fracture and lays unbounded paths forwards towards greater discoveries and insight.

Appendix A

Notched cases

We extend the application of this fluctuation-dissipation based method of fracture mechanics beyond the homogeneous linear and nonlinear cases to deal with notched systems. Notched systems are created by removing bonds from the center of the simulation model, and we deal with four cases corresponding to 4, 12, 24 and 40 removed bonds in the 10 x 10 x 10 face-centered cubic (FCC) lattice.

A.1 Notch creation

We define the reference configuration of a lattice as the fully bonded and unloaded state of the lattice. A notch is created in the reference configuration of the lattice by removing bonds from the bond list of the system, such that a fully bonded system does not include removed bonds. This bond removal is different from the Monte Carlo move of turning a bond OFF in the semigrand canonical ensemble. First, we do not randomly turn off bonds according to an acceptance criterion. Instead, the bond removal is deterministic and set by the reference lattice as a part of the simulation geometry definition. Second, removing a bond from a bond list means it is no longer available for performing Monte Carlo trial moves. The removed bond can never be turned ON or OFF, and the removed bond is not counted in the tally of bonds. In this sense a removed bond is not a bond that is turned OFF. The removed bond is a nonexistent bond, similar to how there is never any material between crack faces in

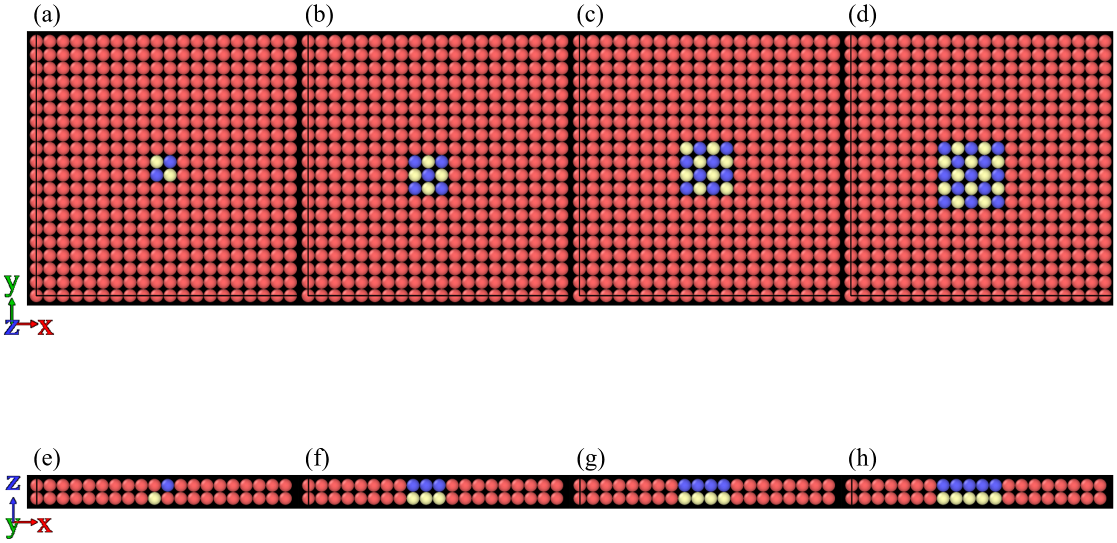

Figure A-1: . Top view of the 10 x 10 x 10 FCC lattice with (a) 4, (b) 12, (c) 24, and (d) 40 bonds removed. (e-h) Side view of the same showing the top (blue) and bottom (yellow) crack faces.

a an idealized infinitely thin crack.

To remove a bond from the reference lattice, a set of mass points are designated as the end points of the bonds to be removed. Then, all bonds between these, and only these, mass points are removed from the bond list. The mass points that form the endpoints of removed bonds are given unique types to differentiate them from the rest of the system. Removing bonds creates a crack in the system. The top and bottom crack faces are the blue and yellow mass points as shown in Fig. A-1(e-h), respectively. No bonds exist between blue and yellow mass points as these are the top and bottom crack faces, respectively. Bonds between blue and blue, yellow and yellow and any mass point with red are allowed and form the reference lattice configuration. In this way, we create as thin a crack as possible in the FCC lattice.

Removing different numbers of bonds alters the constant number of total bonds, N_0, in the system. Recall from Ch. 2, Eq. (2.2), N_0 is the sum of all bonds, broken and intact. For the same 10 x 10 x 10 FCC lattice with a different number of removed bonds, N_0 is different for each. As we remove 4, 12, 24, and 40 bonds from the 10 x 10 x 10 FCC lattice, we generate systems with with different $N_0 = 23,996$, $23,988$,

$23,976$, and $23,960$ total bonds.

A.2 Phase diagrams for notched systems

Phase diagrams are generated for all the notched systems with both harmonic and Morse potentials, as shown in Fig. (A-2). For the same number of removed bonds, the Morse system outperforms the harmonic systems. Regardless of potential, increasing the number of removed bonds, or otherwise stated, increasing the crack area, diminishes the fracture resistance of the system as demonstrated by a smaller deformed area in the phase diagram. The smaller deformed area is due to the lower slope and critical strain at failure in domains II and III, respectively, of the phase diagrams.

A notch has a cascading effect on the phase diagram starting in domain II, where the slope of the phase boundary decreases with increased notch size, thereby reducing the area of the deformed region of phase space as expected from a notched system. When reaching domain III, due to the diminished slope of domain II the maximum critical strain is decreased for $\Delta\mu > 0$, further reducing the area of the deformed region of phase space. Notches in both linear and nonlinear systems generate a cascading effect beginning in domain II that results in a change of maximum strain at fracture in domain III.

Brittle fracture phase diagrams are characterized by $\Delta\mu_{gas}$, the slope $\epsilon_V/\Delta\mu$, and the critical failure at strain, ϵ_V, in domains I, II, and III, respectively. The cascading effect of notches works through changing the slope in domain II, which ultimately changes the critical failure strain in domain III. The gas phase in domain I is affected through the change in the value of the strain at the critical point (continuous phase transition discussed in Ch. 3) because the critical strain in domain III is altered. However, $\Delta\mu_{gas}$ remains unaltered regardless of the notch size in the system. The presence of a notch is of no consequence to the unbonded gas-like system, being the limit case of the size of notches. Furthermore, as the triple point occurs at $\Delta\mu_{gas}$ at or near zero strain, the only energy in the unstrained and simultaneously bonded and unbonded system is the groundstate energy, which is a constant that is also

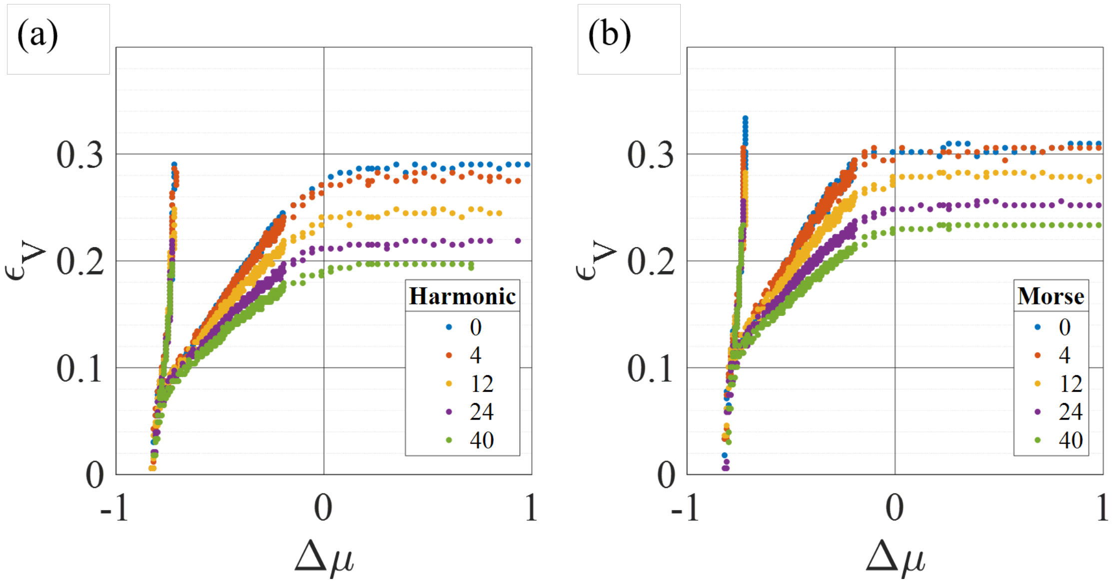

Figure A-2: Phase diagrams of notched systems. Phase diagrams shown for systems with (a) harmonic and (b) Morse potentials. Notches change the slope of domain II, which reduces the maximum strain in domain III. The triple point is unchanged by presence of notches because at the gas phase everything is broken.

independent of the size of the notch. Moreover, the constant terms in Eq. (3.6) for domains I and III reflect this effect of notches. The changing slope in domain II is simply a reflection of the lower failure strain for systems with larger notches, completely in agreement with the increased compliance with increasing crack size in linear elastic fracture mechanics.

A.3 Conclusion

Throughout this work a crack is alluded to, and is indeed an end result, but never incorporated at the reference or starting point of a simulation. This section shows the robustness of the method in being able to do just that, by removing bonds exactly where a crack would exist. A larger compliance for a larger crack area translates into a smaller deformed area and lower critical strain at failure in the phase diagrams of brittle fracture, completely in line with fracture mechanics. In effect, adding a crack, or removing bonds, at the beginning of a simulation localizes the point of crack propagation because the crack initiation is prescribed in the geometry. In terms of the semigrand canonical Monte Carlo (SGCMC) trial moves, the removed bonds are a set of prescribed, equilibrated moves, so the remainder of the simulation simply picks up where the prescribed crack left off. If the crack extended across the entire simulation box, the SGCMC simulation will be over before it ever starts because the simulation is already equilibrated.

Appendix B

Equilibrium temperature effects

The final state variable in the $\Delta\mu VT$ ensemble, temperature, is not directly probed in construction of the isotherms in this work. This is a reflection of the constant ambient temperature of the fracture experiment in simulation. Future work can incorporate the temperature as a parameter in at least two ways. First, different ensembles can be constructed at different temperatures. Second, temperature profiles can be introduced as a layer of heterogeneity. Here, we begin to examine the first scenario.

All the analysis thus far has been carried out at a constant reduced temperature, $T^* = 0.1$. In this section we begin to examine the effect of different equilibrium temperatures for a harmonic system (see Figure B-1), considering a high temperature, $T^* = 1.0$, and a low temperature, $T^* = 0.01$. Recall the choice of $T^* = 0.1$ is to position the work in terms of the fracture of a solid. The high temperature reduces the system to a gas-like state unable to resist loading, effectively pushing $\Delta\mu_{gas}$ to 0. In consequence, there is no domain II and $\epsilon_V^{crit} = 0$ in domain III; the phase diagram is a flat line. This all indicates the system as a solid is already broken and unable to carry load.

Moving in the opposite direction, on the temperature scale, we immediately see the effects of a lower temperature, $T^* = 0.01$, in the phase diagram. Starting in domain I, $\Delta\mu_{gas}$ ($\approx -\epsilon_i^0$) is shifted to lower values of the bond rupture potential, as expected for colder temperatures. In consequence, the larger range of $\Delta\mu$ in domain II leads to a higher critical strain reached in domain III. There is also a slight increase in the slope of domain II for the lower temperature system, which further leads to an increase in the critical strain in domain III. Higher temperatures lead to lower slopes of the phase diagram in domain II, as seen in the zero slope in domain II for the $T^* = 1.0$ system. Finally, domain III exhibits a critical strain that is inversely proportional to temperature. This comes as a direct result of the definition of $T^* = \frac{k_B T}{\epsilon_i^0}$, where the groundstate energy is inversely proportional to the reduced temperature. These observations demonstrate the versatility of the method. But more involved studies are required to fully map the third dimension of the phase diagram of brittle fracture.

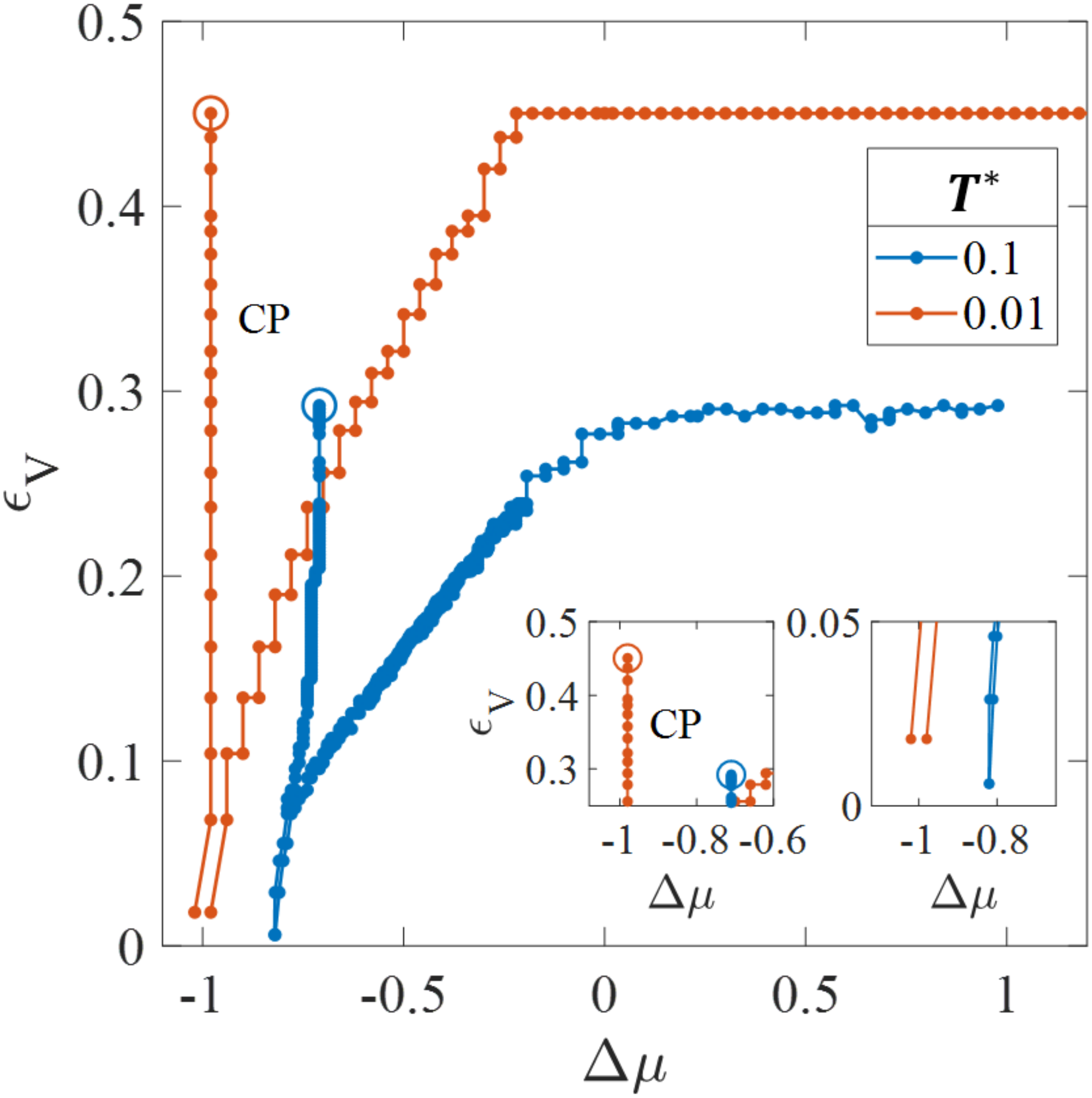

Figure B-1: Phase diagrams for different temperatures. Where the undeformed system is a solid at equilbrium, the phase diagram exhibits all domains I, II, and III. Lower temperatures (red line), $T^* = 0.01$, shift μ_{gas} to the theoretical limit of $-\epsilon_i^0$ in domain I. For intermediate temperatures, μ_{gas} moves closer to $\Delta\mu = 0$. At higher temperatures the domain II collapses to a point where $\Delta\mu_{gas} = 0$, and the system is broken for all $\Delta\mu$, leaving domain III to be a ray at $\epsilon_V = 0$ pointing in the direction of positive $\Delta\mu$ (not shown).

Appendix C

Fracture in the grand canonical ensemble

A grand canonical Monte Carlo Approach (GCMC) is proposed for the fracture analysis of solids discretized as mass points and bond interactions. In contrast to classical load-driven fracture processes, the GCMC approach introduces an auxiliary field, the bond rupture potential μ, to which the system is subjected; in addition to changes in volume V and temperature T. In this μVT-ensemble, bond isotherms that link the average number of bonds to the bond rupture potential $(N_k - \mu)$ are obtained that carry critical information for fracture analysis. Specifically, the slope of the bond isotherm reflects bond fluctuations, permitting identification of (1) a fluctuation-based damage variable, and (2) the competition in energy fluctuations between the redistribution of strain energy induced by bond rupture, and the dissipation of the groundstate energy. Based on these fluctuations, it is shown that the GCMC-approach allows the identification of a critical bond energy release rate of material samples, when strain energy fluctuations equal groundstate energy fluctuations – much akin to Griffith's 1921 stationarity postulate to "predicting the breaking loads of elastic solids". This is illustrated by means of thermodynamic integration of bond isotherms to determine force-displacement curves, for both notched and unnotched homogeneous samples discretized by regular two-dimensional lattices with bonds exhibiting harmonic potentials.

C.1 Griffith's postulate

In his groundbreaking 1921 paper "The phenomena of Rupture and Flow in Solids" [1], which defined much of the course of engineering mechanics over the past 100 years, Griffith postulated that in the course of fracture propagation (crack surface Γ) the "total diminution of the potential energy of the system, due to the presence of the crack" is the difference between the "increase of strain energy due to (...) a very narrow crack", W, and the "potential energy of the surface of the crack", U, associated with surface tension. The first is recognized –with opposite sign– as the variation, at constant volume, of the Helmholtz free energy $F = -W$, the second as Gibbs surface energy, $U = 4\Gamma\gamma_s$ (with Γ the crack surface, γ_s the surface tension) so that the "condition that the crack may extend" at constant load equals– in his own words [1]:

$$\frac{\partial}{\partial\Gamma}(W-U)=0 \tag{C.1}$$

Griffith's postulate of the stationarity of $W-U$ during fracture propagation is based on his assessment that his theory was able to extend the realm of the "theorem of minimum potential energy to predicting the breaking loads of elastic solids". But it was later recognized that the stationarity postulate (C.1) based on the First Law of Thermodynamics ignores the very nature of fracture; that is irreversibility. Griffith's theory was thus rephrased by invoking the more appropriate 2nd Law of Thermodynamics leading to the introduction of energy release rate and its critical (threshold) value the fracture energy. That is, the creation of fracture surface, $d\Gamma \geq 0$, in an elastic solid between two equilibrium states at controlled boundary conditions, with both satisfying the minimum potential energy theorem, dissipates in a displacement- (or volume) controlled situation the free energy in the form:

$$d\mathcal{D}=\mathcal{G}d\Gamma\geq 0;\mathcal{G}=-\left.\frac{\partial F}{\partial\Gamma}\right|_{VT}\leq\mathcal{G}_F;\ d\Gamma\geq 0 \tag{C.2}$$

where $\mathcal{G}$ is the energy release rate, and $\mathcal{G}_F$ the fracture energy. Since Griffith, the classical way of fracture mechanics consists in sweeping a load protocol of (generalized) "volume" changes to determine when the energy release rate $\mathcal{G}$ reaches the fracture energy $\mathcal{G}_F$. As an alternative, and motivated by Griffith's stationarity postulate, it is of interest to explore the fracture propagation criterion as a minimization problem in the form:

$$(\mathcal{G} - \mathcal{G}_F)\, d\Gamma = - \left.\frac{\partial}{\partial \Gamma}\right|_{VT} (F + \mathcal{G}_F \Gamma)\, d\Gamma = 0 \tag{C.3}$$

or equivalently, considering the fracture surface as a number of broken bonds $N_0 - N$ caused by fracture surface creation (with N_0 the number of initial bonds, and N the number of intact bonds as the sample is stretched):

$$\left.\frac{\partial}{\partial N}\right|_{VT} (F - \mu N)\, dN = \left.\frac{\partial \Omega}{\partial N}\right|_{VT} dN = 0 \tag{C.4}$$

where μ is coined bond rupture potential; and $dN \leq 0$ the change in bond number. The minimization problem thus defined by Eq. (C.4) is a minimization of a grand potential, $\Omega = F - \mu N$, in the grand canonical thermodynamic ensemble, when considering instead of the number of particles the number of onds, N, and instead of the chemical potential the bond rupture potential, μ. If one considers a fracture process as a sequence of constrained equilibrium states (i.e. what is generally referred to as quasi-static fracture [73]), the solution of the minimization problem (C.4) can make use of the rich canon of grand canonical Monte Carlo (GCMC) Techniques employed in molecular simulations of fluid properties [151], adosrption-desorption and condensation phenomena in porous materials [105, 106], phase separation phenomena [152], and so on (see [68]).

It could be argued that recently developed variational principles for damage phase field models for fracture based upon the global minimization of a Griffith-like functional, composed of a bulk and a surface energy term, pursue a similar minimization path – in a continuum fashion [153–156]. However, in contrast to these continuum approaches that remain in the classical framework of displacement-driven boundary conditions (equivalent to the so-called canonical (NVT) thermodynamic ensemble), our approach focuses on Griffith's postulate in the grand canonical ensemble (μVT). It will be shown that the choice of this thermodynamic ensemble (and associated potential, i.e. grand potential Ω) suggests a new route to the solution of fracture mechanics problems; the GCMC approach.

That is, the focus of this thesis is to explore the GCMC method as an alternative to classical displacement–driven fracture mechanics approaches. The method is first developed, before it is applied to a series of homogeneous solid samples with and without notches, discretized by regular two-dimensional lattices.

C.2 Method

Consider thus a material system discretized in mass points that interact with neighboring mass points through effective bond interaction potentials so that the total internal energy of the system reads as:

$$U = \sum_{i}^{N} U^{i}\left(\overrightarrow{r}_{i}\right) + \sum_{i,j}^{N} U^{ij}\left(\overrightarrow{r}_{ij} = \overrightarrow{r}_{j} - \overrightarrow{r}_{i}\right) + \sum_{i,j,k}^{N} U^{ijk}\left(\overrightarrow{r}_{i}, \overrightarrow{r}_{j}, \overrightarrow{r}_{k}\right) + \dots \tag{C.5}$$

Herein, $U^{i}\left(\overrightarrow{r}_{i}\right) = -\epsilon_{i}^{0}$ stands for the one-body term of the energy of mass points defined by position vector $\overrightarrow{r}_{i}$ which defines the well-depth of the interaction potential at equilibrium; $U^{ij}\left(\overrightarrow{r}_{ij} = \overrightarrow{r}_{j} - \overrightarrow{r}_{i}\right)$ describes two-body interactions between mass points i and j; U^{ijk} three-body interactions between i, j and k; and so on. The interaction potentials are assumed to carry all the relevant physics information to define the energy variations between mass points. For this system, the fracture problem is restated in the grand canonical thermodynamic Ensemble, in which the system of interest is coupled to a heat bath (at temperature T) and an infinite reservoir (at a chemical potential μ) with which it can exchange bonds (instead of particles, N). In this ensemble, both the energy (U) and number of bonds (N) fluctuate, at the specified bond potential (μ), prescribed (generalized) volume (V) (i.e. prescribed displacement) and temperature (T). In this μVT–ensemble, one would sweep the pseudo-chemical potential μ in order to obtain the number of broken bonds and its fluctuations around a minimum the grand potential realizes according to Eq. (C.4).

C.2.1 GCMC approach: Acceptance criterion

An efficient way of solving such an ensemble (i.e. determining the minimum value of Ω) is by means of grand canonical Monte Carlo Simulations, in which μ, V, T are specified. The GCMC approach thus consists of bond addition and bond deletion moves, following acceptance criteria that take into account the change of energy of the microstates; that is:

$$acc\,(o \to n) = \min\left(1, p_{o\to n}\right) \tag{C.6}$$

with:

- For an insertion move, i.e. addition of a bond $(N \to N+1)$:

$$p_{N\to N+1} = \frac{V\Lambda^{-3}}{N+1}\exp\left(\frac{1}{k_B T}\left(\mu - \Delta U_{N\to N+1}\right)\right) \tag{C.7}$$

- For a deletion move, i.e. deletion of a bond $(N \to N-1)$:

$$p_{N\to N-1} = \frac{N}{V\Lambda^{-3}}\exp\left(-\frac{1}{k_B T}\left(\mu + \Delta U_{N\to N-1}\right)\right) \tag{C.8}$$

In the above, $\Delta U_{o\to n} = U_n - U_o$ stands for the difference in total energy of microstate $k = (o, n)$ evaluated from Eq. (C.5), V for the volume of the simulation box; whereas Λ is de Broglie thermal wave length, which must be much smaller than the characteristic size of the bond length, σ_0, so that classical Newtonian mechanics applies; that is:

$$\Lambda = \frac{h}{\left(2\pi k_B T m_b\right)^{1/2}} = \left(\frac{N_0}{V}\right)^{1/2}\frac{h}{\left(2\pi T^* p^* \rho^*\right)^{1/2}} \ll \sigma_0 \tag{C.9}$$

or in reduced (MD) temperature ($T^* = k_B T/\epsilon_i^0$), pressure ($p^* = \epsilon_i^0/\sigma_0^3$) and mass density units ($\rho^* = \rho\sigma_0^3$):

$$T^* = \frac{k_b T}{\epsilon_i^0} \gg \frac{N_0\left(h/\sigma_0\right)^2}{V\left(2\pi p^* \rho^*\right)};\ p^* = \frac{\epsilon_i^0}{\sigma_0^3} \gg \frac{N_0\left(h/\sigma_0\right)^2}{V\left(2\pi T^* \rho^*\right)} \tag{C.10}$$

with $h = 6.626070040(81) \times 10^{-34}$ Js the Planck constant and $k_B = 1.38064852(79) \times$

10^{-23}J/K the Boltzmann constant, $m_b =$ mass attributed to bonds from connecting mass points; e.g. for a homogeneous material $m_b = \rho V/N_0$.

The result of such GCMC-simulations is a relationship of the form $N = N(\mu)$ and its fluctuations.

C.2.2 Bond rupture activity

It is of interest to identify some limit values of the bond energy release rate. The first, and natural one, is the limit value of $\mu \to \mu_{\lim}$ for an unloaded system at equilibrium everywhere, for which:

$$U^{ij} = U^{ijk} = 0;\ U = \sum_i^N U^i\left(\overrightarrow{r}_i\right) \tag{C.11}$$

The very nature of this asymptotic equilibrium state requires that both insertion and deletion moves are equally likely to be accepted. That is, for a homogeneous system, for which $U^i = -\epsilon_i^0$,

$$\begin{aligned} p_{N\to N+1} &= \frac{V\Lambda^{-3}}{N_0+1}\exp\left(\frac{1}{k_BT}\left(\mu_{\lim}+\epsilon_i^0\right)\right) \geq 1 && \text{(C.12a)} \\ p_{N\to N-1} &= \frac{N_0}{V\Lambda^{-3}}\exp\left(-\frac{1}{k_BT}\left(\mu_{\lim}+\epsilon_i^0\right)\right) \geq 1 && \text{(C.12b)} \end{aligned}$$

Hence:

$$\ln\left(\frac{N_0+1}{V\Lambda^{-3}}\right) \leq \frac{1}{k_BT}\left(\mu_{\lim}+\epsilon_i^0\right) \leq \ln\left(\frac{N_0}{V\Lambda^{-3}}\right) \tag{C.13}$$

Noting that $N_0 \gg 1$, the two inequalities are satisfied for a critical value:

$$\frac{\mu_{\lim}}{\epsilon_i^0} \equiv -1 + T^*\ln\left(\frac{1}{\Lambda^*}\right) \tag{C.14}$$

where:

$$\frac{1}{\Lambda^*} = \frac{N_0\Lambda^3}{V} = \left(\frac{N_0}{V}\right)^{5/2}\frac{h^3}{\left(2\pi T^*p^*\rho^*\right)^{3/2}} \ll \frac{N_0\sigma_0^3}{V} \tag{C.15}$$

The critical value derived here for the unloaded case can be associated with a complete bond rupture at a critical bond energy value $\mu_{\lim}$, which dissipates the ground state energy of the unloaded system. Using the limit case (C.14) one can restate the acceptance criteria (C.7) and (C.8) in the form:

$$p_{N\to N+1} = \frac{N_0}{N+1}\frac{1}{a}\exp\left(-\frac{1}{T^*}\left(\frac{\Delta U_{N\to N+1}}{\epsilon_i^0}+1\right)\right) \tag{C.16a}$$

$$p_{N\to N-1} = \frac{N}{N_0}a\exp\left(-\frac{1}{T^*}\left(\frac{\Delta U_{N\to N-1}}{\epsilon_i^0}-1\right)\right) \tag{C.16b}$$

where a by analogy with the chemical activity is recognized as a "bond rupture activit":

$$a = \exp\left(-\frac{1}{T^*\epsilon_i^0}\left(\mu-\mu_{\lim}\right)\right) \tag{C.17}$$

The bond rupture activity has a maximum value of $a = 1$ for $\mu = \mu_{\lim}$, in agreement of the activity of a solid body composed of a uniform, single species solid non-interacting with any of its neighbours. That is, in the terminology of physical chemistry [157], μ_{lim} defines a 'standard state' of a solid in a vaporized-type state.

C.2.3 Link with linear elastic fracture mechanics

It is instructive to seek a formal link between the GCMC fracture approach and classical Linear Elastic Fracture Mechanics (LEFM). Consider thus the initial bond–rupture state: the system is moved out of its equilibrium state through the application of a displacement loading. Close to the equilibrium state, the bond stretching response is linear in consequence of the displacement loading $\overrightarrow{\delta}$ applied at the boundary:

$$\lambda_{ij}\sigma_0 = \underline{\underline{A}}_{ij}\cdot\overrightarrow{\delta} \tag{C.18}$$

with $\underline{\underline{A}}_{ij} = \underline{\underline{A}}_{ij}\left(\overrightarrow{r}_{ij}\right)$ some (dimensionless) linear (matrix) operator corresponding each to the response of the system. Sufficiently close to equilibrium ($N/N_0 = O\left(1\right)$), the strain energy follows a harmonic potential, so that:

$$U^{ij}\left(\lambda_{ij}\right) = \frac{1}{2}\epsilon_{ij}\lambda_{ij}^2 = \frac{1}{2}\frac{\epsilon_{ij}}{\sigma_0^2}\overrightarrow{\delta}\cdot\underline{\underline{B}}^{ij}\cdot\overrightarrow{\delta};\ \underline{\underline{B}}^{ij} = \left[\left(\underline{\underline{A}}_{ij}\right)^T\cdot\underline{\underline{A}}_{ij}\right] \tag{C.19}$$

With this form in mind, we evaluate the bond energies (for a homogeneous system):

$$\frac{U_N}{\epsilon_i^0} = -N + \sum_{ij=1}^{N} \frac{U^{ij}\left(\lambda_{ij}\right)}{\epsilon_i^0} = -N + \frac{1}{2}\frac{\epsilon_{ij}}{\epsilon_i^0\sigma_0^2}\overrightarrow{\delta}\cdot\sum_{ij=1}^{N}\underline{\underline{B}}_{ij}\cdot\overrightarrow{\delta} \tag{C.20}$$

Whence the change in bond energy, when the first bond ruptures ($N_0 \rightarrow N_0 - 1$):

$$\frac{\Delta U_{N_0\rightarrow N_0-1}}{\epsilon_i^0} = \frac{U_{N_0-1} - U_{N_0}}{\epsilon_i^0} = 1 - \frac{1}{2}\frac{\epsilon_{ij}}{\epsilon_i^0\sigma_0^2}\overrightarrow{\delta}\cdot\underline{\underline{C}}_{ij}^{N_0}\cdot\overrightarrow{\delta} \tag{C.21}$$

where $\underline{\underline{C}}_{ij}^{N_0}$ can be associated with the variation of the Hessian when one bond breaks:

$$\underline{\underline{C}}_{ij}^{N_0} = \sum_{ij=1}^{N_0}\underline{\underline{B}}_{ij} - \sum_{ij=1}^{N_0-1}\underline{\underline{B}}_{ij} = \frac{\partial}{\partial N}\frac{\partial^2\left(U_{N_0}/\epsilon_i^0\right)}{\partial\left(\overrightarrow{\delta}/\sigma_0\right)^2} \tag{C.22}$$

Similarly, considering the state $N = N_0 - 1$, an insertion step ($N_0 - 1 \rightarrow N_0$) is associated with the energy change:

$$\frac{\Delta U_{N_0-1\rightarrow N_0}}{\epsilon_i^0} = \frac{U_{N_0} - U_{N_0-1}}{\epsilon_i^0} = -1 + \frac{1}{2}\frac{\epsilon_{ij}}{\epsilon_i^0\sigma_0^2}\overrightarrow{\delta}\cdot\underline{\underline{C}}_{ij}^{N_0}\cdot\overrightarrow{\delta} \tag{C.23}$$

The first bond rupture ($N_0 \rightarrow N_0 - 1$) becomes probable if – according to Eq. (C.8):

$$p_{N_0\rightarrow N_0-1} = \exp\left(\frac{1}{T^*}\left(-\frac{(\mu-\mu_{\text{lim}})}{\epsilon_i^0} + \frac{1}{2}\frac{\epsilon_{ij}}{\epsilon_i^0\sigma_0^2}\overrightarrow{\delta}\cdot\underline{\underline{C}}_{ij}^{N_0}\cdot\overrightarrow{\delta}\right)\right) > 1 \tag{C.24}$$

or equivalently, in terms of the critical bond energy release rate:

$$\frac{(\mu-\mu_{\text{lim}})}{\epsilon_i^0} < \frac{1}{2}\frac{\epsilon_{ij}}{\epsilon_i^0\sigma_0^2}\overrightarrow{\delta}\cdot\underline{\underline{C}}_{ij}^{N_0}\cdot\overrightarrow{\delta} \tag{C.25}$$

Similarly, considering the state $N = N_0 - 1$, an insertion step ($N_0 - 1 \rightarrow N_0$) becomes possible, if according to Eq. (C.7):

$$p_{N_0-1\rightarrow N_0} > 1 \Leftrightarrow \frac{\mu-\mu_{\text{lim}}}{\epsilon_i^0} > \frac{\epsilon_{ij}}{2\epsilon_i^0\sigma_0^2}\overrightarrow{\delta}\cdot\underline{\underline{C}}_{ij}^{N_0}\cdot\overrightarrow{\delta} \tag{C.26}$$

Finally, the Monte-Carlo procedure will converge to a solution for which the probability of insertion is equal to the probability of deletion; for which reason the bond energy release at the onset of the initial fracture formation will converge according to Eqn. (C.25) and (C.26) to a value of:

$$\frac{\mu - \mu_{\text{lim}}}{\epsilon_i^0} \equiv \frac{\epsilon_{ij}}{2\epsilon_i^0 \sigma_0^2} \overrightarrow{\delta} \cdot \underline{\underline{C}}_{ij}^{N_0} \cdot \overrightarrow{\delta} \tag{C.27}$$

It is worth noting that the right hand side of Eq. (C.27) together with Eq. (C.22) is almost identical to stiffness-based fracture perturbations methods used in Linear Elastic Fracture Mechanics (LEFM) for the evaluation of the energy release rate [12]. The fracture mechanics–GCMC analogy thus suggests:

$$\frac{\mu - \mu_{\text{lim}}}{\epsilon_i^0} = -\frac{\mathcal{G}}{\epsilon_i^0} \left(\frac{\partial \Gamma}{\partial N} \right) \tag{C.28}$$

where the negative sign comes from the fact that $\partial\Gamma/\partial N < 0$ (since N stands for the number of unbroken bonds). At bond rupture, $\mathcal{G} = \mathcal{G}_F$, it becomes possible to formally identify the link between fracture energy and the bond rupture potential:

$$\mu\left(N_0\right) - \mu_{\text{lim}} \equiv -\mathcal{G}_F \left(\frac{\partial \Gamma}{\partial N} \right) \tag{C.29}$$

On the other hand, in contrast to fracture mechanics, in the GCMC approach the value of the energy release rate, $\mathcal{G}$, is fixed, whereas the value of $\mu = \mu\left(N_0\right)$ –respectively the value of the fracture energy– is changed, until the probability of deletion and insertion is equal; that is:

$$N_0 \rightarrow N_0 - 1 : \frac{\mathcal{G}}{\epsilon_i^0} \left(\frac{\partial \Gamma}{\partial N} \right) + \frac{\mu - \mu_{\text{lim}}}{\epsilon_i^0} > 0 \Leftrightarrow \mathcal{G} - \mathcal{G}_F\left(N\right) > 0 \tag{C.30}$$

$$N_0 - 1 \rightarrow N_0 : \frac{\mathcal{G}}{\epsilon_i^0} \left(\frac{\partial \Gamma}{\partial N} \right) + \frac{\mu - \mu_{\text{lim}}}{\epsilon_i^0} < 0 \Leftrightarrow \mathcal{G} - \mathcal{G}_F\left(N\right) < 0 \tag{C.31}$$

Otherwise said, in sweeping with the GCMC approach possible values of $\mu\left(N\right)$ –respectively $\mathcal{G}_F\left(N\right)$– deletion is favored as long as $\mathcal{G} > \mathcal{G}_F\left(N\right)$, whereas insertion is favored if $\mathcal{G} < \mathcal{G}_F\left(N\right)$, with μ_{lim} being the smallest possible value of the critical bond energy, $\mu(N) \in \,]\mu_{\lim}; 0[$.

C.2.4 Bond rupture fluctuations, compressibility, damage and heat of bond Rupture

There is, however, a fundamental difference between the fracture mechanics approach and the GCMC approach, which relates to fluctuations; that is, for a given value of μ, there exists a number of $k-$ configurations associated with bond fracture. Otherwise said, there is not a single deterministic bond breakage, but a number of possible bonds that can break, at the same value of μ. At a given chemical potential μ, let $\langle N_k \rangle$ the average number of bonds in the system; whereas the fluctuations are characterized by the variance $\mathrm{Var}(N_k) = \langle N_k^2 \rangle - \langle N_k \rangle^2$. The variance relates to the slope of the $\langle N_k \rangle - \mu$ –curve by:

$$\mathrm{Var}(N_k) = \left\langle N_k^2 \right\rangle - \langle N_k \rangle^2 = T^* \left(\frac{\partial \langle N_k \rangle}{\partial (\mu/\epsilon_i^0)} \right)_{VT} \tag{C.32}$$

Whereas the slop relates to the bond compressibility κ_T of the system by:

$$\kappa_T = \frac{V}{\epsilon_i^0 \langle N_k \rangle^2} \left(\frac{\partial \langle N_k \rangle}{\partial (\mu/\epsilon_i^0)} \right)_{VT} = \frac{\kappa_0}{\langle N_k \rangle} \left(\left\langle N_k^2 \right\rangle - \langle N_k \rangle^2 \right) \tag{C.33}$$

where $\kappa_0 = V/(k_B T \langle N_k \rangle) = V/(T^* \epsilon_i^0 \langle N_k \rangle)$ can be considered as a compressibility factor of the ideal gas. Before the first bond ruptures, $\langle N_k \rangle = N_0$, and the slope is $\lim_{N_0} (\partial \langle N_k \rangle / \partial \mu) \to 0$; meaning that the system is infinitely rigid ($\kappa_T \to 0$).In return, when $\mu \to \mu_{\lim}$, the slope is $\lim_{\mu \to \mu_{\lim}} (\partial \langle N_k \rangle / \partial \mu) \to \infty$, which means that the system is infinitely compressible ($\kappa_T \to \infty$); much as a gas. Thus, the compressibility which is but a reflection of fluctuations can be used to describe the damage accumulation from a state of incompressibility to a state of infinite compressibility w.r.t. fracture. In fact, consider damage variable $D \in [0, 1]$, with $D = 0$ corresponding to the initial state ($\kappa_T \to 0$), and $D = 1$ to the complete broken state ($\kappa_T \to \infty$). The damage variable can thus be defined in terms of bond fluctuations as:

$$D = \frac{\langle N_k \rangle \kappa_T / \kappa_0}{1 + \langle N_k \rangle \kappa_T / \kappa_0} = \frac{\langle N_k^2 \rangle - \langle N_k \rangle^2}{1 + \langle N_k^2 \rangle - \langle N_k \rangle^2} \tag{C.34}$$

That is, the initial state corresponds to the absence of fluctuations; whereas the complete damage state is an asymptotic state, where fluctuations dominate, $\langle N_k^2 \rangle - \langle N_k \rangle^2 \gg 1$.

Another quantity of interest relating to fluctuations is the change in average internal energy, $\langle U_k \rangle$, between two systems that differ only by the average number of bonds. The definition follows closely the one employed to computing the heat of adsorption in the grand canonical ensemble, for which the heat (measurable by e.g. calorimetry) relates to the differential change in the internal energy by (see [105], and application in [106]):

$$q = -\frac{\partial \langle U_k \rangle}{\partial \langle N_k \rangle} = -\frac{\langle N_k U_k \rangle - \langle N_k \rangle \langle U_k \rangle}{\langle N_k^2 \rangle - \langle N_k \rangle^2} \tag{C.35}$$

where U_k stands for the internal energy associated with realization N_k at a given chemical potential μ. Following Eq. (C.5), it is useful to break the energy fluctuations down in two terms, one related to the groundstate energy, the other to the strain energy activated between mass points; i.e. $U_k = U_k^i + U_k^{ij} + ...$; hence,

$$q = -\frac{\partial \langle U_k^i \rangle}{\partial \langle N_k \rangle} - \frac{\partial \langle U_k^{ij} \rangle}{\partial \langle N_k \rangle} = -\frac{\langle N_k U_k^i \rangle - \langle N_k \rangle \langle U_k^i \rangle}{\langle N_k^2 \rangle - \langle N_k \rangle^2} - \frac{\langle N_k U_k^{ij} \rangle - \langle N_k \rangle \langle U_k^{ij} \rangle}{\langle N_k^2 \rangle - \langle N_k \rangle^2} \tag{C.36}$$

where U_k^i and U_k^{ij} stand respectively for the groundstate energy and deformation energy of the k^{th} realization. The two terms on the r.h.s. of Eq. (C.36) represent respectively; the heat release associated with the energy release of the groundstate energy (noting that $U_k^i < 0$); and the heat release due to inter-mass point strain energy variation (noting that $U_k^{ij} \geq 0$). In the limit case, when the strain energy is exhausted, that is $\partial \langle U_k^{ij} \rangle / \partial \langle N_k \rangle = 0$ and $U_k^{ij} = 0$ [which corresponds strictly to the definition of the critical chemical potential defined by Eq. (C.14)], the heat released due to the complete dissipation of the ground state energy – in the absence of any deformation of the system is:

$$q\left(\mu \rightarrow \mu_{\lim}\right) = -\frac{\partial \left\langle U_k^i \right\rangle}{\partial \left\langle N_k \right\rangle} = -\frac{\left\langle N_k U_k^i \right\rangle - \left\langle N_k \right\rangle \left\langle U_k^i \right\rangle}{\left\langle N_k^2 \right\rangle - \left\langle N_k \right\rangle^2} \tag{C.37}$$

In the case of a homogeneous material, for which $U_k^i = -N_k \epsilon_i^0$, this ultimate energy dissipation is $q\left(\mu \rightarrow \mu_{\lim}\right) = \epsilon_i^0$. On the other hand, the second term on the r.h.s. of Eq. (C.36) represents the heat associated with the change in strain energy due to bond insertion or removal; a strain energy which results from the application of mechanical work to the system (generalized volume change, i.e. displacement, maintained constant in the μVT-ensemble). Thus, for values $\mu \in]\mu_{N_0-1}, \mu_{\lim}[$, there exists a second –intermediate– critical value of the chemical potential for which the change in internal energy due to bond insertion or deletion is equal to the ground-state energy:

$$q\left(\mu \rightarrow \mu_{crit}\right) = -\frac{\partial}{\partial \left\langle N_k \right\rangle}\left(\left\langle U_k^{ij} \right\rangle + \left\langle U_k^i \right\rangle\right) = 0 \tag{C.38}$$

or, equivalently in terms of fluctuations, for a homogeneous system:

$$q\left(\mu \rightarrow \mu_{crit}\right) = 0;\ \frac{\partial \left\langle U_k^{ij} \right\rangle}{\partial \left\langle N_k \right\rangle} = \frac{\left\langle n_k U_k^{ij} \right\rangle - \left\langle n_k \right\rangle \left\langle U_k^{ij} \right\rangle}{\left\langle n_k^2 \right\rangle - \left\langle n_k \right\rangle^2} = \epsilon_i^0 \tag{C.39}$$

This 'heat balance' condition between elastic and groundstate energy that defines the critical state (C.38) can be viewed as the statistical physics counterpart of Griffith's fracture propagation criterion (C.1), which thus permits to make a handshake between the classical continuum formulation of fracture mechanics and the statistical physics of fluctuations. In this handshake, the quantity $\partial \left\langle U_k^{ij} \right\rangle / \partial \left\langle N_k \right\rangle$ can be viewed as the elastic bond energy release rate, whereas the quantity $-\partial \left\langle U_k^i \right\rangle / \partial \left\langle N_k \right\rangle$ as the critical bond energy release rate defined by Eqn. (C.38), (C.37) and (C.39).

C.3 Application

The focus of this application is to give proof of the concept that the GCMC method thus proposed is an alternative to classical load–driven fracture mechanics. For this purpose, we consider the simplest discrete representation of a material domain, a regular two-dimensional lattice. Borrowing from recent developments of the Lattice Element Method (LEM), we employ the potential-of-mean-force (PMF) approach to describe interactions between lattice sites ([19, 70]). This approach has been shown to coincide in the linear elastic regime with the classical LEM formulation that uses truss and beam elements to propagate mechanical information from lattice site to lattice site (for state-of-the-art, see e.g. [158]). In return, the PFM-approach has the advantage that it permits a handshake with statistical physics-based interaction potentials, which are explicitly required in the proposed GCMC approach. It should, however, be noted that the GCMC approach is not restricted to lattice-type representations, but should hold for any discrete simulation approach that explicitly defines energy states in the material by means of bonded interaction potentials.

C.3.1 Simulation samples

We consider regular two-dimensional lattices of size σ_0 with lattice sites connected by 8 bonds to neighboring lattice sites. The interactions between mass points are described by harmonic potentials, of the form (C.19); i.e. $U^i + U^{ij} = -\epsilon_i^0 + \frac{1}{2}\epsilon_{ij}\lambda_{ij}^2$ with $U^i(\overrightarrow{r}_i) = -\epsilon_0^i$ the groundstate energy (well depth), and ϵ^{ij} the energy activated by the stretch $\lambda_{ij} = 1/||\overrightarrow{r}_{ij}^0||(\overrightarrow{r}_{ij} - \overrightarrow{r}_{ij}^0) \cdot \overrightarrow{e}_n^{ij}$ in the link direction $\overrightarrow{e}_n^{ij} = \overrightarrow{r}_{ij}/||\overrightarrow{r}_{ij}||$. The material considered is homogeneous and isotropic (Young's modulus E, Poisson's ratio ν) one with a notch, the other without a notch (Fig. C-1), which owing to the limit of a two-dimensional lattice with only 2-body interactions (i.e. $\nu = 1/3$; see e.g. [70]) ϵ_{ij} is related to the Young's modulus E and the third-dimension thickness d by $\epsilon_{ij} \simeq (3/4)\, E\sigma_0^2 d$ for both straight and diagonal links; hence in a dimensionless form:

$$\frac{U^i + U^{ij}}{\epsilon_i^0} = -1 + \frac{1}{2}\chi\lambda_{ij}^2; \chi = \frac{\epsilon_{ij}}{\epsilon_i^0} = \frac{3}{4}\frac{E\sigma_0^2 d}{\epsilon_i^0} \tag{C.40}$$

The critical local stretch is thus $\lambda_c = \sqrt{2/\chi}$, for which $U^i + U^{ij} = 0$. In the simulations, we consider $\chi = 115.45$ (hence, $\lambda_c = 0.131$), a temperature (in reduced units) $T^* = k_B T/\epsilon_i^0 = 0.1$, which satisfies Eq. (C.10). Unnotched and notched systems are investigated (Fig. C-1a-c), corresponding to critical values of the bond potential according to Eqs. (C.14) and (C.38) of $\mu_{\lim}/\epsilon_i^0 = -26.7241$; and $\mu_{crit}/\epsilon_i^0 = \mu_{\lim}/\epsilon_i^0 + 1 = -25.7241$. In the simulations, we consider periodic boundary conditions, so that lateral displacements are zero, whereas vertical displacements on opposite sides are prescribed $\delta = \pm u^d/2$, so that the prescribed volume of the system is $V = V_0\left(1+\overline{\lambda}\right)$, with $\overline{\lambda} = u^d/L_y$ the average stretch in the vertical direction. Different initial stretch magnitudes $\overline{\lambda}/\lambda_c$ are prescribed ranging from $\overline{\lambda}/\lambda_c = 0$ to $\overline{\lambda}/\lambda_c = 4/3$.

C.3.2 Results

Bond isotherms

Typical results obtained from the GCMC simulations are shown in Figure C-1 in form of bond potential – average number of bonds relationship; plots which can be aptly called –by analogy with adsorption processes– "bond isotherms", $\langle N_k\rangle - \mu$. As a reminder, in the GCMC simulations, μ is prescribed (together with the volume and the temperature), and the average number of bonds $\langle N_k\rangle$ corresponds to the average of k distinct configurations, for which –on average– the probability of insertion is equal to the probability of deletion. Specifically, three systems are investigated (Fig. C-1a-c), an unnotched and a notched specimen subject to a volume change $\overline{\lambda}$ close to the critical local stretch $\overline{\lambda}/\lambda_c \approx 1$, and a broken system, for which the strain energy stored in the bonds is zero. Despite different starting points (related to the initial number of bonds), it is remarkable that the systems (notched and unnotched) subject to similar volume changes converge to a characteristic curve all the way to the limit bond potential $\mu_{\lim}$ for which all strain energy has been dissipated. The fact that the slope between the two systems is similar can be understood from Eq. (C.32): two systems loaded close to the fracture limit, exhibit same fluctuations; with the fluctuations being a hallmark of the energy-driven bond rupture mechanisms. In contrast, the broken system (or any unloaded system) exhibits very small bond fluctuations until it reaches the limit bond potential $\mu_{\lim}$, where it follows the same evolution as the loaded system, when the strain energy capacity of the system is exhausted. Finally, at the limit bond value all three systems have about the same number of broken bonds (inlet of Fig. C-1), meaning that the directional bias introduced by the displacement loading of the notched and unnotched specimen converge toward roughly the same number of broken bonds when the strain energy is exhausted.

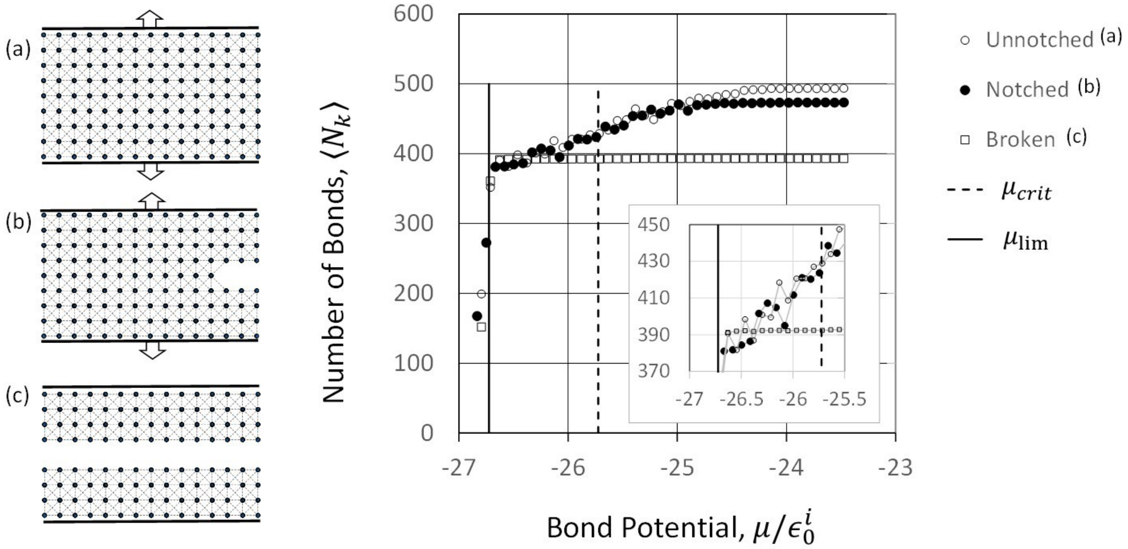

Figure C-1: Bond-Isotherms $\langle N_k \rangle - \mu$ for three systems: (a) unnotched; (b) notched; (c) broken. The unnotched and notched system are loaded close to the critical local stretch of the system, $\overline{\lambda}/\lambda_c \approx 1$. The inlet shows a magnification of the bond-isotherms around the limit bond potential $\mu_{\mathrm{lim}}/\epsilon_i^0$ corresponding to a system for which the strain energy of the system is zero.

One could inquire about fracture initiation in the GCMC method, specifically in the un-notched case, and whether the failure is localized or diffuse. In the homogeneous case, bond deletion starts in a diffuse (almost random) way, at high values of the bond rupture potential. As the bond rupture potential approaches the critical value, these diffuse events (which we sample through the MC approach) coalesce into some connected fractures. It should, however, be noted that there is no fracture path history in the GCMC approach. That is, for each value of the bond rupture potential, the GCMC simulations start with the same intact sample loaded with a constant displacement. The coalescence of bond rupture events in the GCMC approach only relates to (1) the value of the bond rupture potential; and (2) the displacement loading which introduces a preferred direction for individual bond rupture events to occur.

Damage evolution due to fluctuations

Figures C-2(a,b) display the damage evolution in function of the bond potential for different prescribed stretch ratios, $\overline{\lambda}/\lambda_c$, for both the unnotched and the notched systems. In light of the damage definition (C.34), it is remarkable to note that the unloaded system permit – via the damage evolution – an identification of the critical bond potential μ_{crit} and $\mu_{\lim}$ based only on bond fluctuations. In fact, the damage curves in C-2(a,b) for the unloaded system ($\overline{\lambda}/\lambda_c = 0$) exhibit two jumps, one at $\mu \to \mu_{crit}$, another at $\mu \to \mu_{\lim}$. At $\mu \to \mu_{crit}$, damage jumps from $D = 0$ to $D = 1/2$, corresponding thus, according to Eq. (C.34), to a finite bond compressibility of $\kappa_T \left(\mu \to \mu_{crit}\right) = \kappa_0 / \left\langle N_k \right\rangle$. At $\mu \to \mu_{\lim}$, a second jump occurs from $D = 1/2$ to $D = 1$ corresponding thus to an infinite bond compressibility$\kappa_T \left(\mu \to \mu_{\lim}\right) \to 0$ associated with large fluctuations, much akin to a gas. In return, when loaded ($\overline{\lambda}/\lambda_c > 0$), the fluctuation–driven damage entails earlier damage accumulation at values of $\mu > \mu_{crit}$. The damage evolution are s-shaped and reach the fully damaged state (dominated by fluctuations) well before the limit state, $\mu \to \mu_{\lim}$, and the higher the initial load the earlier the fully damaged state is reached (i.e. shift to the right in Fig.C-2a,b).

Energy dissipation due to fluctuations

Figures C-3(a,b) display the “ heat balance” components, in function of the prescribed bond potential, for both the unnotched and the notched system close to the critical stretch; together with the evolution of the total internal energy (groundstate energy and strain energy). Determined from Eqn. (C.35) and (C.36) based upon both energy and bond fluctuations, the results show a decrease of the heat associated with strain energy, $q_{br}^{ij} < 0$, while the heat associated with ground state energy dissipation is constant, $q_{br}^{0} = \epsilon_i^0$; a hallmark of the homogeneity of the considered material system. Remarkably, yet as predicted from the theory, when $q_{br}^0 + q_{br}^{ij} = 0$, the system reaches its maximum dissipation capacity at $\mu \to \mu_{crit}$; below which (i.e. $\mu \in]\mu_{crit}, \mu_{\lim}[$) the total energy is (almost) constant (i.e. $\partial U / \partial \mu \to 0$). This means that any lowering of the prescribed bond potential as an external field does not change –on average– the internal energy, — a clear hallmark of a metastable state. While such metastable states are accessible to the GCMC method (in contrast to unstable states), they are associated with an uncontrolled bond rupture process, defining but the subsequent localized strain energy dissipations available in the system.

Thermodynamic integration and ergodicity

The premise of the GCMC approach is that by means of equilibrium-based minimization, it is possible to assess the actual fracture resistance of materials systems; much in the vein of Griffith's stationarity principle, and postulate. This postulate merits hypothesis testing. That is, the GCMC approach herein developed is –on average– equivalent to the classical fracture mechanics testing of materials, which consists of increasing the load (here the displacement) up to a critical value at which the elastic energy put into the system, is dissipated in the creation of fracture surface. In the GCMC approach, the change in energy between the initial state and the broken state is provided by an integration of the bond isotherms in the form:

$$U_{\mathrm{lim}} - U_0 = \int_{N_{\mathrm{lim}}}^{N_0\left(\overline{\lambda}\right)} \left(\mu - \mu_{\mathrm{lim}}\right)\ d\left\langle N_k \right\rangle \tag{C.41}$$

where $N_0\left(\overline{\lambda}\right)$ is the number of initial bonds at a given displacement loading defined by $\overline{\lambda}$. Figure C-4a,b plots the bond isotherms in a form $\langle N_k \rangle$ vs. $\left(\mu - \mu_{\mathrm{lim}}\right)/\epsilon_i^0$ for different prescribed stretch ratios, $\overline{\lambda}/\lambda_c$, for both the unnotched and the notched system. The energy integral (C.41) shown in Fig. C-4c follows a convex quadratic development with the prescribed displacement; up to a maximum value beyond which the energy converges, for both samples, to the same value of $\left(U_{\mathrm{lim}} - U_0\right)/\epsilon_i^0 \simeq 140$. This value corresponds (almost) exactly to the number of broken bonds $N_0 - N_{\mathrm{lim}}$ shown in the bond isotherms in Figures C-4a,b. This means that this maximum value provided by energy integration provides, for the homogeneous system, a means to assess the number of broken bonds that release energy in the course of a loading process. In fact, since $U_{\mathrm{lim}} = -N_{\mathrm{lim}}\epsilon_i^0$ and $U_0 = -N_0\epsilon_i^0 + U^{ij}\left(\overline{\lambda}\right)$, at the limit when the strain energy is exhausted ($U^{ij}=0$), the maximum energy that can be dissipated is $\lim_{U^{ij}\to 0}\left(U_{\text{lim}}-U_0\right)=\left(N_0-N_{\text{lim}}\right)\epsilon_i^0$. Up to this limit value, the thermodynamic integration of the bond isotherms provides a means to assess the (elastic) bond deformation behavior, since $U_{\text{lim}}-U_0=\left(N_0-N_{\text{lim}}\right)\epsilon_i^0-U^{ij}\left(\overline{\lambda}\right)$. Thus, for $\overline{\lambda}-$ values smaller than the limit value, a derivative of the energy curve provides a means to assess the (reaction) force–displacement relation of the sample in the displacement driven test; from:

$$R=-\frac{\partial\left(U_{\text{lim}}-U_0\right)}{\partial u^d}=\frac{1}{L_y}\frac{\partial U^{ij}\left(\overline{\lambda}\right)}{\partial\overline{\lambda}} \tag{C.42}$$

Figure C-4d plots this force-displacement relation in a dimensionless form; confirming for the harmonic case a linear behavior up to the limit value, and a drop thereafter. This shows that the GCMC–approach is able to predict classical force–displacement relations by mere thermodynamic integration of the bond isotherms. This is strong evidence that the GCMC-approach satisfies the ergodic hypothesis of statistical physics (see e.g. [159]); that is, the equivalence of the "long-term time average", i.e. static force-displacement response (obtained in classical "quasi-static" fracture mechanics by means of displacement-driven tests), and the statistical-equilibrium ensemble average (obtained here by means of thermodynamic integration of the GCMC bond isotherms).

Finally, for a homogeneous material, the thermodynamic integration of the bond isotherms may also provide an indirect means to determine the bond energy parameters, and specifically the ground state energy ϵ_i^0. In fact, the maximum force (or macroscopic stress) scales as $\max R\sim\epsilon_i^0\left(\epsilon_i^0/\epsilon_{ij}\right)^{1/2}$. Since ϵ_{ij} is a mere function of the elasticity of the material (see [70]), the scaling of the maximum force (or stress) could be used for calibration.

C.4 Concluding remarks

It has thus been shown that a GCMC-approach to Fracture Mechanics provides an attractive alternative to assess the fracture resistance of solids, particular if the solid's energy state is represented in a discrete way, by means of two-body and three-body interactions. The following points deserve attention:

1. If fracture processes are considered as a sequence of constrained equilibrium states (which is the definition since Griffith [1] of a quasi-static fracture problem [73]), with each state representing an energy minimum, a restatement of the fracture mechanics problem in the grand canonical thermodynamic ensemble provides a means to determine the associated bond ruptures and their fluctuations. This is achieved by introducing an auxiliary external field, the bond rupture potential μ, in addition to the other external constraints that define the μVT-ensemble, namely the volume (generalized displacement) and the temperature. Otherwise said, out-of-equilibrium conditions such as the one relevant for e.g. dynamic fracture propagation cannot be addressed with the equilibrium-based GCMC framework.

2. The results of the GCMC-approach are summarized in terms of bond isotherms ($\langle N_k \rangle - \mu$) that depend on the prescribed (generalized) volume (i.e. displacement boundary conditions) and the prescribed temperature; as well as on the interaction potentials. These bond isotherms carry critical information for fracture analysis; but appear to be insensitive to the presence and location of pre-existing notches, cracks etc., as required in classical fracture mechanics. Specifically, the slope of the bond isotherms just reflects bond fluctuations, permitting the definition of a fluctuation-based damage variable -as an output, rather than input. For a homogeneous material, it is shown that such a fluctuation-based damage definition permits the determination of two critical bond rupture potentials; one (μ_{crit}) associated with the maximum dissipation capacity (when strain energy fluctuations equal groundstate energy fluctuations); the other (μ_{lim}) with the limit case when all strain energy of the system is exhausted. The difference between the two, $\mu_{lim} - \mu crit$, defines the fracture resistance of the material.

3. A second critical output of the GCMC method is a means to effectively track energy fluctuations in terms of heat; and specifically the competition in energy fluctuations between the redistribution of strain energy induced by bond rup-

ture, and the dissipation of the groundstate energy. A bond rupture process is suggested to be stable as long as the sum of both is smaller than zero; while it is metastable when the sum is greater than zero (noting that MC-methods –in contrast to MD-approaches– cannot assess unstable states).

4. It can be (and has been) argued that the discrete nature of the GCMC approach may entail fracture path and discretization dependency of the results, as known from classical load-driven discrete fracture simulation techniques. While fracture path dependency can be excluded by the very nature of the GCMC approach based on energy acceptance criteria (see e.g. [68]), discretization effects should not affect the evaluation of the fracture resistance, defined by the fluctuation-based change in the internal energy (i.e. Eq. (C.36)). In fact, while a change in discretization will change the numbers of initial bonds, and thus the bond isotherms, a fine enough discretization will ensure a representative statistical sampling of different configurations to evaluate the fracture resistance from associated energy fluctuations.

5. The thermodynamic integration of the bond isotherms provides a means to make an explicit handshake between classical force displacement relations and the GCMC-approach. At least for the elastic domain, this handshake provides evidence that the proposed approach satisfies the ergodic hypothesis of statistical physics. Derived here for harmonic potentials of a regular lattice, it is found that the maximum force (or macroscopic stress) scales as $\max R \sim \epsilon_i^0 \left(\epsilon_i^0/\epsilon_{ij}\right)^{1/2}$. That is, given the elasticity scaling, $\epsilon_{ij} \sim E$, a stiffer material is expected to have a lower maximum force unless the increase of elasticity is compensated by groundstate energy.

6. For proof of concept of the GCMC method, a simple, regular two-dimensional lattice with harmonic potentials was considered; and some of the results need to be understood within the limitations of this elementary two-dimensional model. For instance, the integration of the bond isotherms to obtain energy curves show a kink in the energy evolution at the critical displacement corresponding to the

maximum fracture energy (Fig. C-4c). Such a kink can be associated with what is called in statistical physics a second-order phase transition. Such phase transition phenomena are known to be affected both by the dimension of the problem and the type of interactions. Ongoing research aims at clarifying this point, whether the method thus proposed is able to accommodate in three-dimensional heterogeneities at both the bond scale (variability of groundstate energy, elasticity, non-harmonic potentials etc.), and the sample scale (geometric heterogeneities due to texture, multiphase materials, interfaces etc.).

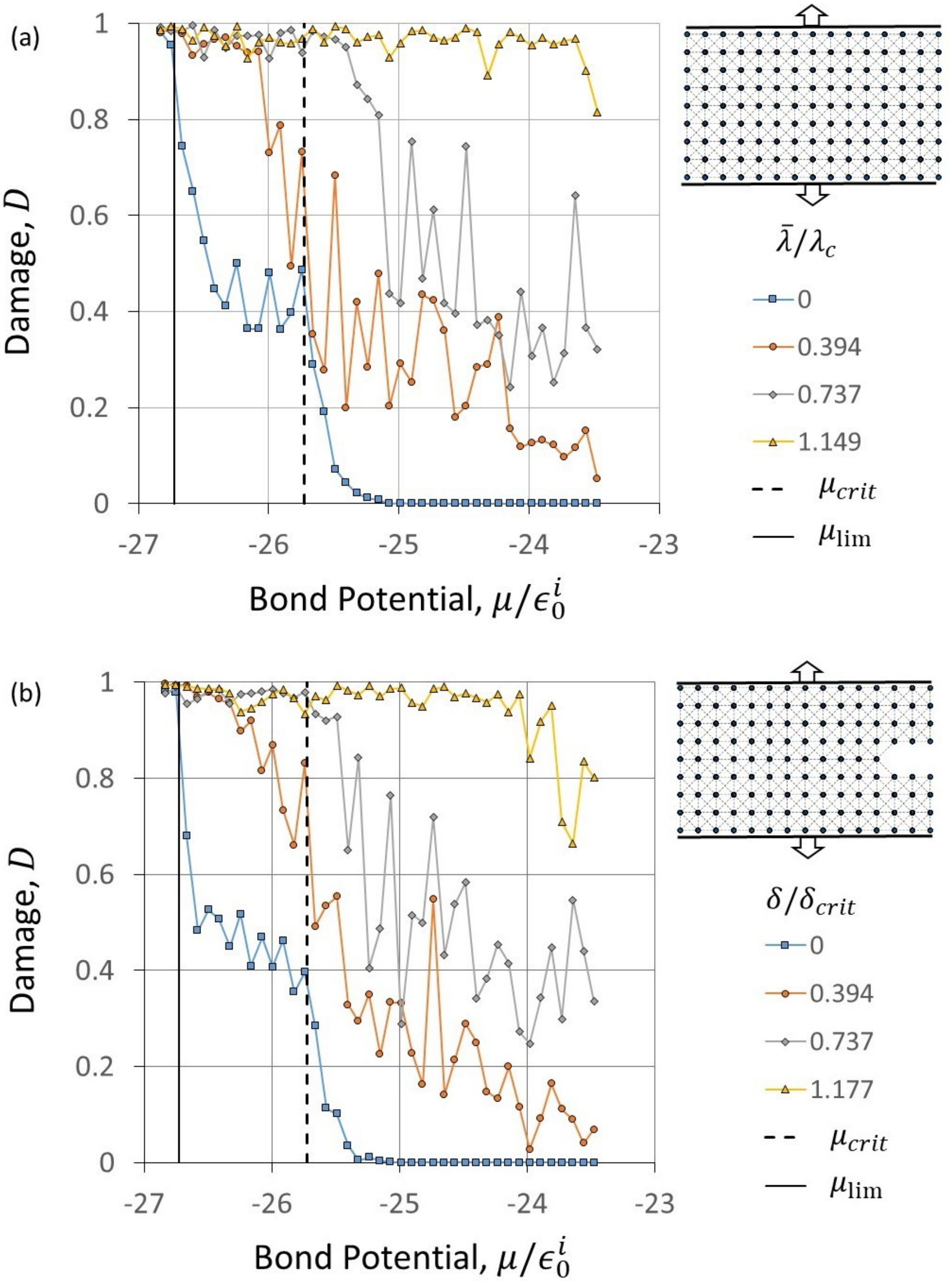

Figure C-2: Fluctuation-based damage in function of the prescribed bond rupture potential, for (a) the unnotched sample, and (b) the notched sample; and different stretch levels (with λ_c the critical stretch at which the bond potential is zero)

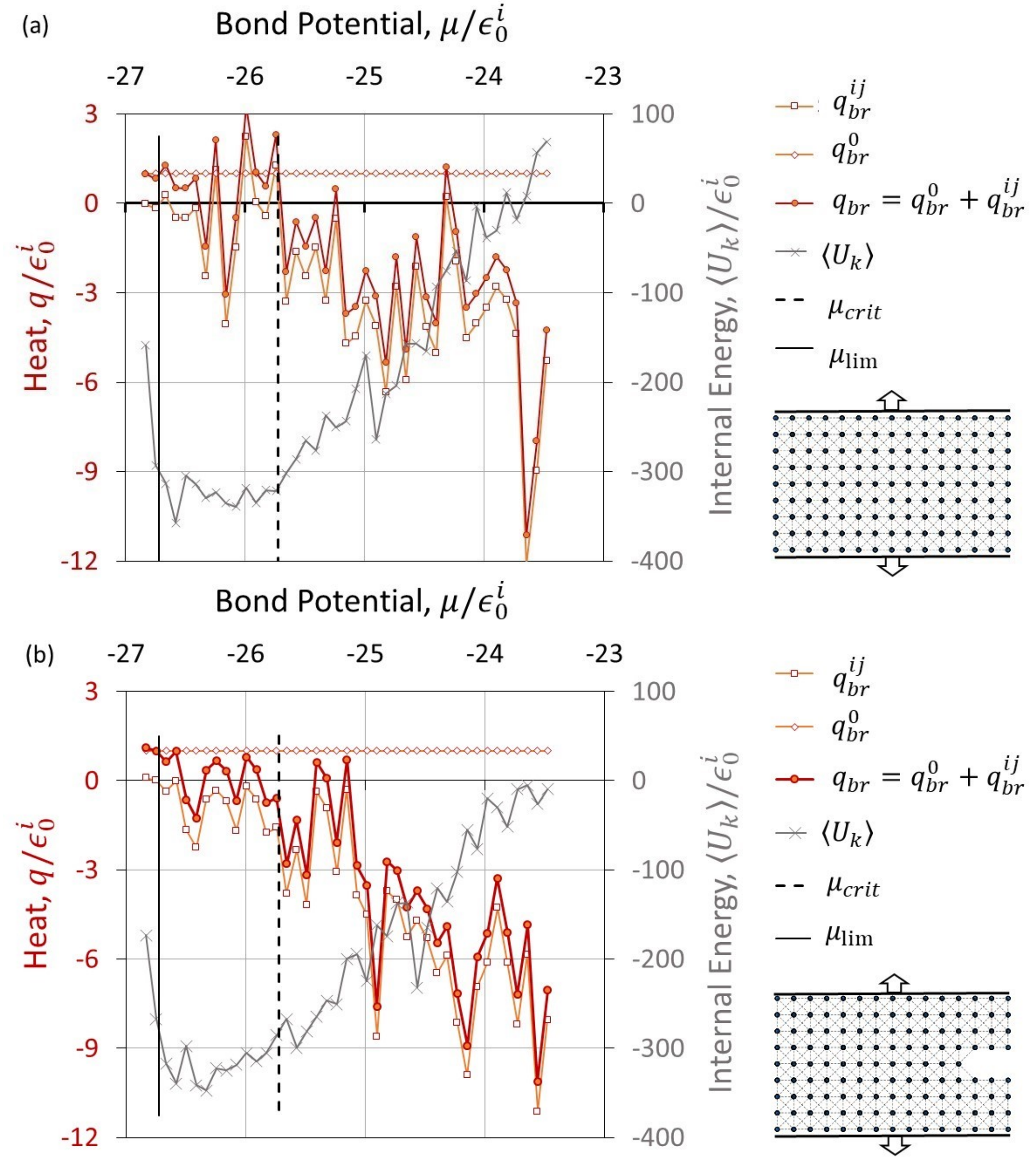

Figure C-3: Energy Dissipation due to Fluctuations for (a) the unnotched and (b) the notched sample loaded to respectively $\overline{\lambda}/\lambda_c = 1.15$ and $\overline{\lambda}/\lambda_c = 1.18$. Herein, q_{br}^{ij} and q_{br}^{0} stand for the heat associatd with respectively strain energy fluctuations and ground state energy fluctuations ($q_{br}^{0} = \epsilon_i^0$ for the homogeneous system).

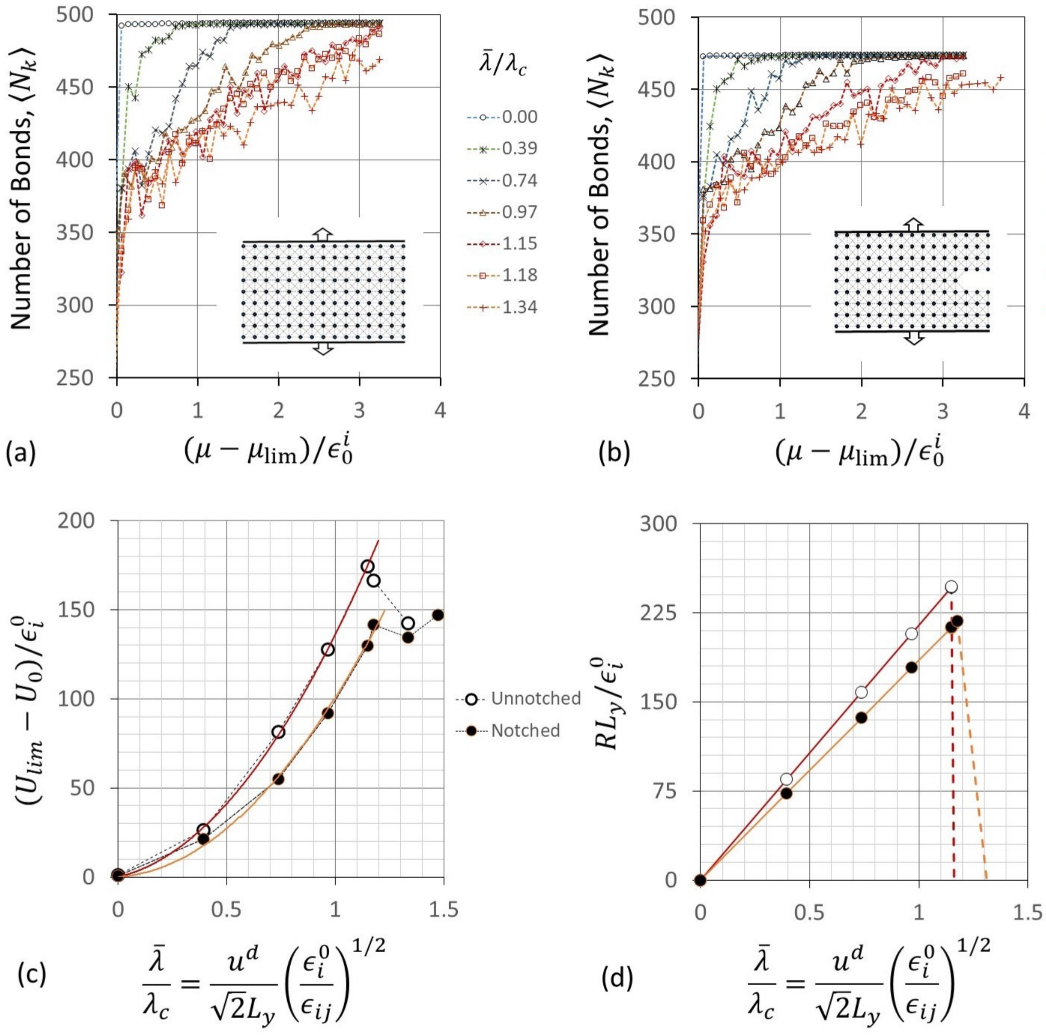

Figure C-4: Thermodynamic integration of the bond isotherms of (a) an unnotched sample; and (b) a notched sample for different stretch magnitudes, $\overline{\lambda}/\lambda_c$. (c) Resulting change in internal energy $U_{\text{lim}} - U_0 = \int_{N_{\text{lim}}}^{N_0(\overline{\lambda})} (\mu - \mu_{\text{lim}})\ d\langle N_k \rangle$, and (d) derived (dimensionless) force–displacement relation for a homogeneous system described by harmonic interactions.

Bibliography

[1] A. A. Griffith, "VI. The phenomena of rupture and flow in solids," *Philosophical Transactions of the Royal Society of London. Series A, Containing Papers of a Mathematical or Physical Character*, vol. 221, no. 582-593, pp. 163–198, 1921.

[2] T. L. Anderson, *Fracture Mechanics: Fundamentals and Applications.* CRC press, 2017.

[3] A. Kanvinde, "Predicting fracture in civil engineering steel structures: State of the art," *Journal of Structural Engineering*, vol. 143, no. 3, p. 03116001, 2017.

[4] G. R. Irwin and J. A. Kies, "Critical energy rate analysis of fracture strength," *Welding Research Supplement*, vol. 33, pp. 193–198, 1954.

[5] G. R. Irwin, "Analysis of stresses and strains near the end of a crack in an elastic solid," *Journal of Applied Mechanics*, vol. 24, pp. 361–364, 1957.

[6] E. Orowan, "Fracture and strength of solids," *Reports on Progress in Physics*, vol. 12, no. 1, p. 185, 1949.

[7] C. E. Inglis, "Stresses in a plate due to the presence of cracks and sharp corners," *Trans. Inst. Naval Archit.*, vol. 55, pp. 219–241, 1913.

[8] G. I. Barenblatt, "The mathematical theory of equilibrium cracks in brittle fracture," in *Advances in Applied Mechanics*, vol. 7, pp. 55–129, Elsevier, 1962.

[9] G. Cherepanov, "The propagation of cracks in a continuous medium," *Journal of Applied Mathematics and Mechanics*, vol. 31, no. 3, pp. 503–512, 1967.

[10] J. R. Rice, "A path independent integral and the approximate analysis of strain concentration by notches and cracks," *Journal of Applied Mechanics*, vol. 35, pp. 379–386, 06 1968.

[11] T. Shimada, K. Ouchi, Y. Chihara, and T. Kitamura, "Breakdown of continuum fracture mechanics at the nanoscale," *Scientific Reports*, vol. 5, p. 8596, 2015.

[12] D. M. Parks, "A stiffness derivative finite element technique for determination of crack tip stress intensity factors," *International Journal of Fracture*, vol. 10, no. 4, pp. 487–502, 1974.

[13] A. Hillerborg, M. Modéer, and P.-E. Petersson, “Analysis of crack formation and crack growth in concrete by means of fracture mechanics and finite elements,” *Cement and Concrete Research*, vol. 6, no. 6, pp. 773–781, 1976.

[14] Z. P. Bažant and L. Cedolin, “Fracture mechanics of reinforced concrete,” *Journal of the Engineering Mechanics Division*, vol. 106, no. 6, pp. 1287–1306, 1980.

[15] S. Vasic, I. Smith, and E. Landis, “Finite element techniques and models for wood fracture mechanics,” *Wood Science and Technology*, vol. 39, no. 1, pp. 3–17, 2005.

[16] F. F. Abraham, D. Brodbeck, W. E. Rudge, and X. Xu, “A molecular dynamics investigation of rapid fracture mechanics,” *Journal of the Mechanics and Physics of Solids*, vol. 45, no. 9, pp. 1595–1619, 1997.

[17] L. Brochard, G. Hantal, H. Laubie, F.-J. Ulm, and R. J. Pellenq, “Capturing material toughness by molecular simulation: accounting for large yielding effects and limits,” *International Journal of Fracture*, vol. 194, no. 2, pp. 149–167, 2015.

[18] E. Schlangen and J. Van Mier, “Simple lattice model for numerical simulation of fracture of concrete materials and structures,” *Materials and Structures*, vol. 25, no. 9, pp. 534–542, 1992.

[19] H. Laubie, F. Radjai, R. Pellenq, and F.-J. Ulm, “A potential-of-mean-force approach for fracture mechanics of heterogeneous materials using the lattice element method,” *Journal of the Mechanics and Physics of Solids*, vol. 105, pp. 116–130, 2017.

[20] Z. Pan, R. Ma, D. Wang, and A. Chen, “A review of lattice type model in fracture mechanics: theory, applications, and perspectives,” *Engineering Fracture Mechanics*, vol. 190, pp. 382–409, 2018.

[21] N. Abid, M. Mirkhalaf, and F. Barthelat, “Discrete-element modeling of nacre-like materials: Effects of random microstructures on strain localization and mechanical performance,” *Journal of the Mechanics and Physics of Solids*, vol. 112, pp. 385–402, 2018.

[22] P. Klein and H. Gao, “Crack nucleation and growth as strain localization in a virtual-bond continuum,” *Engineering Fracture Mechanics*, vol. 61, no. 1, pp. 21–48, 1998.

[23] J. Oliver, A. E. Huespe, and I. Dias, “Strain localization, strong discontinuities and material fracture: Matches and mismatches,” *Computer Methods in Applied Mechanics and Engineering*, vol. 241, pp. 323–336, 2012.

[24] Z. P. Bažant and S.-D. Pang, “Activation energy based extreme value statistics and size effect in brittle and quasibrittle fracture,” *Journal of the Mechanics and Physics of Solids*, vol. 55, no. 1, pp. 91–131, 2007.

[25] Z. Bertalan, A. Shekhawat, J. P. Sethna, and S. Zapperi, "Fracture strength: Stress concentration, extreme value statistics, and the fate of the Weibull distribution," *Physical Review Applied*, vol. 2, no. 3, p. 034008, 2014.

[26] E. Castillo, *Extreme Value Theory in Engineering.* Statistical Modeling and Decision Science, Elsevier Science, 2012.

[27] M. J. Alava, P. K. Nukala, and S. Zapperi, "Statistical models of fracture," *Advances in Physics*, vol. 55, no. 3-4, pp. 349–476, 2006.

[28] S. Biswas, P. Ray, and B. K. Chakrabarti, *Statistical Physics of Fracture, Breakdown, and Earthquake: Effects of Disorder and Heterogeneity.* John Wiley & Sons, 2015.

[29] S. Biswas, L. Goehring, and B. K. Chakrabarti, "Statistical physics of fracture and earthquakes," *Philosophical Transactions of the Royal Society A: Mathematical, Physical and Engineering Sciences*, vol. 377, no. 2136, p. 20180202, 2019.

[30] J. Schmittbuhl, S. Gentier, and S. Roux, "Field measurements of the roughness of fault surfaces," *Geophysical Research Letters*, vol. 20, no. 8, pp. 639–641, 1993.

[31] J. Schmittbuhl, F. Schmitt, and C. Scholz, "Scaling invariance of crack surfaces," *Journal of Geophysical Research: Solid Earth*, vol. 100, no. B4, pp. 5953–5973, 1995.

[32] D. Sornette, "Discrete-scale invariance and complex dimensions," *Physics Reports*, vol. 297, no. 5, pp. 239–270, 1998.

[33] E. Bouchaud, "The morphology of fracture surfaces: a tool for understanding crack propagation in complex materials," *Surface Review and Letters*, vol. 10, no. 05, pp. 797–814, 2003.

[34] S. Zapperi, P. K. V. Nukala, and S. Šimunović, "Crack roughness and avalanche precursors in the random fuse model," *Physical Review E*, vol. 71, no. 2, p. 026106, 2005.

[35] S. Roux, A. Hansen, and E. Guyon, "Criticality in non-linear transport properties of heterogeneous materials," *Journal de Physique*, vol. 48, no. 12, pp. 2125–2130, 1987.

[36] M. Sahimi, *Heterogeneous Materials I: Linear transport and optical properties*, vol. 22. Springer Science & Business Media, 2003.

[37] W.-Z. Cai, S.-T. Tu, and J.-M. Gong, "A physically based percolation model of the effective electrical conductivity of particle filled composites," *Journal of Composite Materials*, vol. 40, no. 23, pp. 2131–2142, 2006.

[38] C. Bowen and D. P. Almond, “Modelling the ‘universal’ dielectric response in heterogeneous materials using microstructural electrical networks,” *Materials Science and Technology*, vol. 22, no. 6, pp. 719–724, 2006.

[39] I. Aranson, V. Kalatsky, and V. Vinokur, “Continuum field description of crack propagation,” *Physical Review Letters*, vol. 85, no. 1, p. 118, 2000.

[40] R. Spatschek, E. Brener, and A. Karma, “Phase field modeling of crack propagation,” *Philosophical Magazine*, vol. 91, no. 1, pp. 75–95, 2011.

[41] D. Bonamy and E. Bouchaud, “Failure of heterogeneous materials: A dynamic phase transition?,” *Physics Reports*, vol. 498, no. 1, pp. 1–44, 2011.

[42] J. Chopin, A. Bhaskar, A. Jog, and L. Ponson, “Depinning dynamics of crack fronts,” *Physical Review Letters*, vol. 121, no. 23, p. 235501, 2018.

[43] F. T. Peirce, “32—X.—Tensile tests for cotton yarns v.—“The weakest link” theorems on the strength of long and of composite specimens,” *Journal of the Textile Institute Transactions*, vol. 17, pp. T355–368, 1926.

[44] F. Raischel, F. Kun, and H. J. Herrmann, “Fiber bundle models for composite materials,” *The e-Journal of Nondestructive Testing & Ultrasonics*, vol. 11, no. 12, 2006.

[45] F. Kun, F. Raischel, R. Hidalgo, and H. Herrmann, “Extensions of fibre bundle models,” in *Modelling Critical and Catastrophic Phenomena in Geoscience*, pp. 57–92, Springer, 2006.

[46] P. K. V. V. Nukala, S. imunovi, and S. Zapperi, “Percolation and localization in the random fuse model,” *Journal of Statistical Mechanics: Theory and Experiment*, vol. 2004, p. P08001, aug 2004.

[47] A. G. Evans and K. T. Faber, “Toughening of ceramics by circumferential microcracking,” *Journal of the American Ceramic Society*, vol. 64, no. 7, pp. 394–398, 1981.

[48] D. K. Shum and J. W. Hutchinson, “On toughening by microcracks,” *Mechanics of Materials*, vol. 9, no. 2, pp. 83–91, 1990.

[49] K. T. Faber and A. G. Evans, “Crack deflection processes—I. Theory,” *Acta Metallurgica*, vol. 31, no. 4, pp. 565–576, 1983.

[50] H. Gao and J. R. Rice, “A first-order perturbation analysis of crack trapping by arrays of obstacles,” *Journal of Applied Mechanics*, vol. 56, no. 4, p. 828, 1989.

[51] H. Ming-Yuan and J. W. Hutchinson, “Crack deflection at an interface between dissimilar elastic materials,” *International Journal of Solids and Structures*, vol. 25, no. 9, pp. 1053–1067, 1989.

[52] K. Raveendran, A. Verma, and C. Rao, "Bounds on effective fracture toughness of multiphase materials," *Composites*, vol. 22, no. 4, pp. 290–294, 1991.

[53] A. F. Bower and M. Ortiz, "A three-dimensional analysis of crack trapping and bridging by tough particles," *Journal of the Mechanics and Physics of Solids*, vol. 39, no. 6, pp. 815–858, 1991.

[54] S. Yi, S. Gao, and L. Shen, "Fracture toughening mechanism of shape memory alloys under mixed-mode loading due to martensite transformation," *International Journal of Solids and Structures*, vol. 38, no. 24-25, pp. 4463–4476, 2001.

[55] J. Ma, M.-S. Mo, X.-S. Du, P. Rosso, K. Friedrich, and H.-C. Kuan, "Effect of inorganic nanoparticles on mechanical property, fracture toughness and toughening mechanism of two epoxy systems," *Polymer*, vol. 49, no. 16, pp. 3510–3523, 2008.

[56] N. R. Brodnik, C.-J. Hsueh, K. T. Faber, B. Bourdin, G. Ravichandran, and K. Bhattacharya, "Guiding and trapping cracks with compliant inclusions for enhancing toughness of brittle composite materials," *Journal of Applied Mechanics*, vol. 87, no. 3, 2020.

[57] N. Brodnik, S. Brach, C. Long, G. Ravichandran, B. Bourdin, K. Faber, and K. Bhattacharya, "Fracture diodes: Directional asymmetry of fracture toughness," *Physical Review Letters*, vol. 126, no. 2, p. 025503, 2021.

[58] S. Torquato, "Random heterogeneous media: Microstructure and improved bounds on effective properties," *Applied Mechanics Reviews*, vol. 44, no. 2, p. 37, 1991.

[59] J. Quintanilla and S. Torquato, "Microstructure functions for a model of statistically inhomogeneous random media," *Physical Review E*, vol. 55, no. 2, p. 1558, 1997.

[60] Y. Jiao, F. Stillinger, and S. Torquato, "A superior descriptor of random textures and its predictive capacity," *Proceedings of the National Academy of Sciences*, vol. 106, no. 42, pp. 17634–17639, 2009.

[61] H. Tada, P. Paris, and G. Irwin, "The analysis of cracks handbook," *ASME Press*, vol. 2, p. 1, 2000.

[62] R. Bowley and M. Sanchez, "Introductory statistical mechanics," *European Journal of Physics*, vol. 21, no. 2, p. 197, 2000.

[63] M. Kardar, *Statistical Physics of Particles.* Cambridge University Press, 2007.

[64] M. Kardar, *Statistical Physics of Fields.* Cambridge University Press, 2007.

[65] J. G. Briano and E. D. Glandt, "Statistical thermodynamics of polydisperse fluids," *The Journal of Chemical Physics*, vol. 80, no. 7, pp. 3336–3343, 1984.

[66] D. A. Kofke and E. D. Glandt, "Nearly monodisperse fluids. I. Monte Carlo simulations of Lennard-Jones particles in a semigrand ensemble," *The Journal of Chemical Physics*, vol. 87, no. 8, pp. 4881–4890, 1987.

[67] D. A. Kofke and E. D. Glandt, "Monte Carlo simulation of multicomponent equilibria in a semigrand canonical ensemble," *Molecular Physics*, vol. 64, no. 6, pp. 1105–1131, 1988.

[68] D. Frenkel and B. Smit, *Understanding Molecular Simulation: From Algorithms to Applications*, vol. 1. Elsevier, 2001.

[69] N. Metropolis, A. W. Rosenbluth, M. N. Rosenbluth, A. H. Teller, and E. Teller, "Equation of state calculations by fast computing machines," *The Journal of Chemical Physics*, vol. 21, no. 6, pp. 1087–1092, 1953.

[70] H. Laubie, S. Monfared, F. Radjaï, R. Pellenq, and F.-J. Ulm, "Effective potentials and elastic properties in the lattice-element method: isotropy and transverse isotropy," *Journal of Nanomechanics and Micromechanics*, vol. 7, no. 3, p. 04017007, 2017.

[71] S. Plimpton, "Fast parallel algorithms for short-range molecular dynamics," *Journal of Computational Physics*, vol. 117, no. 1, pp. 1–19, 1995.

[72] A. Stukowski, "Visualization and analysis of atomistic simulation data with OVITO–the Open Visualization Tool," *Modelling and Simulation in Materials Science and Engineering*, vol. 18, no. 1, p. 015012, 2009.

[73] J. Rice, "Thermodynamics of the quasi-static growth of Griffith cracks," *Journal of the Mechanics and Physics of Solids*, vol. 26, no. 2, pp. 61–78, 1978.

[74] D. S. Dugdale, "Yielding of steel sheets containing slits," *Journal of the Mechanics and Physics of Solids*, vol. 8, no. 2, pp. 100–104, 1960.

[75] J. Hutchinson, "Singular behaviour at the end of a tensile crack in a hardening material," *Journal of the Mechanics and Physics of Solids*, vol. 16, no. 1, pp. 13–31, 1968.

[76] Z. Yang, X. Su, J. Chen, and G. Liu, "Monte Carlo simulation of complex cohesive fracture in random heterogeneous quasi-brittle materials," *International Journal of Solids and Structures*, vol. 46, no. 17, pp. 3222–3234, 2009.

[77] P. Ray, "Statistical physics perspective of fracture in brittle and quasi-brittle materials," *Philosophical Transactions of the Royal Society A*, vol. 377, no. 2136, p. 20170396, 2019.

[78] H. J. Herrmann and S. Roux, *Statistical Models for the Fracture of Disordered Media*. Elsevier, 2014.

[79] S. Zapperi, P. Ray, H. E. Stanley, and A. Vespignani, "First-order transition in the breakdown of disordered media," *Physical Review Letters*, vol. 78, no. 8, p. 1408, 1997.

[80] J. Barés, M. Hattali, D. Dalmas, and D. Bonamy, "Fluctuations of global energy release and crackling in nominally brittle heterogeneous fracture," *Physical Review Letters*, vol. 113, no. 26, p. 264301, 2014.

[81] J. R. Rice and R. Thomson, "Ductile versus brittle behaviour of crystals," *The Philosophical Magazine: A Journal of Theoretical Experimental and Applied Physics*, vol. 29, no. 1, pp. 73–97, 1974.

[82] B. Decelis, A. S. Argon, and S. Yip, "Molecular dynamics simulation of crack tip processes in alpha-iron and copper," *Journal of Applied Physics*, vol. 54, no. 9, pp. 4864–4878, 1983.

[83] K. S. Cheung and S. Yip, "A molecular-dynamics simulation of crack-tip extension: the brittle-to-ductile transition," *Modelling and Simulation in Materials Science and Engineering*, vol. 2, no. 4, p. 865, 1994.

[84] J. Sinclair, "The influence of the interatomic force law and of kinks on the propagation of brittle cracks," *The Philosophical Magazine: A Journal of Theoretical Experimental and Applied Physics*, vol. 31, no. 3, pp. 647–671, 1975.

[85] B. L. Holian and R. Ravelo, "Fracture simulations using large-scale molecular dynamics," *Physical Review B*, vol. 51, no. 17, p. 11275, 1995.

[86] M. Marder, "Effects of atoms on brittle fracture," *International Journal of Fracture*, vol. 130, no. 2, pp. 517–555, 2004.

[87] M. J. Buehler and H. Gao, "Dynamical fracture instabilities due to local hyperelasticity at crack tips," *Nature*, vol. 439, no. 7074, pp. 307–310, 2006.

[88] S. Zhou, P. Lomdahl, R. Thomson, and B. Holian, "Dynamic crack processes via molecular dynamics," *Physical Review Letters*, vol. 76, no. 13, p. 2318, 1996.

[89] P. Gumbsch, S. Zhou, and B. Holian, "Molecular dynamics investigation of dynamic crack stability," *Physical Review B*, vol. 55, no. 6, p. 3445, 1997.

[90] M. Marder and S. Gross, "Origin of crack tip instabilities," *Journal of the Mechanics and Physics of Solids*, vol. 43, no. 1, pp. 1–48, 1995.

[91] F. F. Abraham and J. Broughton, "Large-scale simulations of brittle and ductile failure in fcc crystals," *Computational Materials Science*, vol. 10, no. 1-4, pp. 1–9, 1998.

[92] J. Kermode, T. Albaret, D. Sherman, N. Bernstein, P. Gumbsch, M. Payne, G. Csányi, and A. De Vita, "Low-speed fracture instabilities in a brittle crystal," *Nature*, vol. 455, no. 7217, pp. 1224–1227, 2008.

[93] E. Bouchbinder, J. Fineberg, and M. Marder, "Dynamics of simple cracks," *Annual Review of Condensed Matter Physics*, vol. 1, no. 1, pp. 371–395, 2010.

[94] V. Ginzburg and L. Manevitch, "The extended Frenkel-Kontorova model and its application to the problems of brittle fracture and adhesive failure," *International Journal of Fracture*, vol. 64, no. 1, pp. 93–99, 1993.

[95] R. Miller, E. Tadmor, R. Phillips, and M. Ortiz, "Quasicontinuum simulation of fracture at the atomic scale," *Modelling and Simulation in Materials Science and Engineering*, vol. 6, no. 5, p. 607, 1998.

[96] R. Pérez and P. Gumbsch, "Directional anisotropy in the cleavage fracture of silicon," *Physical Review Letters*, vol. 84, no. 23, p. 5347, 2000.

[97] B. R. Lawn, "Physics of fracture," *Journal of the American Ceramic Society*, vol. 66, no. 2, pp. 83–91, 1983.

[98] J. Kermode, L. Ben-Bashat, F. Atrash, J. Cilliers, D. Sherman, and A. De Vita, "Macroscopic scattering of cracks initiated at single impurity atoms," *Nature Communications*, vol. 4, no. 1, pp. 1–8, 2013.

[99] M. Bauchy, B. Wang, M. Wang, Y. Yu, M. J. A. Qomi, M. M. Smedskjaer, C. Bichara, F.-J. Ulm, and R. Pellenq, "Fracture toughness anomalies: Viewpoint of topological constraint theory," *Acta Materialia*, vol. 121, pp. 234–239, 2016.

[100] H. Laubie, F. Radjai, R. Pellenq, and F.-J. Ulm, "Stress transmission and failure in disordered porous media," *Physical Review Letters*, vol. 119, no. 7, p. 075501, 2017.

[101] P. M. Morse, "Diatomic molecules according to the wave mechanics. II. Vibrational levels," *Physical Review*, vol. 34, no. 1, p. 57, 1929.

[102] M. Campostrini, A. Pelissetto, P. Rossi, and E. Vicari, "25th-order high-temperature expansion results for three-dimensional Ising-like systems on the simple-cubic lattice," *Physical Review E*, vol. 65, no. 6, p. 066127, 2002.

[103] M. Luban, "Solvable compressible Ising model," *Physical Review B*, vol. 7, no. 5, p. 2203, 1973.

[104] Visit http://link.aps.org/supplemental/10.1103/PhysRevE.103.013003 for a visualization of the potential energy evolution during the fracture process, as well as the formation of microcracks throughout the system converging into one macrocrack at failure.

[105] P. Nicholson, D. Nicholson, W. Nicholson, and N. G. Parsonage, *Computer Simulation and the Statistical Mechanics of Adsorption*. Academic Press, 1982.

[106] R.-M. Pellenq and P. Levitz, "Capillary condensation in a disordered mesoporous medium: a grand canonical Monte Carlo study," *Molecular Physics*, vol. 100, no. 13, pp. 2059–2077, 2002.

[107] T. Al-Mulla, R. J.-M. Pellenq, and F.-J. Ulm, "Griffith's postulate: Grand canonical Monte Carlo approach for fracture mechanics of solids," *Engineering Fracture Mechanics*, vol. 199, pp. 544–554, 2018.

[108] C. K. H. Dharan, "Fracture Mechanics of Composite Materials," *Journal of Engineering Materials and Technology*, vol. 100, pp. 233–247, 07 1978.

[109] G. Bao, S. Ho, Z. Suo, and B. Fan, "The role of material orthotropy in fracture specimens for composites," *International Journal of Solids and Structures*, vol. 29, no. 9, pp. 1105–1116, 1992.

[110] G. Constantinides, K. R. Chandran, F.-J. Ulm, and K. Van Vliet, "Grid indentation analysis of composite microstructure and mechanics: Principles and validation," *Materials Science and Engineering: A*, vol. 430, no. 1-2, pp. 189–202, 2006.

[111] K. Sieradzki and R. Li, "Fracture behavior of a solid with random porosity," *Physical Review Letters*, vol. 56, no. 23, p. 2509, 1986.

[112] S. L. Kramer, A. Jones, A. Mostafa, B. Ravaji, T. Tancogne-Dejean, C. C. Roth, M. G. Bandpay, K. Pack, J. T. Foster, M. Behzadinasab, *et al.*, "The third Sandia Fracture Challenge: predictions of ductile fracture in additively manufactured metal," *International Journal of Fracture*, vol. 218, no. 1, pp. 5–61, 2019.

[113] E. A. Papon and A. Haque, "Fracture toughness of additively manufactured carbon fiber reinforced composites," *Additive Manufacturing*, vol. 26, pp. 41–52, 2019.

[114] Z. Jia and L. Wang, "3D printing of biomimetic composites with improved fracture toughness," *Acta Materialia*, vol. 173, pp. 61–73, 2019.

[115] S. Kamat, X. Su, R. Ballarini, and A. Heuer, "Structural basis for the fracture toughness of the shell of the conch Strombus gigas," *Nature*, vol. 405, pp. 1036–1040, 2000.

[116] H. Gao, "Application of fracture mechanics concepts to hierarchical biomechanics of bone and bone-like materials," *International Journal of Fracture*, vol. 138, no. 1-4, p. 101, 2006.

[117] H. Yao, Z. Xie, C. He, and M. Dao, "Fracture mode control: a bio-inspired strategy to combat catastrophic damage," *Scientific Reports*, vol. 5, no. 1, pp. 1–6, 2015.

[118] H.-C. Loh, T. Divoux, B. Gludovatz, P. Gilbert, R. Ritchie, F.-J. Ulm, and A. Masic, "Nacre toughening due to cooperative plastic deformation of stacks of co-oriented aragonite platelets," *Communications Materials*, vol. 1, no. 1, pp. 1–10, 2020.

[119] M. Mower and A. Argon, "Experimental investigations of crack trapping in brittle heterogeneous solids," *Mechanics of Materials*, vol. 19, pp. 343–364, 1995.

[120] Y. Shao, H.-P. Zhao, X.-Q. Feng, and H. Gao, "Discontinuous crack-bridging model for fracture toughness analysis of nacre," *Journal of the Mechanics and Physics of Solids*, vol. 60, pp. 1400–1419, 2012.

[121] M. Hossain, C.-J. Hsueh, B. Bourdin, and K. Bhattacharya, "Effective toughness of heterogeneous media," *Journal of the Mechanics and Physics of Solids*, vol. 71, pp. 15–32, 2014.

[122] Z. Bažant and J.-J. Le, *Probabilistic Mechanics of Quasibrittle Structures: Strength, Lifetime, and Size Effect.* Cambridge University Press, 2017.

[123] P. Beale and D. Srolovitz, "Elastic fracture in random materials," *Physical Review B*, vol. 37, p. 5500, 1988.

[124] A. Delaplace, G. Pijaudier-Cabot, and S. Roux, "Progressive damage in discrete models and consequences on continuum modelling," *Journal of the Mechanics and Physics of Solids*, vol. 44, no. 1, pp. 99–136, 1997.

[125] T. Mulla, S. Moeini, K. Ioannidou, R. J.-M. Pellenq, and F.-J. Ulm, "Phase diagram of brittle fracture in the semi-grand-canonical ensemble," *Physical Review E*, vol. 103, p. 013003, Jan 2021.

[126] R. Kubo, "The fluctuation-dissipation theorem," *Reports on Progress in Physics*, vol. 29, no. 1, p. 255, 1966.

[127] P. Kabir, F.-J. Ulm, and A.-T. Akono, "Rate-independent fracture toughness of gray and black kerogen-rich shales," *Acta Geotechnica*, vol. 12, no. 6, pp. 1207–1227, 2017.

[128] H. Kakisawa and T. Sumitomo, "The toughening mechanism of nacre and structural materials inspired by nacre," *Science and Technology of Advanced Materials*, vol. 12, no. 6, p. 064710, 2011.

[129] A. Evans and A. Heuer, "Transformation toughening in ceramics: Martensitic transformations in crack-tip stress fields," *Journal of the American Ceramic Society*, vol. 63, no. 5-6, pp. 241–248, 1980.

[130] H. Pan and G. Weng, "A micromechanics theory for the transformation toughening of two-phase ceramics," *Acta Mechanica*, vol. 156, no. 1, pp. 47–62, 2002.

[131] T. Yamaguchi, Y. Onoue, and Y. Sawae, “Topology and toughening of sparse elastic networks,” *Physical Review Letters*, vol. 124, p. 068002, Feb 2020.

[132] Y. Barak, A. Srivastava, and S. Osovski, “Correlating fracture toughness and fracture surface roughness via correlation length scale,” *International Journal of Fracture*, vol. 219, no. 1, pp. 19–30, 2019.

[133] S. Torquato, J. Beasley, and Y. Chiew, “Two-point cluster function for continuum percolation,” *The Journal of Chemical Physics*, vol. 88, no. 10, pp. 6540–6547, 1988.

[134] P. Smith and S. Torquato, “Computer simulation results for the two-point probability function of composite media,” *Journal of Computational Physics*, vol. 76, no. 1, pp. 176–191, 1988.

[135] J. E. Bertram and A. A. Biewener, “Bone curvature: Sacrificing strength for load predictability?,” *Journal of Theoretical Biology*, vol. 131, no. 1, pp. 75–92, 1988.

[136] Z. Feng, J. Rho, S. Han, and I. Ziv, “Orientation and loading condition dependence of fracture toughness in cortical bone,” *Materials Science and Engineering: C*, vol. 11, no. 1, pp. 41–46, 2000.

[137] M. R. Chandler, P. G. Meredith, N. Brantut, and B. R. Crawford, “Fracture toughness anisotropy in shale,” *Journal of Geophysical Research: Solid Earth*, vol. 121, no. 3, pp. 1706–1729, 2016.

[138] R. Rice, “Ceramic matrix composite toughening mechanisms: An update,” in *Proceedings of the 9th Annual Conference on Composites and Advanced Ceramic Materials: Ceramic Engineering and Science Proceedings*, vol. 6, pp. 589–607, Wiley Online Library, 1985.

[139] K. Konopka, M. Maj, and K. J. Kurzydłowski, “Studies of the effect of metal particles on the fracture toughness of ceramic matrix composites,” *Materials Characterization*, vol. 51, no. 5, pp. 335–340, 2003.

[140] I. T. Jolliffe and J. Cadima, “Principal component analysis: a review and recent developments,” *Philosophical Transactions of the Royal Society A: Mathematical, Physical and Engineering Sciences*, vol. 374, no. 2065, p. 20150202, 2016.

[141] B. Epstein, “Application of the theory of extreme values in fracture problems,” *Journal of the American Statistical Association*, vol. 43, no. 243, pp. 403–412, 1948.

[142] R. Doremus, “Fracture statistics: A comparison of the normal, Weibull, and Type I extreme value distributions,” *Journal of Applied Physics*, vol. 54, no. 1, pp. 193–198, 1983.

[143] D. W. Nicholson and P. Ni, “Extreme value probabilistic theory for mixed-mode brittle fracture,” *Engineering Fracture Mechanics*, vol. 58, no. 1-2, pp. 121–132, 1997.

[144] D. Nicholson, P. Ni, and Y. Ahn, “Probabilistic theory for mixed mode fatigue crack growth in brittle plates with random cracks,” *Engineering Fracture Mechanics*, vol. 66, no. 3, pp. 305–320, 2000.

[145] A. Rinaldi, D. Krajcinovic, and S. Mastilovic, “Statistical damage mechanics and extreme value theory,” *International Journal of Damage Mechanics*, vol. 16, no. 1, pp. 57–76, 2007.

[146] O. Francesconi, M. Panero, and D. Preti, “Strong coupling from non-equilibrium Monte Carlo simulations,” *Journal of High Energy Physics*, vol. 2020, no. 7, pp. 1–42, 2020.

[147] J. P. Nilmeier, G. E. Crooks, D. D. Minh, and J. D. Chodera, “Nonequilibrium candidate Monte Carlo is an efficient tool for equilibrium simulation,” *Proceedings of the National Academy of Sciences*, vol. 108, no. 45, pp. E1009–E1018, 2011.

[148] B. K. Radak and B. Roux, “Efficiency in nonequilibrium molecular dynamics Monte Carlo simulations,” *The Journal of Chemical Physics*, vol. 145, no. 13, p. 134109, 2016.

[149] M. Mamonova, I. Popov, P. Prudnikov, V. Prudnikov, and A. Purtov, “Monte Carlo simulation of the non-equilibrium critical dynamics of low-dimensional magnetics and multilayer structures,” *Lobachevskii Journal of Mathematics*, vol. 38, no. 5, pp. 944–947, 2017.

[150] M. D. P. Martínez, M. Giuliano, and M. Hoyuelos, “Out-of-equilibrium Monte Carlo simulations of a classical gas with Bose-Einstein statistics,” *Physical Review E*, vol. 102, no. 6, p. 062125, 2020.

[151] L. Rowley, D. Nicholson, and N. Parsonage, “Monte Carlo grand canonical ensemble calculation in a gas-liquid transition region for 12-6 Argon,” *Journal of Computational Physics*, vol. 17, no. 4, pp. 401–414, 1975.

[152] L. D. Gelb, K. Gubbins, R. Radhakrishnan, and M. Sliwinska-Bartkowiak, “Phase separation in confined systems,” *Reports on Progress in Physics*, vol. 62, no. 12, p. 1573, 1999.

[153] G. A. Francfort and J.-J. Marigo, “Revisiting brittle fracture as an energy minimization problem,” *Journal of the Mechanics and Physics of Solids*, vol. 46, no. 8, pp. 1319–1342, 1998.

[154] B. Bourdin, G. A. Francfort, and J.-J. Marigo, “The variational approach to fracture,” *Journal of Elasticity*, vol. 91, no. 1-3, pp. 5–148, 2008.

[155] C. Miehe, F. Welschinger, and M. Hofacker, "Thermodynamically consistent phase-field models of fracture: Variational principles and multi-field FE implementations," *International Journal for Numerical Methods in Engineering*, vol. 83, no. 10, pp. 1273–1311, 2010.

[156] R. de Borst and C. V. Verhoosel, "Gradient damage vs phase-field approaches for fracture: Similarities and differences," *Computer Methods in Applied Mechanics and Engineering*, vol. 312, pp. 78–94, 2016.

[157] A. D. McNaught, A. Wilkinson, *et al.*, *Compendium of Chemical Terminology*, vol. 1669. Blackwell Science Oxford, 1997.

[158] V. Topin, J.-Y. Delenne, F. Radjaı, L. Brendel, and F. Mabille, "Strength and failure of cemented granular matter," *The European Physical Journal E*, vol. 23, no. 4, pp. 413–429, 2007.

[159] K. S. Thorne and R. D. Blandford, *Modern Classical Physics: Optics, Fluids, Plasmas, Elasticity, Relativity, and Statistical Physics*. Princeton University Press, 2017.